UNIVERSITY OF SOUTHAMPTON

Faculty of Engineering and Physical Sciences
School of Chemistry

Protein NMR on a Chip: Development of an Integrated Microfluidic Platform for Studying Protein-Ligand Interactions by Nuclear Magnetic Resonance

by

Marek Plata

BSc

ORCiD: 0000-0003-2683-5762

A thesis for the degree of
Doctor of Philosophy

September 2023

University of Southampton

Abstract

Faculty of Engineering and Physical Sciences
School of Chemistry

Doctor of Philosophy

Protein NMR on a Chip:
Development of an Integrated Microfluidic Platform for Studying Protein-Ligand Interactions by Nuclear Magnetic Resonance

by Marek Plata

The following work demonstrates the performance of the integrated microfluidic system for studying protein-ligand interactions by nuclear magnetic resonance (NMR). The device couples together the advantages associated with microfluidic operation, i.e. minimised sample use and precision of operation, and characterisation by NMR. NMR offers unique capabilities for biomolecular research, relating to its non-invasive and non-destructive nature and atomic-scale resolution. This enables identification of the number and location of interaction sites, allosteric effects, atomic structures, dynamics of ligands and proteins, as well as full thermodynamic evaluation of the interaction. Integrating the aforementioned aspects can open new avenues for protein analysis, on one hand enhancing the usually limited throughput and functionality of NMR, on the other providing an extensive readout method to microfluidic systems, that can be further linked with other analytical tools.

Contents

List of Figures

List of Tables

Declaration of Authorship

I declare that this thesis and the work presented in it is my own and has been generated by me as the result of my own original research.

I confirm that:

1. This work was done wholly or mainly while in candidature for a research degree at this University;
2. Where any part of this thesis has previously been submitted for a degree or any other qualification at this University or any other institution, this has been clearly stated;
3. Where I have consulted the published work of others, this is always clearly attributed;
4. Where I have quoted from the work of others, the source is always given. With the exception of such quotations, this thesis is entirely my own work;
5. I have acknowledged all main sources of help;
6. Where the thesis is based on work done by myself jointly with others, I have made clear exactly what was done by others and what I have contributed myself;
7. Parts of this work have been published as:

Signed:..... Date:.....

Acknowledgements

I would like to express gratitude to my PhD supervisors, Dr Jörn M. Werner and Prof. Marcel Utz for their patience and guidance that has helped me grow academically and personally through this time. In particular, I appreciate the time they have invested to help me understand the many aspects of nuclear magnetic resonance which I found especially challenging. With their support I feel I have gained skills and knowledge that will stay with me for years to come.

Acknowledgements are due to the members of my research group: Sylwia Ostrowska, Evie Rogers, Manvendra Sharma, Bishnubatra Patra and Billy Hale, who have helped me to tackle the common and uncommon challenges I faced bringing this project to life. Manvendra Sharma and Billy Hale deserve special credit for their known-how and support they provided me to implement the aspects of automation and peristaltics to this work.

Special thanks go to Dr Christopher Williams and Prof. Matthew Crump at the University of Bristol for facilitating the acquisition of additional protein spectra using the state-of-the-art 1.7 mm MicroCryoProbe^{TM} (Bruker, US).

I appreciate all of my colleagues who helped me enormously with everyday conversations on science and beyond. My thanks go to: Christian Bengs, Jamie Whipham, George Bacanu, Murari Soundararajan, Mohamed Sabba, Johannes Collel, Laurynas Dagys, Bonifac Legrady, Giulia Melchiorre, Karel Kouril, Hana Kourilova, Stuart Elliot and Barbara Ripka. George Bacanu is due a singular distinction for proofreading the majority of this work.

Finally, I wish to thank my wife Mariana who has always believed in me and supported my choices. This would not be possible without you.

To my wife Mariana
and our daughter Clara

Chapter 1

Introduction

1.1 The goal

The aim of this work is to develop and validate an automated system for characterisation of protein - ligand interactions, exploiting the advantages of microfluidic operation and analysis by NMR. Microfluidics allow for precise control of the experimental conditions and operation with only microlitres of sample, while NMR is inherently non-invasive and non-destructive and provides detailed atomic-scale information about biomolecules and their behaviour in solution, often in near-physiological conditions. Combination of the two approaches into a common LoC-μNMR platform therefore offers unprecedented opportunities, otherwise unavailable for most analytical tools.

1.2 Motivation

NMR is a very powerful diagnostic technique, however it normally operates on $\sim$ 500 μL samples and allows for limited functionality. A number of solutions that addresses either the sample volume requirements or expands the applications' range are available, yet all resolve those issues exclusively. Microfluidics on the other hand might provide the right balance, as it offers high precision of operation with only microlitres of sample. Therefore, an integrated LoC-μNMR system can present a range of unique advantages to biomolecular research. Such system should contain generic components that introduce multiple liquid samples, combine and mix them, and operate autonomously inside the NMR spectrometer. In microfluidics, these functions are often carried out by pneumatically actuated microvalves and pumps[56,164] that rely on deformation of PDMS to manipulate the sample liquid. In the context of NMR these types of solutions are not trivial. The device is required to operate at high magnetic

fields and within the confined space of the spectrometer bore. PDMS in particular is detrimental to the magnetic field homogeneity and leads to large background signals in the NMR spectra. Fortunately, Yilmaz and Utz[186] have already demonstrated a way to overcome this issue. It is possible to fabricate fully NMR-compatible PMMA chips that contain PDMS-based components away from the detection area, and do not affect the spectral resolution. Rapid prototyping of the PMMA chips is available in the Utz lab, those are made to a generic design corresponding to the geometry of the homebuilt transmission line probe. The design flexibility and rapid prototyping allows for a range of functionalities to be implemented and evaluated time- and cost-effectively.

This project is aimed to demonstrate the functionality of such a device specifically in the context of protein NMR. The assumed strategy is to carry out a fully automated and highly precise protein-ligand titration experiments with minimal use of protein sample. In a conventional NMR approach this is achieved by repeated exchange of small quantities of liquid between two ~ 500 μl samples: one at zero ligand concentration, the other containing ligand concentration sufficient to ensure saturation of the protein. In the NMR spectra, recorded at each of the exchange steps, changes can be observed in the chemical shift, signal intensity or linewidth for the nuclei involved in the interaction, which give a read-out for the fraction bound of protein. Based on this data the thermodynamic characterisation of the interaction, including the determination of the binding constant, is achieved. Implementation of this process into a LoC-μNMR platform allows to eliminate the need for extensive, error-prone manipulations of the samples, and offers notable cost reduction by lowered sample use. Upon successful completion of this task further developments can be considered, e.g. adaptation towards other protein NMR experiments, parallelisation or formulation of a common pipeline approach leading from microscale protein expression to analysis.

The work described benefits from previous accomplishments in the Utz and Werner labs. Specifically, the custom-built transmission line probe probe and its capability for 2D detection[150], as well as the fabrication methods of NMR-compatible microfluidic devices[186]. Likewise, the main subject of study for this work, the hFynSH3 protein, was readily available and its expression and purification for the purpose of analysis by NMR could be carried out following well-established protocols. The novelty of this work relates to the adaptation of the microfluidic device and the associated hardware to suit the specific requirements of the titration experiment, automation of the entire experimental procedure with integration of NMR acquisition, and extending the current state of knowledge on the hFynSH3 protein with extensive set of heteronuclear NMR data.

The aim of this thesis is to present the author's individual contributions towards this project. Where relevant, the inputs of others are clearly stated. This document is organised as follows. In chapter 2 the main theoretical grounding and present-day knowledge within the field is summarised. Chapter 3 presents the author's work,

achieved using a commercial state-of-the-art NMR equipment, for structural and thermodynamic characterisation of protein-ligand interactions using biologically relevant and well defined molecular model system. The design, operation and functional validation of the novel LoC-μNMR platform is shown in chapter 4, while chapter 5 demonstrates the applicability of this device towards high resolution protein-observed NMR studies of protein-ligand interactions. Chapter 6 specifies the experimental considerations in relation to the presented results and chapter 7 outlines the main conclusions of the project.

Chapter 2

Background

2.1 Physical foundations

The following summarises the fundamental principles of nuclear magnetic resonance needed to describe the methods involved and results obtained in the course of the 'Protein NMR on a Chip' project. The author admits many concepts are intentionally simplified, if considered not essential to the body of the presented work. Comprehensive explanation of the theoretical concepts of NMR is available in the works by Cavanagh et al.[20], Claridge[23], Keeler[74], Levitt[86], Teng[159], Wüthrich[179] and others.

2.1.1 The quantum mechanical principles

NMR is the study of matter through the interaction of the atomic nuclei with the magnetic field. This interaction is made possible thanks to the *spin*, i.e. the intrinsic form of angular momentum carried by elementary particles. Spin is an inherent quantum mechanical property that cannot be adequately explained by classical physics. Quantum mechanics postulates that all nuclei are characterised by the nuclear spin quantum number, I, which can have values greater than or equal to zero and is defined by multiples of $1/2$. A correlation exists between the nucleus' mass number and I such that nuclei with an even mass number always have an integer spin quantum number, while those with odd mass numbers posses non-integer I, i.e. $1/2$, $3/2$, $5/2$, etc. Only nuclei with non-zero I posses nuclear spin and as such can be observed by NMR. In the context of organic chemistry a clear setback is that the dominant carbon isotope, ^{12}C, has $I = 0$ which renders it 'NMR silent'. Similar case exists for nitrogen, another fundamental element of organic molecules. For the most abundant nitrogen isotope, ^{14}N with $I = 1$, its nucleus is subject to significant quadrupolar interactions, that render it difficult to observe by NMR. Fortunately, other stable carbon and nitrogen isotopes exist, ^{13}C and ^{15}N with $I = 1/2$, more easily accessible to NMR, however at much

lower natural abundance. Nowadays numerous methods exist for labelling of organic molecules with ^{13}C and ^{15}N, nonetheless this adds considerable costs to sample preparation. In table 2.1 the nuclei most commonly analysed by NMR in the biomolecular context are listed along with their essential characteristics.

Nucleus	**Spin**	**Gyromagnetic ratio (γ) /MHz T^{-1}**	**Natural abundance /%**
^{1}H	1/2	42.58	99.99
^{2}H	1	6.54	0.01
^{13}C	1/2	10.71	1.07
^{14}N	1	3.08	99.6
^{15}N	1/2	-4.32	0.37
^{19}F	1/2	40.08	99.99
^{31}P	1/2	17.25	99.99

Table 2.1: Characteristics of relevant NMR-active nuclei.

A fundamental principle of NMR is the *Zeeman effect*, manifested as the separation of nuclear spin energy levels in the presence of a static magnetic field. This separation is related to the $(2I+1)$-fold degeneracy of the spin quantum number, meaning that for $I = 1/2$ the nucleus has two Zeeman states, while for $I = 1$ it has three. This expansion becomes greater for higher spin quantum numbers, however, much of the principles governing NMR can be explained based on the spin-1/2 Zeeman states, presented in fig. 2.1. By convention, the available energy states are defined as α and β or $+1/2$ and $-1/2$, which in a gross approximation can be explained as the spins aligning along or against the magnetic field, respectively. In a mathematical notation the two basis states are defined as vector quantities:

$$|\alpha\rangle = \begin{pmatrix} 1 \\ 0 \end{pmatrix} \qquad |\beta\rangle = \begin{pmatrix} 0 \\ 1 \end{pmatrix} \tag{2.1}$$

In reality, individual spins are not restricted to either of the states but rather exist in a *superposition* of the two, while the *wavefuncton* is the principal quantum mechanical entity that describes the superposition state:

$$|\psi\rangle = c_\alpha|\alpha\rangle + c_\beta|\beta\rangle = \begin{pmatrix} c_\alpha \\ c_\beta \end{pmatrix} \tag{2.2}$$

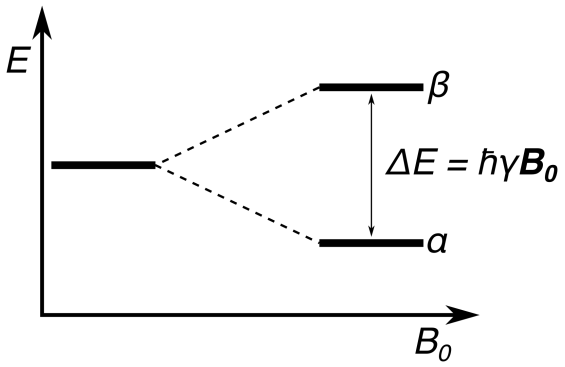

Figure 2.1: Energy levels for a spin-1/2 in the presence of a static magnetic field.

where c_α and c_β are the *superposition coefficients* relating to the individual populations of each state. As an essentially complex entity the wavefunction possess its complex conjugate counterpart, which in mathematical terms is defined as an adjoint, $|\psi\rangle^\dagger$, of the wavefunction column vector:

$$\langle\psi| = |\psi\rangle^\dagger = \begin{pmatrix} c_\alpha^* & c_\beta^* \end{pmatrix} \tag{2.3}$$

where $c_{\alpha,\beta}^*$ denotes the complex conjugates of the superposition coefficients. The above notation, established by Paul Dirac, is very useful to describe the fundamental properties of the wavefunction that are being exploited in NMR:

$$\langle\psi|\psi\rangle = \begin{pmatrix} c_\alpha^* & c_\beta^* \end{pmatrix} \begin{pmatrix} c_\alpha \\ c_\beta \end{pmatrix} = c_\alpha c_\alpha^* + c_\beta c_\beta^* = |c_\alpha|^2 + |c_\beta|^2 = 1 \tag{2.4}$$

$$|\psi\rangle\langle\psi| = \begin{pmatrix} c_\alpha \\ c_\beta \end{pmatrix} \begin{pmatrix} c_\alpha^* & c_\beta^* \end{pmatrix} = \begin{pmatrix} c_\alpha c_\alpha^* & c_\alpha c_\beta^* \\ c_\beta c_\alpha^* & c_\beta c_\beta^* \end{pmatrix} \tag{2.5}$$

Equations (2.4) and (2.5) denote the inner and outer product of vector entities, dictated by linear algebra. The inner product, eq. (2.4), specifies the normalisation condition of the wavefunction, meaning that although the exact populations of the $|\alpha\rangle$ and $|\beta\rangle$ cannot be fully known, the entire population within the wavefunction is constrained to the two available states. This principle is further supplemented by the orthogonality condition for different states, $|r_i\rangle$ and $|r_j\rangle$, together termed as *orthonormality*:

$$\langle r_i|r_j\rangle = \begin{cases} 0 & \text{if } i \neq j \\ 1 & \text{if } i = j \end{cases} \tag{2.6}$$

The outer product, eq. (2.5), results in an expansion of the one-dimensional vectors into the two-dimensional matrix including the quadratic products of the superposition coefficients. This product is called the projection operator of the basis states which

gains special significance when considering a large number of spins, in which case it is expressed as the density operator:

$$\hat{\rho} = \frac{|\psi_1\rangle\langle\psi_1| + |\psi_2\rangle\langle\psi_2| + \dots}{N} = \overline{|\psi\rangle\langle\psi|} \tag{2.7}$$

where N is the total number of spins while the overbar indicates the average over all spins within the ensemble. Analogous to eq. (2.5) the matrix representation of the density operator is:

$$\hat{\rho} = \begin{pmatrix} \rho_{\alpha\alpha} & \rho_{\alpha\beta} \\ \rho_{\beta\alpha} & \rho_{\beta\beta} \end{pmatrix} = \begin{pmatrix} \overline{c_\alpha c_\alpha^*} & \overline{c_\alpha c_\beta^*} \\ \overline{c_\beta c_\alpha^*} & \overline{c_\beta c_\beta^*} \end{pmatrix} \tag{2.8}$$

Conveniently, in this representation the diagonal matrix elements are the populations, $\rho_{\alpha\alpha}$ and $\rho_{\beta\beta}$, of the $|\alpha\rangle$ and $|\beta\rangle$ spin states. The off-diagonal elements on the other hand represent *coherences* between the states. Coherences are linked by the complex relationship:

$$\rho_{\alpha\beta} = \overline{c_\alpha c_\beta^*} = \left(\overline{c_\beta c_\alpha^*}\right)^* = {\rho_{\beta\alpha}}^* \tag{2.9}$$

and the populations are always normalised:

$$\rho_{\alpha\alpha} + \rho_{\beta\beta} = 1 \tag{2.10}$$

Both element types of the density matrix are of critical importance to NMR. While the population differences have a physical manifestation as the macroscopic equilibrium magnetisation of the sample inside the magnetic field, it is the coherences specifically that give rise to the observable NMR signal.

2.1.2 Emergence of the observable NMR signal

Presence of nuclear spins within the sample placed inside the static magnetic field, $\boldsymbol{B_0}$, gives rise to the macroscopic magnetisation, $\boldsymbol{M}$, as a consequence of the difference in population of the available spin states:

$$\boldsymbol{M} = \frac{N_\alpha}{N_\beta} = e^{\Delta E/k_B T} \tag{2.11}$$

where $N_{\alpha,\beta}$ simply represent the number of nuclei in a given energy state, ΔE is the energy separation between the α and β energy states, k_B is the Boltzmann constant and T is the temperature. As included in fig. 2.1, the energy separation is:

$$\Delta E = \hbar\gamma \boldsymbol{B_0} \tag{2.12}$$

where $\hbar$ is the reduced Planck constant, $\hbar = h/2\pi$, and γ is the nucleus-specific gyromagnetic ratio, as listed in table 2.1. Following from eqs. (2.11) and (2.12), it becomes

clear that $\boldsymbol{M}$ is mainly determined by the gyromagnetic ratio and the strength of the magnetic field.

According to the semi-classical *vector model* $\boldsymbol{M}$ is a vector quantity, which at thermodynamic equilibrium is aligned along or against the direction dictated by the $\boldsymbol{B_0}$, by convention the z axis. In a standard *pulse − acquire* NMR experiment, the signal is produced by perturbation of the magnetisation vector away from its equilibrium position through irradiation with an oscillating radiofrequency (RF) field, $\boldsymbol{B_1}$. The RF pulse results in generation of $\boldsymbol{B_1}$ in the x, y plane that exerts a torque on $\boldsymbol{M}$. With well chosen pulse duration $\boldsymbol{M}$ is rotated by 90° and aligns entirely in the direction perpendicular to $\boldsymbol{B_0}$, i.e. the transverse (x, y) plane. Once the RF pulse is switched off $\boldsymbol{M}$ begins a precession motion under the influence of $\boldsymbol{B_0}$. Precession is strictly a consequence of the spin of the nucleus and its frequency is dictated by the nucleus' gyromagnetic ratio, γ, in angular frequency it is expressed as:

$$\omega_0 = -\gamma \boldsymbol{B_0} \tag{2.13}$$

The gyromagnetic ratio is a measure of the nucleus' receptivity to the magnetic field, and along the magnitude of $\boldsymbol{B_0}$ determines the characteristic frequency of the nucleus' precession at a given magnetic field, called the *Larmor* frequency. This motion is detected according to the Faraday's law of induction as current on a coil located in the vicinity of the sample. The transverse magnetisation decays with time as the system eventually returns to the thermodynamic equilibrium with magnetisation oriented parallel to $\boldsymbol{B_0}$. This constitutes the free induction decay (FID) signal of the NMR experiment, recorded over approximately 1 second. Next, the FID signal is subject to Fourier transformation (FT), which decomposes the single signal in the time domain into all its individual frequency components.

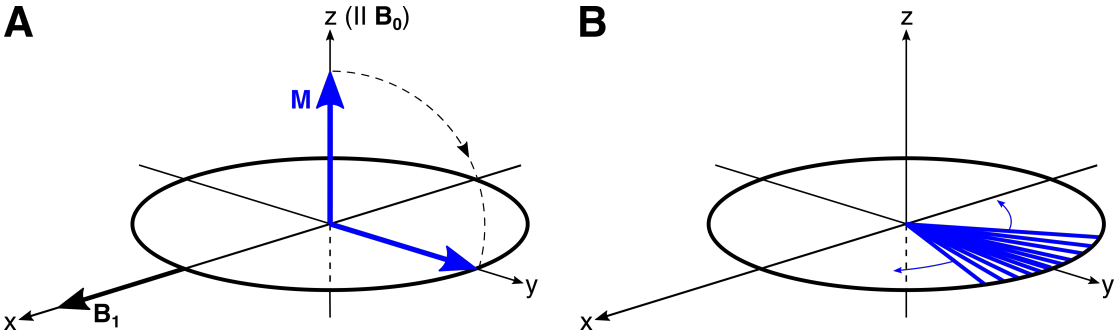

Figure 2.2: Vector model representation of a simple NMR experiment. Transfer of the magnetisation (A) from the equilibrium position to the transverse plane under the influence of $\boldsymbol{B_1}$ and (B) the decay of phase coherence during magnetisation precession that gives rise to the FID signal.

2.1.3 Precession in the rotating frame

Many notions become simplified when considering the precession not in the static laboratory frame, but a conceptual rotating frame. The aim of such transformation is to make the RF field independent of time. In this coordinate system the observed Larmor precession, ω_0, is expressed in relation to the frequency of the rotating frame, $\omega_{r.f.}$, therefore, in the rotating frame the frequency of precession is defined by the $offset$, $\Omega = \omega_0 - \omega_{r.f.}$. The consequence is that the $apparent$ magnetic field, $\boldsymbol{\Delta B}$, can also be expressed with respect to Ω:

$$\boldsymbol{\Delta B} = -\frac{\Omega}{\gamma} \tag{2.14}$$

and the $effective$ magnetic field becomes:

$$\boldsymbol{B}_{eff} = \boldsymbol{\Delta B} + \boldsymbol{B_1} \tag{2.15}$$

Utilising the *Bloch formalism*, the evolution of the macroscopic magnetisation during the NMR experiment can be predicted:

$$\frac{d}{dt}\boldsymbol{M} = \gamma(\boldsymbol{M} \times \boldsymbol{B}_{eff}) - R[\boldsymbol{M} - \boldsymbol{M_0}] \tag{2.16}$$

where $\boldsymbol{M_0}$ denotes the equilibrium magnetisation and $\boldsymbol{R}$ represents the relaxation matrix, which contains the terms governing the system's return to thermodynamic equilibrium. The critical conclusion is that, when viewed from the perspective of the rotating frame, the apparent magnetic field along the z axis can be much smaller than the applied $\boldsymbol{B_0}$. In the special case of $\omega_{r.f.}$ being equal to the Larmor frequency the $\boldsymbol{\Delta B}$ is reduced to zero and the $\boldsymbol{B_1}$ field generated by the RF pulse gains significant influence over the motion of the magnetisation, even though it is much smaller than the applied $\boldsymbol{B_0}$. By definition, the RF pulses are always applied at the Larmor frequency of a relevant nucleus to maximise their effect on the sample. Conversely, the frequencies detected in the NMR experiments are always determined relative to the *receiver* reference frequency. Since this is commonly set to be the same as the RF frequency, it follows that the detection also takes place in the rotating frame and the offsets of individual signals give rise to their frequencies in the NMR spectrum.

2.1.4 Critical NMR parameters

In the context of biomolecular NMR, the following terms need to be clarified:

Chemical shift (δ) is the position of the signal along the frequency axis, measured with respect to a reference compound, usually tetramethylsilane (TMS) or its derivative. Observed signal frequencies are proportional to the magnitude of the applied $\boldsymbol{B_0}$,

however for consistency they are quoted in a field-independent units of ppm:

$$\delta = \frac{\nu - \nu_0}{\nu_0} 10^6, ppm \tag{2.17}$$

where ν and ν_0 are the signal frequencies in Hz of the sample and reference compound, respectively. On the molecular scale, chemical shift is dependent on the close chemical environment of each non-equivalent nucleus. In principle, it is the motions of electrons that create a secondary magnetic field and perturb the applied $\boldsymbol{B_0}$. As a result, the effective magnetic field at each nucleus is marginally different. This accounts for the separation of NMR signals along the frequency axis.

Spin-spin coupling constants ($^nJ_{AX}$) represent scalar, i.e. through-bond interactions between two nuclei (A, X) linked by one or more covalent bonds (n). This coupling is field-independent and usually quoted in units of Hz.

Nuclear Overhauser effect (NOE) arises from dipolar, i.e. through-space, spin couplings with $1/r^6$ correlation to the internuclear distance (r). Therefore NOEs are most prominent for short range interactions and become specifically useful in determination of molecular structures.

Spin-lattice relaxation time (T_1) describes the rate at which the magnetisation returns to the thermodynamic equilibrium parallel to $\boldsymbol{B_0}$ after the RF pulse. T_1 is related to the rotational tumbling of molecules in solution and as such is sensitive to temperature, sample viscosity, and in case of biocompounds, local changes in structural flexibility.

Spin-spin relaxation time (T_2) is the rate of decay of effective magnetisation observed on the transverse plane after the 90° pulse. T_2 is never longer than T_1, and is related to the loss of coherence among individual spins that precess in the transverse plane and build up the macroscopic, observable magnetisation. T_2 relies on the dynamic processes governing the molecules of study, in particular it is inversely correlated to molecular size.

Linewidth ($\Delta\omega_{1/2}$) is the determinant of spectral resolution. In NMR we assume the signals take the Lorentzian line shape. In relation to those, the linewidth is described as width at half-height of the peak. In an ideal NMR experiment, carried out in a kinetically stable system, linewidth has a simple correlation to T_2:

$$\Delta\omega_{1/2} = \frac{1}{T_2}, \tag{2.18}$$

which explains the fall in resolution with increasing molecular size. In reality, linewidth can be dramatically affected by exchange process and experimental artefacts. Moreover, linewidth and T_2 are influenced by molecular mass and shape, otherwise referred to as the rotational correlation time (τ_C), which to a good approximation is expressed by Stoke's law:

$$\tau_C = \frac{4\pi\eta_w {r_H}^3}{3k_B T}, \tag{2.19}$$

where η_w, r_H, k_B, T refer to solvent viscosity, molecule's effective hydrodynamic radius, Boltzmann constant and temperature, respectively.

2.1.5 Chemical exchange

Out of the many important aspects of NMR the ability to study the time-dependent nature of molecular systems, particularly those in thermal equilibrium, makes it stand out amongst other experimental methods. The NMR experiment detects the molecular motions themselves. In consequence it provides access to a broad range of processes occurring on the nanosecond to the many seconds timescale, including the making and breaking of chemical bonds, acid-base and redox reactions, conformational changes of relatively rigid structures such as proteins, as well as protein-ligand interactions. In general, all these processes are referred to as *chemical exchange*. With few reasonable assumptions chemical exchange in the context of NMR is usually simplified to a model of a nucleus shifting between two magnetically distinct environments A and B, each being equally likely populated:

$$\mathrm{A} \underset{k_{BA}}{\overset{k_{AB}}{\rightleftharpoons}} \mathrm{B} \tag{2.20}$$

where k_{AB} and k_{BA} are the forward and reverse rate constants and the exchange constant, k_{ex}, is defined as:

$$k_{ex} = k_{AB} + k_{BA} = \frac{k_{AB}}{p_B} = \frac{k_{BA}}{p_A} \tag{2.21}$$

while p_A and p_B are the equilibrium populations of the nuclear spins in the chemical environments A and B. Considering the above, eq. (2.16) which predicts the evolution of the macroscopic magnetisation during the NMR experiment can be rewritten for A and B, including the contributions of the exchange process:

$$\frac{d}{dt}\boldsymbol{M_A} = \gamma(\boldsymbol{M_A} \times \boldsymbol{B_{eff}}) - R[\boldsymbol{M_A} - \boldsymbol{M_{0,A}}] + k_{BA}\boldsymbol{M_B} - k_{AB}\boldsymbol{M_A} \tag{2.22}$$

$$\frac{d}{dt}\boldsymbol{M_B} = \gamma(\boldsymbol{M_B} \times \boldsymbol{B_{eff}}) - R[\boldsymbol{M_B} - \boldsymbol{M_{0,B}}] + k_{AB}\boldsymbol{M_A} - k_{BA}\boldsymbol{M_B} \tag{2.23}$$

For the NMR experiment, the effects of chemical exchange depend on the relationship between processes occurring at the Larmor timescale, τ^0, i.e. the time required for nuclear spins to precess by 1 radian in the applied magnetic field, the spectral timescale, τ_{spect}, i.e. the inverse of the chemical shift separation between two distinct chemical

environments, $\Delta\omega = |\omega_A - \omega_B|$, and the spin-lattice relaxation timescale defined by T_1. Motions on the τ_{spect} timescale have direct manifestations in the lineshapes of NMR spectra with the critical value at $k_{ex} \approx 2\sqrt{p_A p_B} \times \Delta\omega$. This so called *crossover point* defines the *intermediate exchange* regime, where the ω_A and ω_B signals coalesce. At k_{ex} significantly above and below the crossover point the exchange processes have highly distinct effects on NMR spectra. The *slow exchange* regime is defined by $k_{ex} << \Delta\omega$, where the signals for ω_A and ω_B are individually well defined, on the opposite end, i.e. for $k_{ex} >> \Delta\omega$ and *fast exchange*, only a single peak is observed. The populations of A and B play a critical role in both of these cases. For slow exchange they relate to the *intensities* of the individual signals, while for fast exchange it is the *frequency* of the observed signal that is is averaged by the population difference. The characteristics of the three exchange regimes are presented in fig. 2.3.

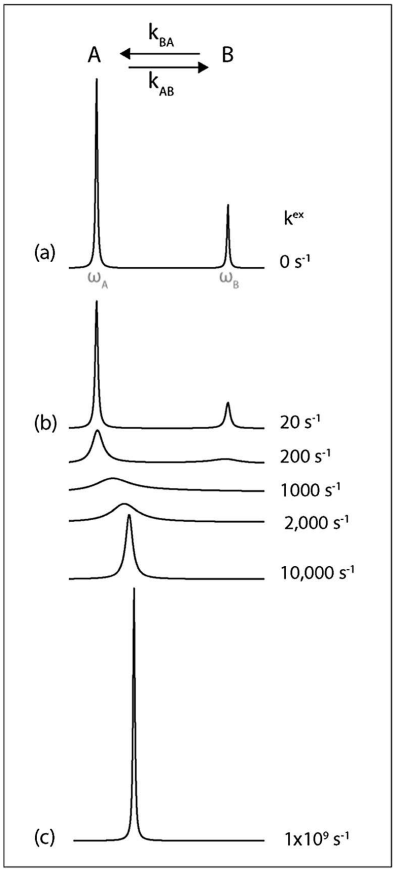

Figure 2.3: Simulated ^{1}H spectra for nuclei in a two-state exchange model. The ratio between the chemical shift difference ($|\omega_A - \omega_B|$) and exchange rate (k^{ex}) is the ground for characterisation of the (a) slow-, (b) intermediate-, and (c) fast-exchange regimes, which determine spectral appearance. Figure reprinted from Farber and Mittermaier[40]. Copyright 2015, with permission from Springer Nature.

2.2 Sensitivity and resolution

The sensitivity and resolution parameters are of critical importance to NMR. Sensitivity is defined as the minimum amount of sample needed to produce a signal clearly above the noise level, while resolution dictates how well the individual signals in the spectrum can be differentiated. The main limitation to sensitivity in NMR relates to the separation of the nuclear spin energy levels, which is few orders of magnitude lower in comparison to other spectroscopic methods. One of the main sensitivity measures is the signal-to-noise ratio (SNR) formulated by Abragam [1] as comparison of the intensity of the observed signal to the root mean square of the noise floor. It can be shown that[167]:

$$SNR \propto [\gamma \boldsymbol{B_0}] \left[\frac{\gamma^2 \, h^2 \, \boldsymbol{B_0} \, N_s}{16\pi^2 \, k_B \, T} \right] \left[\frac{\boldsymbol{B_1}}{i_c} \right] \left[\frac{1}{V_{noise}} \right] \tag{2.24}$$

where N_s the number of spins per unit volume, $\frac{\boldsymbol{B_1}}{i_c}$ is the coil sensitivity defined as the coil magnetic field per unit current, V_{noise} is the noise voltage which has contributions from both the sample and the detector, while h and k_B are the Planck's and Boltzmann's constants, respectively. The above gives a rather complex account of the SNR, however most of the defining parameters are either natural constants or relate to the sample conditions, such as temperature or number of spins. It follows that one of the main sensitivity gains is associated with an increasing magnetic field. In fact, truly groundbreaking improvements in NMR sensitivity were made over the last 50 years, mainly as consequence of the discovery of superconducting materials. As result, iron magnets capable of reaching up to 2.35 T are now replaced by modern superconducting instruments operating at 14 - 28 T. Further sensitivity enhancement is offered by cryocooled probes, which limit the thermal noise generated by the motions of the electrons in the receiver circuitry, reflected by V_{noise} in eq. (2.24). This offers 2 - 4 times better SNR per unit time in comparison to conventional ambient temperature probes[79,167].

In eq. (2.24) the only element directly related to the RF coil is the $\frac{\boldsymbol{B_1}}{i_c}$, which can be optimised by choosing the proper coil geometry for the sample that will maximise the number of spins in the homogeneous $\boldsymbol{B_1}$ volume[37,38]. This approach has been assumed specifically for mass- and volume-limited samples, where the NMR signal is notably improved by using miniaturised detectors that closely coincide with the sample[48,121,122,168]. Further sensitivity improvements are achieved for systems that employ both detector miniaturisation and cryocooling, as demonstrated by Brey et al. [16]. An entirely separate avenue for increasing sensitivity of the NMR experiment is *hyperpolarisation*, where population differences much greater than those at thermal equilibrium are imposed on the sample. Methods involved are associated either with transferring the polarisation from electrons to nuclear spins or the transfer of para-hydrogen spin order through catalysed chemical association. Currently, these techniques hold great promise to NMR as up to 10,000-fold signal enhancements have been reported[6,42].

In practice, the SNR is routinely amplified by *signal averaging*, i.e. repeated acquisition and summation of the resulting spectra. The improvement comes from the fact that the NMR signals are reproducible, whilst the noise is essentially random. For the acquisition repeated N times the signal intensity improves accordingly, however the noise is raised only by a factor of $\sqrt{N}$, therefore the overall SNR scales up as a function of $\sqrt{N}$, allowing for the NMR signals to be extracted out of the noise. The setback of this approach is such that it becomes time consuming, especially for extended pulse sequences and/or molecules with long spin-lattice relaxation times, T_1. An improvement of $5 * SNR$ requires repetition of the same experiment 25 times, while $10 * SNR$ gain can only be achieved with a 100 repetitions. In individual cases this might require hours or even days of experimental time.

As exemplified by eq. (2.24) multiple factors, often specific to the sample, influence the SNR while the acquisition time is completely omitted. This makes the SNR not an adequate parameter when comparing sensitivities of different detectors[85]. Instead, the specific sensitivity measure, S, was introduced[168], a function of SNR taking into account sample conditions such as mass (m) or concentration (C) and the overall acquisition time (t_{acq}):

$$\begin{aligned} S_c &= \frac{SNR}{C\sqrt{t_{acq}}} \\ S_m &= \frac{SNR}{m\sqrt{t_{acq}}} \end{aligned} \tag{2.25}$$

However, scaling with the total acquisition time bears it's own problems, e.g. the contribution of the repetition delay needs to be accounted for as it reflects the T_1 of the sample. This has prompted Lepucki et al. to propose the normalised limit of detection ($nLOD$) measure for comparison of different NMR setups, which describes the detector performance independent of measurement parameters[85]. In the frequency domain the mass-$nLOD$ is defined as:

$$nLOD_f^m = \frac{3n_s\sqrt{\Delta f}}{SNR\sqrt{N}} \tag{2.26}$$

where n_s is the sample amount in mol, Δf is the set receiver bandwidth, SNR is measured for a single scan and N is the number of measurement points per scan.

In the case of resolution, the critical role plays the homogeneity of the applied magnetic field. However, $\boldsymbol{B_0}$ is never perfectly homogeneous as it is being distorted by the imperfections of the experimental setup, such as magnetic susceptibilities introduced by the instruments or the sample. As result, the nuclear spins will experience slightly different magnetic fields depending on their position within the sample, which will be reflected by their Larmor frequencies and therefore the reported chemical shifts. The pronounced effect is broadening of the spectral peaks, which affects both their

linewidth and amplitude, making signals that are close to each other difficult to distinguish. Other characteristics specific to the sample, i.e. the T_2 which is inversely correlated to the linewidth, will also affect the spectral resolution which is defined by the linewidth and SNR:

$$\varepsilon = \frac{\Delta\omega_{1/2}}{\sqrt{SNR}} \tag{2.27}$$

2.2.1 The Transmission Line Probe

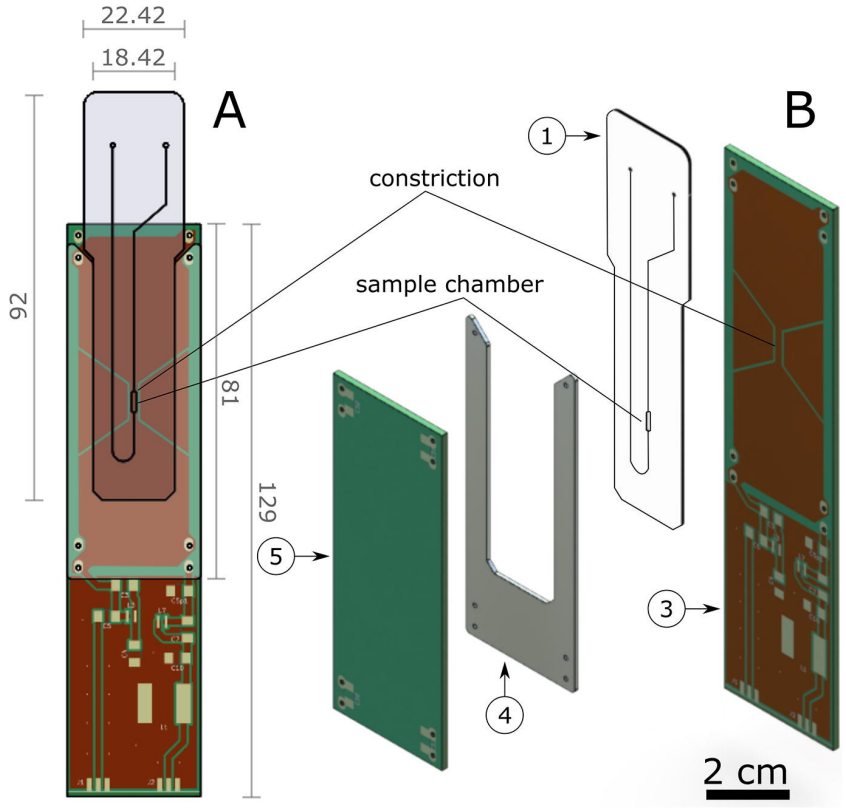

Figure 2.4: Schematic representation of the TLP detector assembly, including the microfluidic device. In the front view (A) the position of the generic microfluidic device (1) is shown, such that the constriction of the detector coincides with the sample chamber in 1. In the exploded view (B), the two planes (3 and 5) of the detector are visible, plus the spacer (4) which ensures the correct position of 1. All measures are expressed in mm, unless stated otherwise. Figure reprinted from Sharma and Utz[150] with permission from the authors. Copyright 2019, with permission from Elsevier.

This work employs the transmission line probe (TLP) specifically designed to accommodate planar microfluidic devices[47,150,186]. The TLP design derives from the stripline NMR detector, proven to give $\sqrt{2}$ improvement in SNR when compared to the conventional helical coil of the same volume[38]. The detector geometry is presented in fig. 2.4, featuring two conducting planes with a constriction that concentrates the RF field and sensitivity onto the sample area of the microfluidic device. The detector is

mounted onto an aluminium scaffold compatible with a standard NMR spectrometer. The modular design of the TLP allows for fast optimisation of the detector, where different designs and geometries can be explored. The current setup is optimised for proton detection at 14 T with a second channel tunable to ^{13}C or ^{15}N.

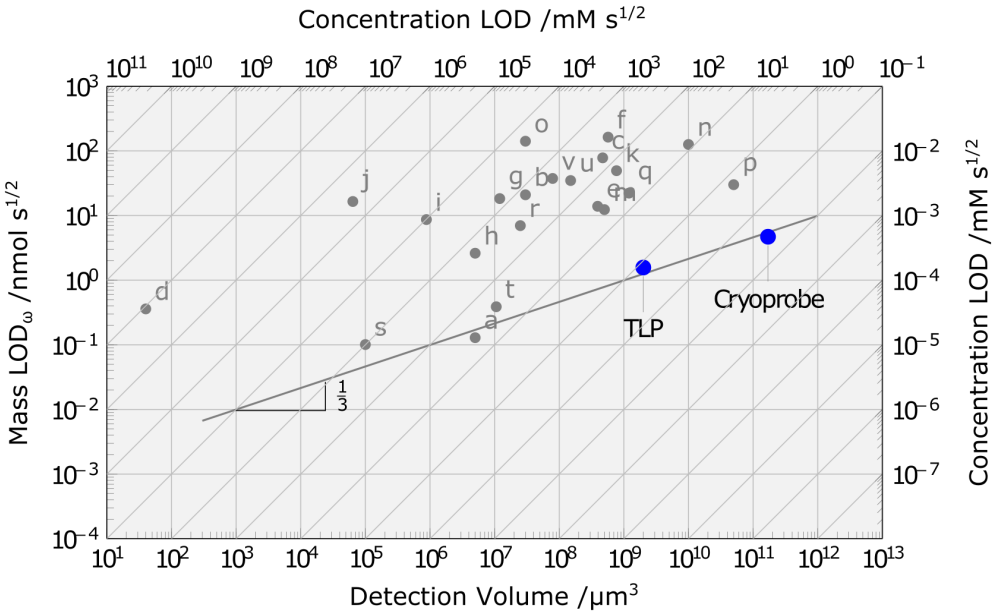

Figure 2.5: Performance profile of the the TLP in comparison to other micro-NMR detectors and a commercially available Cryoprobe (Bruker, US). The references describing individual micro-NMR detectors (a-u) are listed in table B.1 in the appendix.

The performance of the TLP in comparison to other micro-NMR detectors described in the literature is presented in fig. 2.5. The detection volume is plotted on the x-axis, while the y-axis and the diagonal represent the mass- and concentration-LOD, i.e. the inverse of the sensitivity parameters presented in eq. (2.25). All considered micro-NMR (μNMR) detectors are listed in table B.1, including the relevant publications. The TLP is highlighted in blue along the commercially available TCI cryoprobe (Bruker, US) operating on ~ 500 μL samples. As can be noted the TLP performance aligns with the general trend of decreasing $nLOD$ with size, highlighted by the solid line of gradient 1/3. The main advantage for this detector is associated with improved mass sensitivity, which is approximately one order of magnitude better than the cryoprobe, however comes with the concentration-LOD penalty which is correspondingly reduced.

2.3 Practical aspects of protein NMR

2.3.1 Representation of the NMR pulse sequences

As explained in section 2.1.2 the detection of the NMR signal takes place when the magnetisation is perturbed in a direction perpendicular to the applied magnetic field, i.e. the transverse plane. These perturbations are caused by irradiation of the sample with RF pulses, where the timing of the pulse determines the angle of rotation. According to the vector model the maximum signal in the transverse plane is recorded when the magnetisation is tilted 90° away from the equilibrium position, hence the standard pulse-acquire NMR experiment contains a single 90° pulse, immediately followed by the acquisition of the FID signal. The depiction of this experiment is shown in fig. 2.6, where the 90° pulse is represented by a single block on the time axis. In a standard NMR pulse sequence representation, the thickness or colour of the block will relate to the angle of rotation, while additional information may also specify the phase of the RF pulse. The more complex NMR experiments are built by multiple pulses and delays designed to shift the populations and coherences of the density matrix, which is reflected in the detected NMR signal.

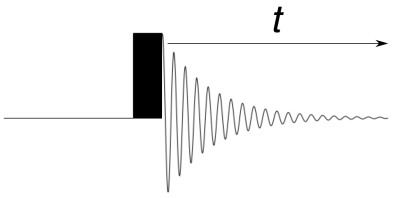

Figure 2.6: Standard representation of an NMR pulse sequence. Horizontal line represents the experiment time axis, coloured blocks symbolise individual RF pulses while decaying oscillating wave is the detected FID signal during the acquisition period, t.

2.3.2 Coupled spins and coherence transfer

So far only individual spins or an ensemble of non-interacting spins have been considered, however real samples consist of complex molecules where spins interact with each other. The simplest model for such system is a pair of coupled spins-1/2, defined by the following wavefunction:

$$|\psi\rangle = c_{\alpha\alpha}|\alpha\alpha\rangle + c_{\alpha\beta}|\alpha\beta\rangle + c_{\beta\alpha}|\beta\alpha\rangle + c_{\beta\beta}|\beta\beta\rangle \tag{2.28}$$

After application of a 90° pulse on this system at equilibrium, the resulting transverse magnetisation may be represented as four vectors in the rotating frame, as shown in fig. 2.7 A. Those are related to the transitions of individual spins between the $|\alpha\rangle$ and

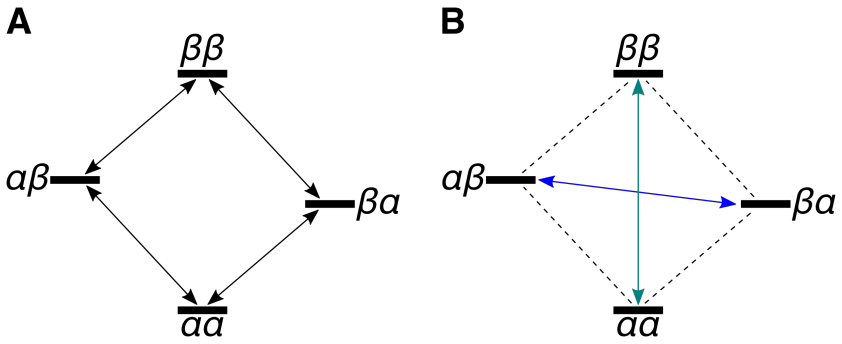

Figure 2.7: The energy diagram for a coupled two-spin system. In (A) only the observable single quantum coherences, associated with the individual spins' transitions between available energy states, are presented as arrows. In (B) the non-observable zero quantum coherence and double quantum coherences are highlighted in blue and gray, respectively.

$|\beta\rangle$ states. In each one of these cases a single transition between $+1/2$ and $-1/2$ states results in a coherence order $p = \pm 1$, which is otherwise known as a single quantum coherence (SQC). Two other transitions are possible where both of the coupled spins change their states, as visualised in fig. 2.7 B. The coherence order in these cases is $p = 0$ for the transitions between the $|\alpha\beta\rangle$ and $|\beta\alpha\rangle$, and $p = \pm 2$ for the transitions between $|\alpha\alpha\rangle$ and $|\beta\beta\rangle$, defined as the zero quantum coherences (ZQCs) and double quantum coherences (DQCs), respectively. This distinction is relevant since the quantum mechanical selection rules dictate that only single quantum coherences can induce magnetisation on the detection coil, therefore those are the only directly observable coherences in the NMR experiment. Coherence transfer on the other hand is possible regardless of the coherence order, however in solution limited only to the J-coupled spins. Exploring the coupling connections becomes extremely important for multidimensional NMR experiments.

2.3.3 Coherence selection

As highlighted above, all possible coherences evolve according to the sequence of delays and pulses during the NMR experiment, however, this might lead to a distorted spectrum if the right coherences are not selected during the pulse sequence. Two methods can be employed to achieve this goal. Through *phase cycling* the pulse sequence is repeated several times over almost identically. The only difference is applied to the *phases*, $\Delta\phi$, of the designated RF pulses. For pulses which change the coherence order, those coherences acquire a phase shift which propagates through the remainder of the pulse sequence. Sequences repeated multiple times, each time with different $\Delta\phi$, when combined allow for the desired signals to add up coherently while all others are cancelled out and do not appear in the resulting spectrum. *PFGs* on the other hand deliberately cause the main magnetic field, $\boldsymbol{B_0}$, to become inhomogeneous for a short

period of time. As result, any coherences present dephase rapidly, however, this can be reversed by applying a second PFG. Therefore, by careful choice of the duration and position of the two PFGs in the pulse sequence one can assure that only the coherences of interest are rephased. Each of the two methods come with significant considerations. For complex multi-pulse sequences the appropriate coherence selection pathway via phase cycling may result in significantly extended experimental time, while application of PFGs can only be carried out by specifically designed gradient coils, which are not standard for every NMR probe.

2.3.4 Multidimensional NMR experiments

Although the initial ideas for two-dimensional NMR were presented by Jean Jeneer in 1971, the first experiments were actually carried out few years later by Aue et al.[8]. This innovation has proven truly revolutionary for biomolecular research, greatly expanding the ability to determine the structures of molecules. The special utility of 2D NMR originates from the fact that these techniques can fully exploit the through-bond (*J*-coupling) and through-space (NOE) spin interactions within, but also between biomolecules. Individual interactions between the spins are either homo- or heteronuclear, the former most commonly relates to the ^{1}H-^{1}H couplings while the latter to ^{1}H-^{13}C and ^{1}H-^{15}N. In protein NMR, the regular distribution of spin interactions, e.g. as for the amide NH *J*-couplings in the peptide bonds, allows for interrogation of all residues of the polypeptide chain while they remain individually resolved in the frequency domain.

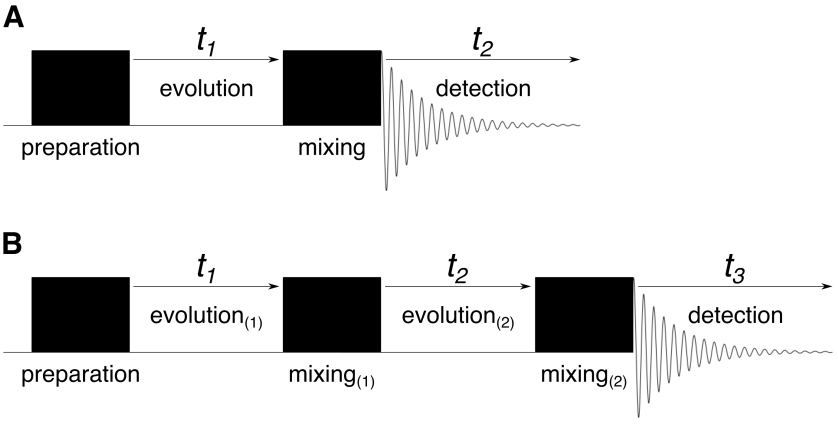

Figure 2.8: The general scheme for two- (A) and three-dimensional (B) NMR experiments.

From the experimental perspective, the generation of the second frequency dimension is relatively simple. Regardless of the exact pulse sequence, the experiment can be subdivided into four distinct periods: preparation, evolution, mixing and detection, as presented in fig. 2.8 A. The detection period is entirely analogous to the 1D format,

preparation and mixing are build by a single pulse or a set of pulses specific to each 2D experiment, and the evolution period is critical to the generation of the second frequency dimension. Therefore specific "acquisition times", t_1 and t_2, are defined for each dimension. The term "acquisition time" can be misleading because it's only the frequencies of the detection period that are being observed directly and therefore constitute the primary (horizontal) axis of the NMR spectrum. The signal in the second dimension is generated by sampling the increasing duration of the t_1 evolution period, as presented in fig. 2.9, which adds an amplitude modulation to the directly detected t_2 signal. The t_2 and t_1 time domain signals are Fourier transformed which results in a 2D spectrum where individual peaks arise at the maximum amplitudes of both the frequency domains. This approach can be expanded further by addition of another incremented evolution period in the pulse sequence, giving rise to a new dimension of the experiment, as presented in fig. 2.8 B. Critically, as no direct observations are made during the evolution period, the coherences evolving through t_1 can be the non-observable ZQCs and DQCs. Those are converted into the observable single quantum coherences in the following mixing period.

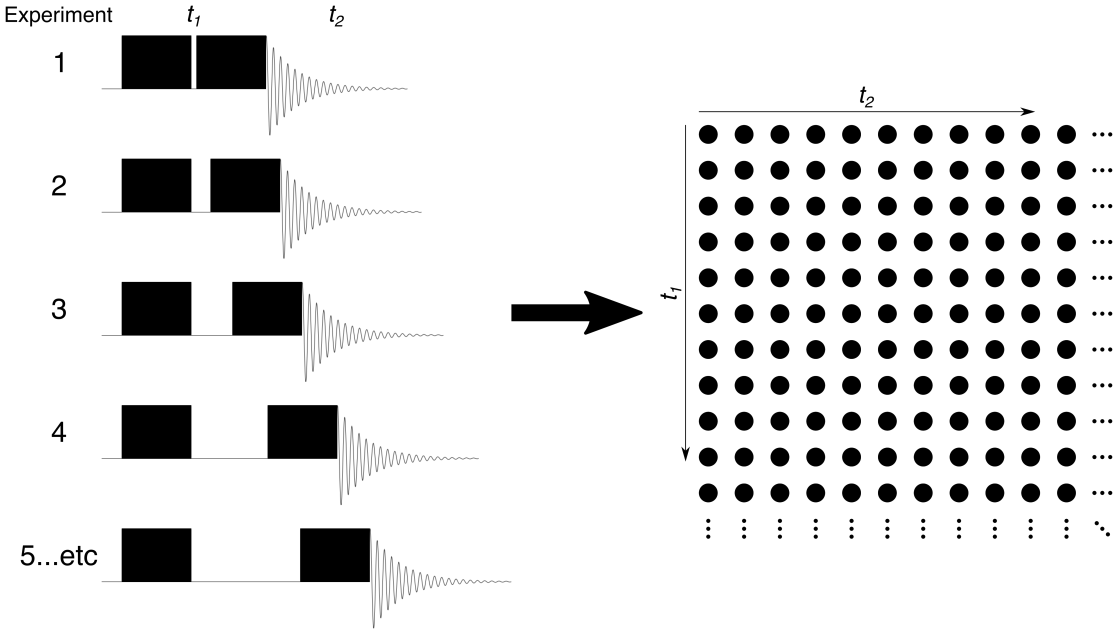

Figure 2.9: The principle of NMR data acquisition in two dimensions. The primary dimension comes from the directly observed FIDs during the t_2 acquisition. The second dimension is generated indirectly through incrementation of the t_1 period in the pulse sequence, which adds an amplitude modulation to the observed FID. Spectra are produced by successive Fourier transformation of the t_2 and t_1 data.

2.3.5 Homonuclear correlation spectroscopy

One of the reasons that make NMR such a powerful technique is that it provides the means to identify the physical correlations between individual atoms, which are

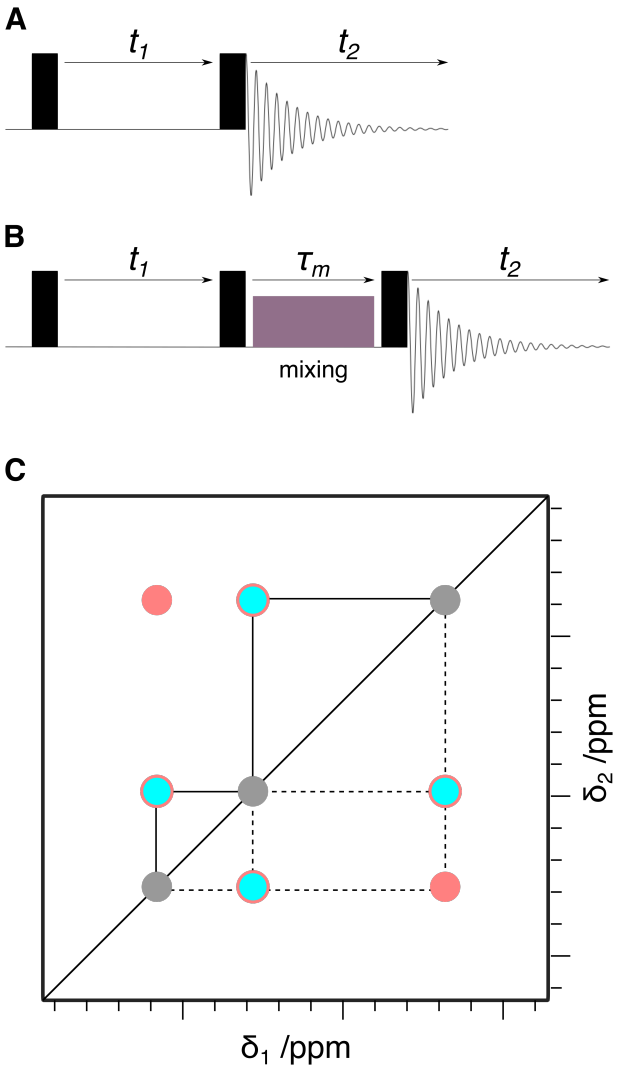

Figure 2.10: The standard pulse sequences for the COSY (A) and TOCSY (B) experiments. During the mixing period in the TOCSY experiment a series of pulses are executed which transfer coherences between spins connected via an unbroken network of *J*-couplings. In the schematic representation of the resulting spectra (C) in grey are the diagonal peaks, in light blue with pink outline are the cross peaks present in both spectra while the pink signals are the cross peaks which are generated as a consequence of the mixing period in the TOCSY experiment. The solid and dotted lines demonstrate the covalent bond relationships that can be extracted from the COSY and TOCSY spectra, respectively.

manifested in the spectrum. This ability cannot be overstated for organic chemists, who use it everyday to characterise newly synthesised chemical compounds. Correlation spectroscopy experiments rely on the *J*-coupling network within the molecule and in consequence allow to resolve the covalent bond arrangements between individual signals. The standard COrrelation SpectroscopY (COSY) and TOtal Correlation SpectroscopY (TOCSY) pulse sequences as well as the schematic representation of the resulting spectra are presented in fig. 2.10. The COSY pulse sequence is composed of two 90° pulses separated by the t_1 evolution period. The first pulse generates the

single quantum coherences which evolve over t_1, and the second RF pulse is used to convert the individual coherences into every other coherence in the coupled spin system. In the resulting spectra two types of peaks can be observed. Those at the same frequencies in both dimensions populate the diagonal of the spectrum and represent the self-correlated spins. These peaks offer no additional information in comparison to a standard 1D spectrum. The second type of peaks are called cross-peaks and appear on the off-diagonal of the spectrum. Cross-peaks are only observed for spins that have a direct J-coupling to the diagonal, therefore they provide critical information about the chemical bond network within a molecule. An expanded pulse sequence, i.e. TOCSY shown in fig. 2.10 B, allows to resolve all signals from spins connected via an unbroken network of J-couplings. The TOCSY experiment employs a series of pulses arranged in a repetitive sequence which constitute the *isotropic mixing* period, where the coherences are relayed along the continuous chain of J-couplings. The duration of the mixing period, τ_m, determines the extent of propagation of the coherences between the coupled spins, where longer mixing times are needed to resolve the long-distance correlations. However, mixing times above 100 ms are rarely effective as they incur a significant sensitivity loss due to relaxation. The COSY and TOCSY spectra are usually recorded together as their additive information allows to quickly identify the single- and multiple-bond connections within the molecule.

2.3.6 Heteronuclear magnetisation transfer

Similar to the ^{1}H-^{1}H correlations considered in the previous section, individual J-couplings can be utilised specifically to transfer magnetisation between ^{1}H, ^{13}C and ^{15}N. As the detected NMR signal is ultimately dependent on the size of the equilibrium magnetisation generated at the start of the experiment, the sensitivity in NMR is dictated mainly by the gyromagnetic ratio and the strength of the applied magnetic field, as defined by eqs. (2.11) and (2.12). Since the γ of ^{1}H is approximately 4 - 10 times that of ^{13}C and ^{15}N while the $\boldsymbol{B_0}$ remains the same for all, the detected proton signals in the NMR experiment are consequently stronger than those for ^{13}C and ^{15}N. The Insensitive Nuclei Enhanced by Polarisation Transfer (INEPT) experiment allows to compensate this difference by transferring the larger equilibrium magnetisation generated on ^{1}H to the low γ nuclei of ^{13}C and ^{15}N. Furthermore, the repetition rate of the experiment, determined by the T_1 of the examined species, can be greatly increased as the proton T_1 is generally much shorter than that of the other nuclei. The refocused INEPT pulse sequence is shown in fig. 2.11 considering a heteronuclear spin-1/2 pair IS, where I signifies the high sensitivity nucleus (^{1}H) and S relates to ^{13}C or ^{15}N. The initial 90° pulse generates the transverse magnetisation on I while the following (1) period, including the 180° pulse on both channels, is designed to evolve the J_{IS}-coupling as the chemical shift is refocused. The second (2) period consists of two 90° pulses that cause the coherence transfer from I to S. This constitutes the actual INEPT pulse sequence,

however the refocused INEPT employs another (3) period analogous to (1) to maximise the amplitude of the signal detected on S. Likewise, the timings of the τ_1 and τ_2 delays are adjusted to give the strongest S signal, which is recorded for $\tau_1 = \tau_2 = 1/(4J_{IS})$. However, in a real molecule different couplings are present and each will show distinct enhancement factor depending on the choice of the delay time. Shown in grey in fig. 2.11 is the decoupling applied on I during detection which effectively reduces the J_{IS} to zero giving rise to a single peak detected in the S frequency domain.

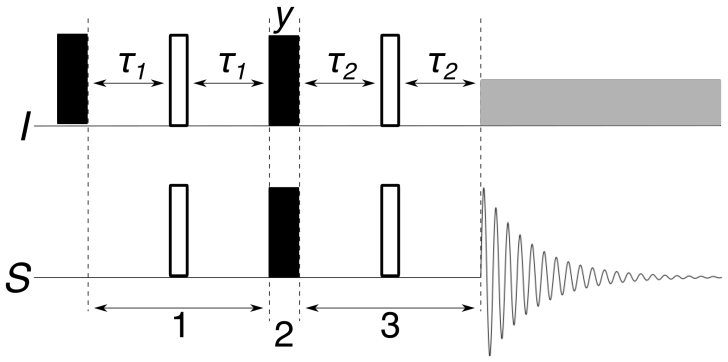

Figure 2.11: Representation of the refocused INEPT pulse experiment. Three periods can be singled out during the pulse sequence. During period 1 ,both spin offsets are refocused through application of the 180° pulse (open rectangle) while the J-couplig is allowed to evolve. Period 2 consists of two 90° pulses, executed simultaneously on both spins transferring the magnetisation from spin I to spin S. In period 3, the pulses from period 1 are repeated for the same effect before the acquisition is carried out. The optimum value for both τ_1 and τ_2 delays is $1/(4J_{IS})$

The INEPT pulse sequence has become one the main building blocks of modern multidimensional NMR experiments, often executed in an out-and-back scheme, where the magnetisation is both generated and detected on ^{1}H, while specific pulses and delays of the t_1 evolution and mixing periods are applied to generate the indirectly detected coherences.

2.3.7 Heteronuclear quantum coherence correlation spectroscopy

The ability to record single-bond correlations between ^{1}H, ^{13}C and ^{15}N atoms is of the upmost importance for protein NMR, as those are regularly distributed within the polypeptide chain. For this purpose two types of experiments are distinguished, Heteronuclear Single Quantum Coherence (HSQC) and Heteronuclear Multiple Quantum Coherence (HMQC), both of which provide essentially equivalent correlation data, however exploit different pathways for the coherence transfer. The main advantage of these methods comes from the ability to disperse the usually crowded protein ^{1}H signals according to their heteronuclear shift. The general scheme for the magnetisation transfer carried out during the HSQC/HMQC experiments is presented in fig. 2.12, while the corresponding pulse sequences are shown in fig. 2.13.

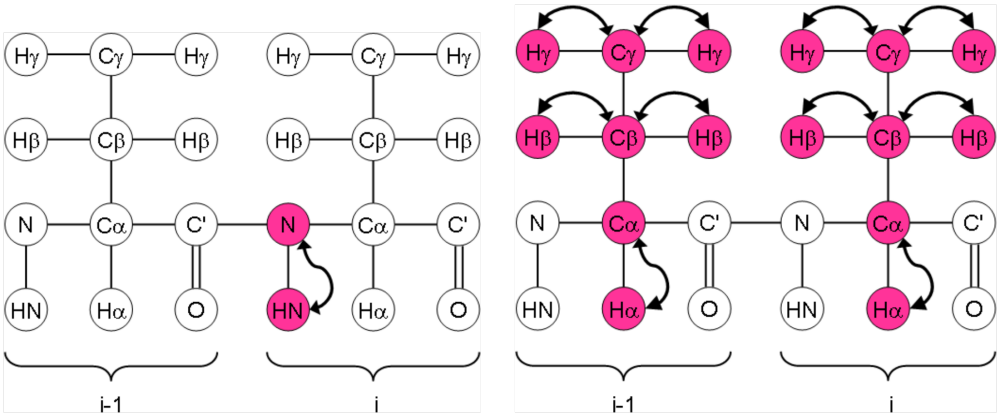

Figure 2.12: Diagram representing the magnetisation transfer carried out during the most common heteronuclear 2D protein experiments. ^{1}H-^{15}N HSQC (left) allows to correlate covalently bound proton and nitrogen atoms of the protein amide groups while the ^{1}H-^{13}C HMQC (right) achieves the same for proton - carbon pairings of the methyl, methylene and methine groups. Figure reproduced from 'Protein NMR: A practical guide' (https://www.protein-nmr.org.uk/) with permission from the author.

Both HSQC and HMQC experiments are build by two INEPT-like sequences separated by the t_1 evolution period for the heteronuclear chemical shift. The initial (1) periods of the HSQC and the INEPT pulse sequences are essentially the same, generating the transverse magnetisation on I, followed by the evolution of the J_{IS}-coupling and coherence transfer to S. During the t_1 period, a single 180° pulse is applied on I to refocus the J_{IS}-coupling, while a single quantum coherence evolves on S. Subsequently, a reverse INEPT is carried out which transfers the magnetisation back to I for detection, while the decoupling is applied to the S channel. Likewise, in the HMQC experiment the initial magnetisation is generated by a 90° pulse on I, which after the delay τ is transferred into a multiple quantum coherence on S by a 90° pulse. The t_1 period again serves to evolve the chemical shift on S, while it is refocused on I by a 180° pulse. Another 90° pulse on S transfers the magnetisation back to I, which is allowed to evolve into the observable single quantum coherence over the second delay τ before detection. Again, the intensity of the detected signal depends on the delay times and is optimal for $\tau_1 = \tau_2 = \tau/2 = 1/(4J_{IS})$. Despite the differences in the two pulse sequences the resulting spectra are largely the same and the experiments can be applied alternately. However, the HSQC offers superior sensitivity and resolution in the indirect dimension therefore it remains the most commonly used heteronuclear correlation technique. The advantages of the HMQC on the other hand relate to the simpler pulse sequence and exploration of specific relaxation properties of the multiple quantum coherences, which can be beneficial for the ^{1}H-^{13}C couplings. Furthermore, an improved version of the HMQC sequence was developed, i.e. the band-Selective Optimised Flip Angle Short Transient (SOFAST) HMQC, which limits the total experimental time to

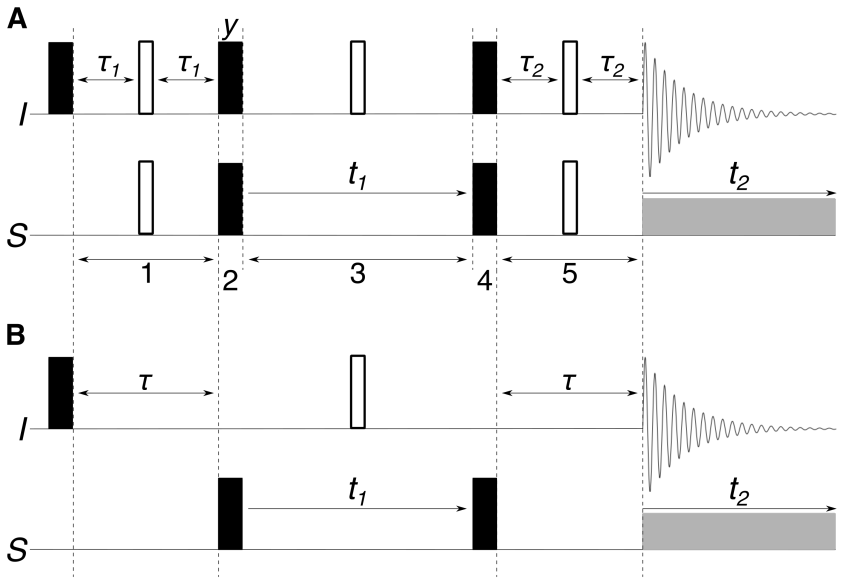

Figure 2.13: The pulse sequences of the HSQC and HMQC experiments. 90° and 180° pulses are represented by filled and open rectangles, respectively. The initial periods (1 and 2) are equivalent to the INEPT pulse sequence and serve to transfer the magnetisation from the highly sensitive I nucleus to the S. The t_1 evolution period (3) follows, before the magnetisation is transferred via reverse INEPT (4 & 5) to I for detection. Grey squares represent the decoupling pulses applied on the S channel during acquisition.

only few seconds, therefore providing the framework for high-throughput NMR studies[53,142,143]. This experiment can be easily implemented using the modern commercial NMR systems, however, due to fast pulse repetition and incorporation of PFGs on top of the double channel requirements it poses notable challenges for the non-standard hardware.

2.4 Protein NMR, the applications outlook

2.4.1 Background

In biomedical research NMR is very highly regarded. It is one of only few methods that provide atomic scale resolution, essential in the field of structural biology. However, the modern-day technique of choice in determining biomolecular structure is X-ray crystallography (XrC). This method, revolutionised by introduction of synchrotron radiation in the 1970s[127], today accounts for over 90 % of all structural data deposited on the RCSB protein data bank (https://www.rcsb.org). The main advantage of XrC is high atomic resolution and potential application to all types of proteins, irrespective of molecular weight, solubility or complexity. On the other side, the fundamental restraint is the ability to obtain uniform macromolecular crystals formed by the object of

interest, a process that is notoriously strenuous and based on a repeated trial-and-error approach[107]. Finally, crystallization drives the molecular system into a highly ordered state with constrained flexibility. Indeed, it is the most ordered structures that provide best structural information, while resolution falls drastically for intrinsically disordered and flexible regions[177]. This drawback, despite unquestionable importance of XrC in biomedical research, reveals significant limitations of the method to describe real-life behaviour of life systems. Biological molecules live predominantly in an aqueous environment, with substantially higher degrees of freedom, an aspect that is especially important for the primary functional elements of life, i.e. proteins. In fact, importance of structural flexibility on protein activity, first characterised for haemoglobin[123], is well recognised in biomedical research[105]. This is the area, where introduction of NMR becomes particularly advantageous.

2.4.2 The historical stand

Contemporary protein NMR owes a great deal to the ground-breaking work carried out in the 1980s by Kurt Wüthrich and Richard Ernst, for which both were awarded the Nobel prize. The field has moved considerably since, however the principles first outlined for two-dimensional experiments[8] are still fundamental for many pulse sequences used to gather biomolecular NMR data. Modern day protein NMR is based on multidimensional experiments, detecting chemical shifts of different nuclei based on their correlation, either through *J*-couplings or NOEs. Because of the character of *J*-couplings, heteronuclear experiments are preferred due to more effective transfer of magnetization between distinctive γ nuclei[12], resulting in higher resolution spectra. Those however require incorporation of NMR-active nuclei into the protein structure, considerably raising the cost and complexity of sample preparation. In resolving molecular structures, experiments utilising the NOE are most useful, with the ability to detect interactions within 6 Å distance. *J*-couplings in turn provide valuable information on the arrangement of covalent bonds and backbone dihedral angles[25,45]. Universal approach in protein NMR requires assignment of each resonance signal, a process that is lengthy and complex, however provides a unique opportunity to investigate the behaviour of every single atom in the structure.

2.4.3 Applications and perspectives

The main characteristics of NMR is the ability to study molecules in solution and access a broad range of timescales[110], which cover crucial biological processes such as enzymatic catalysis, signal transduction, ligand binding or allosteric regulation[100]. Indeed, with XrC being such a dominant technique for structural biology, the focus on dynamic chemical phenomena has become the main application of NMR within

and outside protein study. Here it is important to mention the influence of dynamic processes, namely molecular tumbling, on the experimental result. In NMR, resolution is intrinsically linked to molecular weight, for that reason the detection limit for proteins stands at approximately 50 kDa. Nonetheless, this value falls well within the expected molecular weight of an average globular protein domain[151] making NMR applicable for a broad range of targets. On the other hand, the ability to probe protein dynamics renders NMR very well suited to study weak interactions and low-affinity complexes. Coincidentally those are often responsible for driving biological processes. In particular, protein-ligand interactions are the point of focus to the pharmaceutical industry, where NMR has become especially useful in fragment-based drug discovery (FBDD). Here, through a hit-and-miss approach an entire library of fragments, i.e. small compounds below 300 Da, is screened against a known protein target to identify high quality interactions. In successive steps positive hits are further optimised to lead-like compounds. Efficacy of this approach can be exemplified by, amongst others, the recent development of inhibitor drugs for myeloid cell leukaemia 1 (Mcl-1)[49].

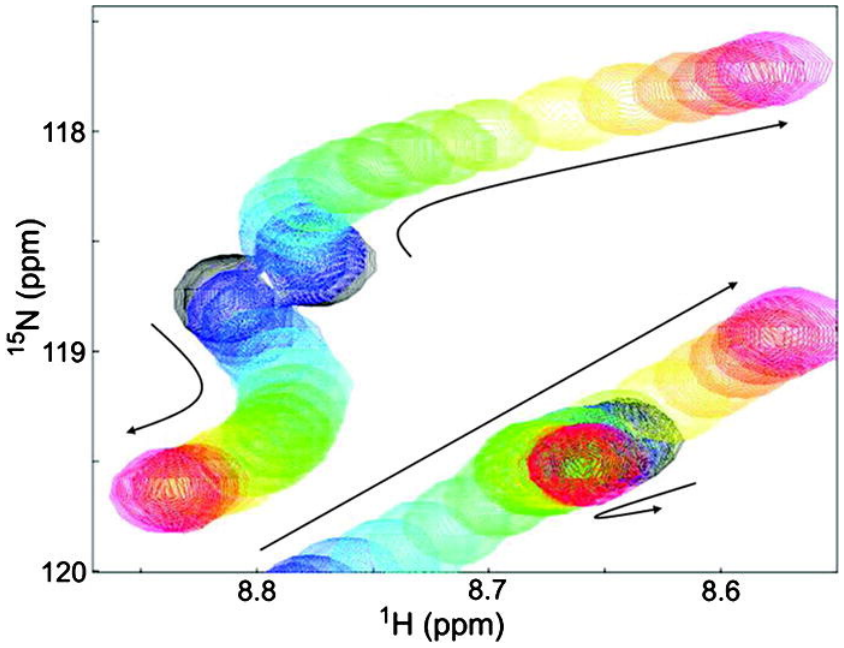

Figure 2.14: A small region of the ^{1}H-^{15}N HSQC spectrum of the TAZ2 protein titrated with p53 AD1 domain. Observed are the CSPs of the protein signals in response to the increasing ligand concentration. Peak colouring relates to the concentration ratio between TAZ2 and p53 AD1, from black for the free protein to magenta for 1:5 ratio, arrows indicate the CSP trajectories for individual signals. Figure reprinted from Arai et al.[5]. Copyright 2012, with permission from the American Chemical Society.

At the current state of affairs, when planning an NMR experiment one needs to take into account primarily the timescales of interrogated interactions and secondly their kinetic profile. By far, the simplest analysis can be carried out based on the population-averaged signals observed for a two-state model in fast exchange regime, with a range

of experiments available of both ligand-observed and protein-observed perspective[50]. The richest set of information is gathered by following the chemical shift perturbations (CSPs) of protein signals in response to the changing ligand-to-protein molar ratio, a characteristic of the fast chemical exchange. This method is very well suited to identify quantitative characteristics of the interactions, such as the binding constant (K_D), as well as more specific information about the binding mode. Conformation changes, number of binding sites, allosteric regulation, differences between specific and non-specific binding can be readily inferred from a relatively simple 2D spectrum[50,173], provided an adequate kinetic model is given. Armed with an appropriate software one can even start to predict the orientation of the ligand within the binding site[30]. Major drawbacks of this type of experiments arise from sample quality (isotope labelling) and quantity (milligrams) requirements, that significantly raise the cost of production. Moreover, extraction of the most intricate information often requires extensive data analysis reliant on resonance assignment.

Operating under the same model, a range of ligand-observed methods are also available to further characterise protein-ligand interactions. Saturation transfer difference (STD)[104] and Water-LOGSY[27] are two 1D experiments commonly employed in early stages of FBDD to identify effective binding moieties from broad libraries of fragments. Both require high ligand excess and significant size difference between the two binding partners. In fact, the difference in molecular weight between free and complexed, i.e. bound ligand, provides ground for detection due to disparate relaxation properties. For this reason, the above methods are especially well suited to study interaction profile of large proteins, otherwise inaccessible for NMR. Furthermore, with introduction of NOE-based experiments simultaneous analysis of a large compound mixtures has now become possible[21]. Adding this to other major advantages of ligand-observed NMR methods, i.e. low protein requirement and no need for isotope labelling, it is clear to notice their applicability for high throughput screening of fragment libraries. However, this approach falls short in later stages of the process where structural information, provided by either NMR or XrC, is necessary to build lead-like compounds. Likewise, accuracy drops when interrogated interactions occur beyond the two-state kinetic model.

Outside the fast exchange regime NMR study of protein-ligand interactions becomes significantly more complicated, however not impossible. CPMG relaxation dispersion[94] and ZZ-exchange[41] are two experiments designed to access the intermediate- to slow- and slow-exchange processes, respectively. Here, data analysis is based on linewidths and intensities of protein signals. This poses serious challenges and requires good understanding of underlying physical processes that govern relaxation properties of the interrogated species and affect the measured quantities. Nevertheless, unique capabilities of those methods open further doors for protein NMR, where

both have become particularly advantageous in studying the dynamics of intrinsically disordered proteins.

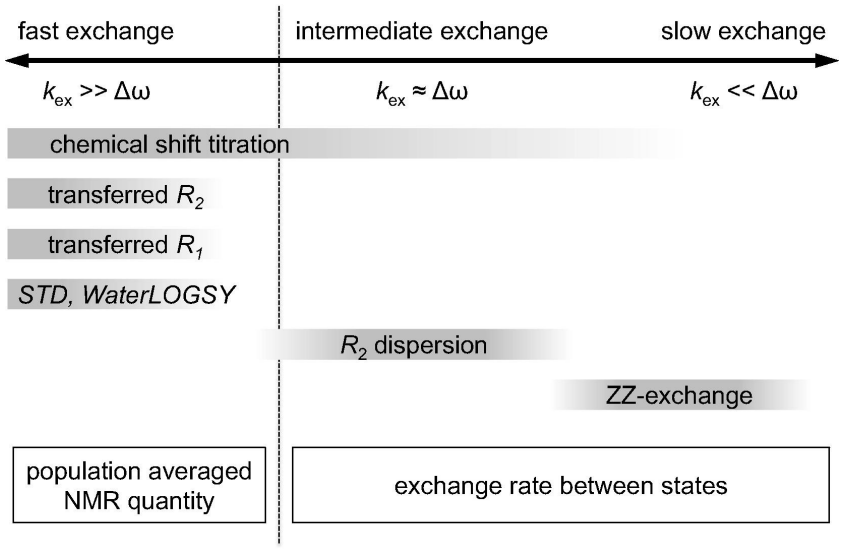

Figure 2.15: NMR methods for analysis of protein-ligand interactions with respect to the chemical shift timescales. The exchange regimes are defined by the ratio of the rate, k_{ex}, and chemical shift difference, $\Delta\omega$, between the free and bound states. Figure reprinted from Furukawa et al.[50]. Copyright 2016, with permission from Elsevier.

Keeping all this in mind it is easy to see how the full power of NMR can be best utilised when multiple experimental approaches are employed to reach an integrated outcome. In particular, FBDD gives a good example how those can be combined and, when complimented with other interrogation platform, lead to a highly effective outcome.

2.5 Probing protein - ligand interactions, alternative methods

So far, the focus of this review were methods in structural biology. However, in relation to the project aims, other techniques to study protein-ligand interaction need to be considered. Keeping with the classification proposed by Yakimchuk[181], the following categories are identified:

2.5.1 Labelled ligand-binding assays

Common methods exploit principles of fluorescence, radioactivity and bioluminescence. In particular, Förster Resonance Energy Transfer (FRET) is a technique highly sensitive to intermolecular distances, although susceptible to fluorescence interference. This method employs the use of two interacting fluorophores, where change in emitted

wavelength is observed when both are in close proximity (< 100 Å)[93]. For this reason, FRET is suitable to detect protein-protein interactions and conformation changes of single proteins. In particular, it was proven useful to study behaviour of membrane proteins[64] in real time. Radioligand binding assays are the method-of-choice for membrane-bound receptors, especially useful for high-throughput studies to determine the binding affinity. Three main binding experiments are: saturation assay, competitive assay and kinetic assay[66]. Primary advantage of this method is simple experimental protocol and ability to determine different binding aspects based on the choice of assay. Nevertheless, concerns arise due to handling of radioactive material. Bioluminescence based platforms, e.g. NanoLuc (Promega, US), utilise the well-known function of the luciferase enzyme. Amongst others, the principles are used for FRET-like Bioluminescence Resonance Energy Transfer (BRET) assays and complementation reporters, where the luciferase protein is separated into two stable components and attached to potential interaction partners[34].

2.5.2 Label-free assays

Multiple methods explore the optical aspect of molecular interactions. Surface plasmon resonance (SPR)[61] and plasmon-waveguide resonance (PWR)[129] measure the changes of the refractive index of the analysed solution at a gold (SPR) or quartz (PWR) surface with immobilised target in response to ligand binding. Advantages of those methods include low sample requirement, application for soluble and membrane-bound proteins and ability to determine binding kinetics in real-time. PWR in particular is highly sensitive to conformation changes with ability to distinguish between full agonists, partial agonists and antagonists[3]. Main complications arise from the need to immobilise the protein target, which may cause interfere with the binding profile. By contrast, mass spectrometry (MS) is a high sensitivity method, where the mass of protein and protein-ligand complex is identified. Currently available saturation experiments allow to characterise even very low affinity ligands, as well as their binding kinetics[55]. Affinity selection MS in turn is commonly employed for screening wide libraries of target compounds and filtering false positive interactions[67]. High accuracy, low cost and suitability for high throughput analysis makes this method a good alternative for radioligand based assays.

2.5.3 Thermodynamic assays

In general, the following techniques can be well applied in almost any laboratory and provide a good platform for high throughput ligand screening. Thermal denaturation assays (TDA) exploit the increase in thermal stability of proteins upon ligand binding. In a usual setup, fluorescence- or aggregation-based approach is assumed to

detect changes in thermal denaturation patterns of proteins in the presence and absence of ligands[149]. For some complexes multiple denaturation transitions may be observed, providing additional information on the interaction profile. Isothermal titration calorimetry (ITC) allows to quantify the heat change observed in a binding event. As such, it is well suited to distinguish between entropic and enthalpic aspects of protein binding[161]. Although widely used, this method is currently limited to high affinity, and single binding site protein-ligand interactions.

2.5.4 Whole cell assays

Methods include Surface acoustic wave (SAW) and resonant-waveguide grating (RWG) biosensors, which are adaptations of SPR and PWR techniques described earlier[4,82]. Both methods detect binding on a surface with immobilised ligand. A change in the amplitude of applied electromagnetic (RWG) or acoustic wave (SAW) is recorded as a measure of molecular mass. Here, membrane receptors are under study allowing for cell attachment. More complex implications of ligand binding can be investigated through combination with other methods, e.g. microscope imaging.

2.5.5 Structure-based assays

Previously discussed XrC and NMR are amongst the most widely used ligand binding methods overall. The unique advantage here is the potential to reach atomic resolution and fully identify the binding surfaces. Specific limitations for both methods render them best suited for different interaction regimes. The necessity to co-crystallise protein-ligand complexes is a major obstacle in XrC, therefore high affinity complexes are preferable. NMR in turn is limited by molecular size but applicable to study reversible interactions of soluble proteins.

Here it is important to point out neither of the available methods are mutually exclusive. Ongoing research is result- and cost-driven, hence the persistent need for innovation and optimisation. In an ideal scenario a single platform would have capacity to provide full binding characterisation for any target. This at present remains unattainable and for most purposes several methods need to be exhausted.

2.6 Microfluidics and its applicability to biomolecular sciences and NMR

2.6.1 Historical context

The object of microfluidics is the science and technology involved in manipulation of small (below 1 ml) volumes of liquid. Whitesides[171] recognises four origins of this field: **a**) molecular analysis, **b**) biodefence, **c**) molecular biology and **d**) microelectronics. Widely regarded as the first platform that demonstrated the power of miniaturisation, Terry et al.[160] presented a gas chromatograph fabricated on a silicon wafer, which offered nearly three orders of magnitude reduction to the overall size of the experimental apparatus in comparison to the conventional setup, without detriment to the device's performance. Following in their footsteps, Manz et al.[98] were the first to introduce the microchip technology to chemical analysis and present the concept of a miniaturised total analysis system (μTAS), i.e. a singular microfluidic device designed to carry out all steps involved in sample analysis, rather than just limiting the sample use. Nowadays this is also referred to as Lab-on-a-Chip (LoC).

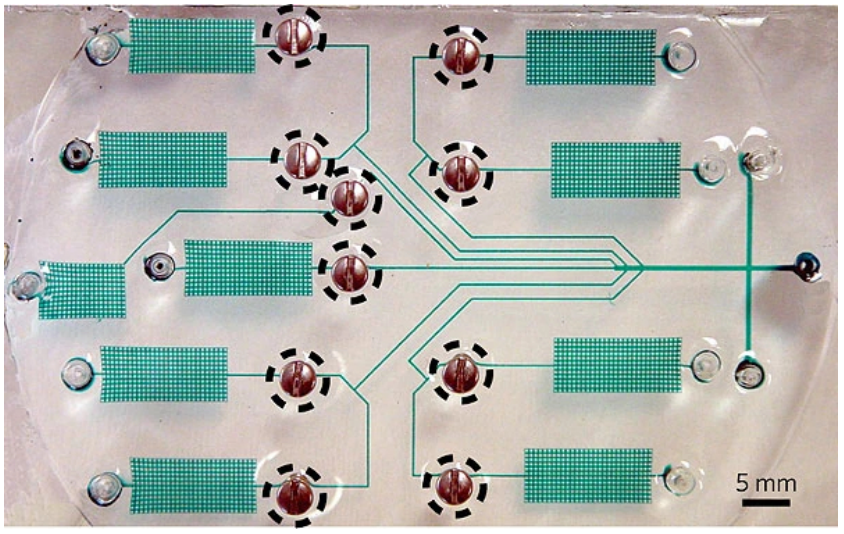

Figure 2.16: Microfluidic device used for sandwich immunoassays as described by Weibel et al.[169]. The device is fabricated in PDMS and incorporates manually operated screw valves (in dashed circles) for controlling the flow of fluids in microfluidic channels. The channels and reagent reservoirs are filled with green dye. Figure reprinted from Whitesides[171]. Copyright 2006, with permission from Springer Nature.

Integration of multiple functionalities, e.g. sorting, mixing, pumping, analysis, offered significant improvements in terms of simplification of experimental procedures, reduced consumption of reagents, and the potential to run multiple experiments in parallel, yet required precise fabrication techniques and new materials. Much was made

possible thanks to soft lithography and polymers such as PDMS, silicon, and other materials, e.g. glass. In particular, the importance of PDMS to microfluidics cannot be overstated. Primarily it is an inexpensive, easily moulded soft elastomer which allows for rapid prototyping. Due to its elastic character it has become possible to fabricate structures in PDMS that could not function in a rigid material. Classic examples are pneumatic valves, such as those developed by Unger et al.[164] or Grover et al.[56]. The former design includes a central liquid line and multiple perpendicular gas channels above it, pressure supplied to the gas channels forces them to expand and block the fluid path beneath, and when actuated in a sequence the valves can create a net flow of the liquid. Further advantages of PDMS include transparency, meaning it can be coupled with optical detection methods, gas permeability, compatibility with biological samples to quote a few, which overall makes it the first choice material for many microfluidic devices. Exemplary microfluidic device fabricated in PDMS and incorporating non-trivial flow control elements necessary for immunoassay functionality is shown in fig. 2.16.

2.6.2 Characterisitcs and challenges

Miniaturisation in microfluidic systems affects not only volumes but also the behaviour of manipulated liquids, which falls under an entirely different regime than that observed on the macroscopic scale. One of the principal characteristics in fluid dynamics is the ratio of inertial to viscous forces, represented by a dimensionless parameter known as the Reynolds number (Re):

$$Re = \frac{uL}{v} \tag{2.29}$$

where u is the flow velocity, L is the characteristic length scale and v is the kinematic viscosity. At the macroscopic scale liquids' Reynolds number are usually very large and lead to turbulence, i.e. chaotic changes in the pressure and flow velocity. In microfluidics Re is very low, i.e. the viscous forces dominate and the inertial effects become negligible, therefore the liquid flow becomes essentially laminar. What this means is that the motion of the fluid particles is very orderly, resembling layers of solids moving in parallel, as depicted in fig. 2.17. Another measure is the Péclet number (Pe) which relates the convection and diffusion occurring in the sample:

$$Pe = \frac{uL\,\rho\,c_p}{k} \tag{2.30}$$

where k is the thermal conductivity and c_p is the specific heat capacity. Again, in microfluidics this ratio is skewed almost entirely towards diffusion. As result of those two characteristics mixing in microfluidic systems is a notorious challenge. For two fluid streams that meet in a common microchannel and flow perfectly in parallel, without

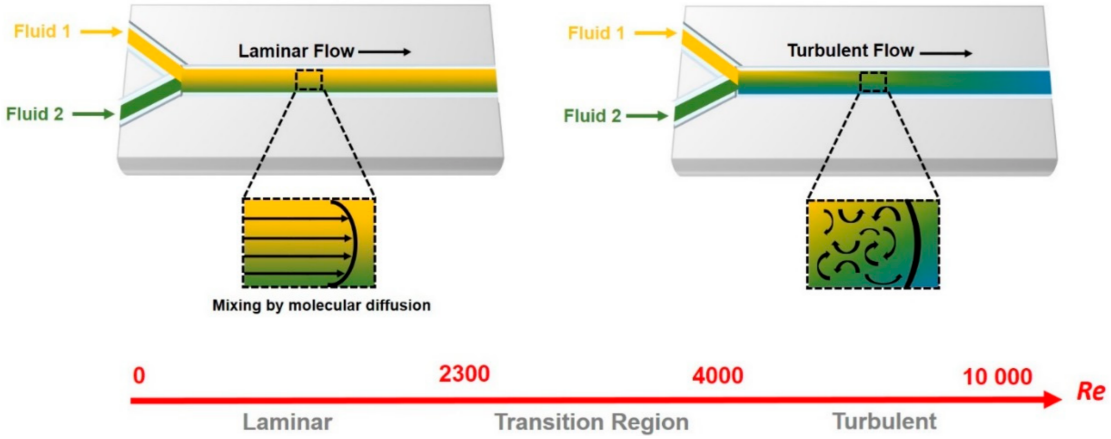

Figure 2.17: Schematic representation of the laminar and turbulent flow regimes. Figure reprinted from Saliba et al.[139] with permission from the author and under the terms of a Creative Commons (CC BY 4.0) license.

any eddies or turbulence, the mixing is basically determined by their contact surface, as shown in fig. 2.17. Taking into account the very small channel diameters of microfluidic devices, such process can take hours. Multiple strategies were assumed to tackle this problem. In general, the solutions can be classified as either active or passive micromixers. Passive approach can be summarised as any adptations to the channels' geometry that give the reagents maximum contact surface. This can be achieved by incorporation of structures such as obstacles, serpentines, convergence-divergence channels, etc. In turn, active micromixers act by applying external forces to the sample, such as acoustic waves, pressure perturbations, magnetic fields, and others. Excellent review of commonly employed micromixers in microfluidics was recently published by Cai et al.[18].

2.6.3 The applications perspective

Modern day microfluidic devices are designed to fit the LoC functionality. Such systems are expected to contain a range of generic components with the ability to: **a**) introduce the reagents, **b**) move the sample liquid, **c**) effectively mix and/or separate mixture components and **d**) carry out detection via fluorescence spectroscopy[65], MS[17], UV-vis spectroscopy[91], plasmonics[185], immunohistochemistry[109], or other methods. NMR, despite its wide range of applications, for years has remained outside of the focus of microfluidics due to its inherent low sensitivity. Much has changed at the break of the 21st century with the introduction of miniaturised detectors[178] that brought improvement in terms of resolution and mass limit of detection. Over the years, many detector designs were developed, some operating on very low volumes and with excellent performance parameters (detailed summary in table B.1 in the appendix). Nonetheless, most micro-NMR (μNMR) platforms fall outside of the

μTAS/LoC category. The incorporation of low-volume detectors[108,132,134] and one-way flow systems[33,63,69,77] has become more widespread over the last two decades and has led to the emergence of so-called hyphenated systems. Flagship representatives of these are platforms that combine liquid chromatography (LC) for sample preparation with NMR detection (LC-NMR)[63,89,90]. The major limitation associated with them is the inability of the LC technology to operate at high magnetic fields, and the prevailing approach is to place all flow manipulation components outside of the spectrometer. However, even if the LC and NMR are connected via a low inner-diameter (ID) capillary, the system still operates with notable dead volumes. Other strategies, like coupling NMR with digital microfluidics[84,156] have proven more effective. Specifically, Swyer *et al.*[156] have presented a system operating at high magnetic fields and capable of detailed control over multiple sample droplets. Nonetheless, in the context of LoC functionality, even this high-precision device has limitations in terms of serial sample manipulation, that each time requires manual involvement, i.e. removal of the NMR probe and loading of the new sample. Furthermore, the specifics of NMR dictate that after the probe is reintroduced into the magnet any inhomogeneities in the magnetic field need to be corrected, i.e. 'shimmed', in order to reach good signal resolution. A task that can be time consuming even for a skilled operator.

2.6.4 Microfluidic protein NMR

The introduction of microfluidics to protein NMR is not new. Building on the success of the first miniaturised detectors, a new range of triple-resonance probes was developed[87,144] with applicability for protein studies. Those early contributions have led to the development of commercially available CapNMR (Protasis, US) and TCI 1.7 mm MicroCryoProbe^{TM} (Bruker, US) micro-probes. Both offer significant improvement in terms of sample requirement ($\sim$ 15 μl) however in the microfluidics aspect neither goes beyond the applications discussed so far. Peti *et al*[125] were one of the first to demonstrate the suitability of the micro-probes for protein NMR and reach complete sidechain assignment based on the μMNR data. In some aspects, they have proven the CapNMR's ability to outperform the conventional 5 mm probes. In their later work[126] the group proposed a unified "pipeline" approach extending all the way from protein micro-expression to characterisation by μNMR. Later, this approach was validated by Zhang *et al*[189] and Rossi *et al*[134]. Both have demonstrated μNMR to be an effective and a cost efficient strategy for large scale optimisation of buffer conditions or protein constructs for structure determination in the later stages.

Chapter 3

NMR characterisation of protein-ligand interactions

This chapter presents the results obtained by the author, using a conventional state-of-the-art NMR equipment, for the study of the hFynSH3 protein and its interaction with a short peptide ligand, p85$\alpha_{\text{P91-T104}}$. Initially, the relevant literature on this molecular model system is summarised, followed by the detailed description of the analysis strategies based on the gathered multidimensional NMR data necessary for structural and thermodynamic characterisation. The aim is to demonstrate the analytical power of NMR as a method for analysis of biomolecular systems, using the assumed molecular model and show the present-day capabilities of commercial NMR hardware. The work presented here is continuing with aim to comprehensively describe the hFynSH3 - p85$\alpha_{\text{P91-T104}}$ system and is expected to be compiled into a relevant publication in the coming months.

3.1 Background

3.1.1 The hFynSH3 - p85$\alpha_{\text{P91-T104}}$ molecular model system

The Src homology 3 (SH3) domain of the human protein Fyn (hFynSH3) was the primary object of study for this project. Fyn is a membrane-associated tyrosine kinase from the Src family, involved in multiple cell functions such as T-cell signalling and neuronal development[71,136]. All Src family members are built by six distinct domains, of which the SH2 and SH3 are necessary for binding to other proteins elements of the signal transduction pathway[36,103,131,152]. SH3 domains are approximately 60

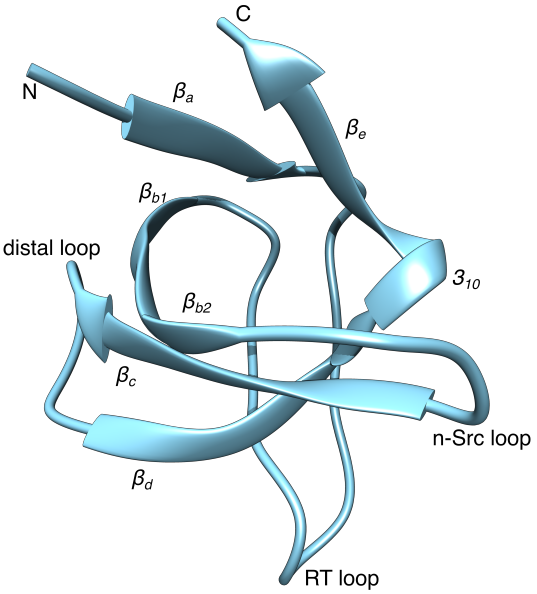

Figure 3.1: Ribbon representation of the hFynSH3 backbone with labelled secondary structure elements. Image produced using UCSF Chimera, based on a previously elucidated structure[114,131], PDB entry: 1NYF.

amino acid (AA) modules commonly recognised to bind proline-rich polypeptide fragments[29,43,81,101,103,116,187]. The canonical recognition site holds the common PxxP motif, where x signifies any residue, arranged in a left-handed polyproline II (PPII) helix[43,103,116]. Recognition of the PxxP motif is carried out by highly conserved Asn, Tyr, Trp and Pro residues between different members of the Src family[44,81]. The flanking residues, specifically the position of a basic residue, most commonly arginine, and the orientation of the ligand is also relevant, hence the two main classes of polypeptide ligands are identified: class I contain the consensus sequence RxLPPxP, whereas for class II the consensus sequence is xPPLPxR[43,81,103], and each orient themselves in an opposite direction with respect to the protein. In some circumstances non-canonical binding was also reported[44,68,70,76,111], however the prevailing presence of prolines, the only naturally occurring N-substituted residues, remains critical for the composition of the ligand. Indeed, Nguyen et al.[117] have shown that proline replacement for synthetic N-substituted residues in a series of polypeptide ligands is not only non-detrimental, but can actually improve the affinity towards the SH3 domain[117,118].

On their own, most SH3 domains are soluble proteins below 10 kDa and show a conserved structure, based on two antiparallel β-sheets and several loop regions[81]. The two antiparallel β-sheets are built by six identified β-strands, while three loop regions and a single 3_{10} helix complete the overall structure, as presented in fig. 3.1. Two distinct structures, FynSH3-1 and FynSH3-2, were first resolved by X-ray crystallography[120], both showing a well conserved β-sheet core structure, however only FynSH3-1 was recognised to be significantly populated in solution[114]. Critically, the binding

surface on hFynSH3 is classically located between the RT (Leu^{90}-Glu^{107}) and n-Src loop (Ser^{114}-Asp^{118}), where at least three hydrophobic grooves can be recognised and include the conserved Asn, Tyr and Trp residues[43,73,88,131,152]. The first two grooves are involved in the recognition of the two prolines from the PxxP motif, while the third/-fourth binds the positively charged arginine residue[43,81].

This work builds on the previously characterised binding of hFynSH3 with a class I ligand, corresponding to residues 91-104 of the p85α regulatory subunit of the PI3-kinase, p85$\alpha_{P91\text{-}T104}$: PPRPLPVAPGSSKT[114,131]. It was shown that the SH3 domain of Fyn is involved in the recruitment of the p85α subunit of PI3-kinase through its proline-rich region[71] to trigger the proliferation of antigen-activated T-cells, mediated by the T-cell derived growth factor, Interleukin 2[72]. Biophysical studies have resolved the hFynSH3 structure in complex with p85$\alpha_{P91\text{-}T104}$[114] and comprehensively characterised the binding towards the greater PI3-kinase[131].

3.2 hFynSH3 protein chemical shift assignment

3.2.1 Backbone amide groups - the protein fingerprint

3.2.1.1 Description

Multidimensional heteronuclear NMR experiments are well established for protein study[20,159,179,180]. One of the primary applications takes into account the fact that all proteins contain repeated amide links at every residue of the amino acid chain. The amide links are made 'accessible' to NMR by ^{15}N-isotope labelling of the protein construct[106], which can be carried out competently and inexpensively in most biochemistry labs. Exploiting the single bond *J*-couplings between the ^{1}H and ^{15}N atoms, as explained in section 2.3.7, a two dimensional ^{1}H-^{15}N HSQC/HMQC[20] spectrum is recorded, where individual amide groups are dispersed onto separate ^{1}H and ^{15}N chemical shift axes. The highlight of this experiment is such that it provides a single resonance signal for each NH group of the protein backbone, with the exception of prolines. Each NH resonance can be further correlated to other atoms within the protein structure. Peak distribution on the ^{1}H-^{15}N plane gives immediate information about the folding character of the sample and to a skilled experimenter provide clues for further investigations. Apart from the backbone signals, individual resonances can also be observed for the sidechain amide groups, as in Trp, Asn, Gln, Lys and Arg residues. These resonances are dispersed into the characteristic regions of the spectrum and can be easily distinguished from the backbone resonances. Due to the above, the ^{1}H-^{15}N HSQC spectrum is often referred to as the protein 'fingerprint' and provides the anchor for the modern multidimensional characterisation of proteins by NMR.

Figure 3.2 shows the full ^{1}H-^{15}N HSQC spectrum of the hFynSH3 construct, including the assignments of individual amide signals. Well dispersed backbone peaks allow to conclude that the protein remains in its native state in the experimental conditions, while sidechain specific signals can be seen in the top right and bottom left corners of the spectrum, for Asn and Gln or Trp residues, respectively. Similar spectra were obtained at regular intervals between other NMR experiments on hFynSH3 to verify sample stability.

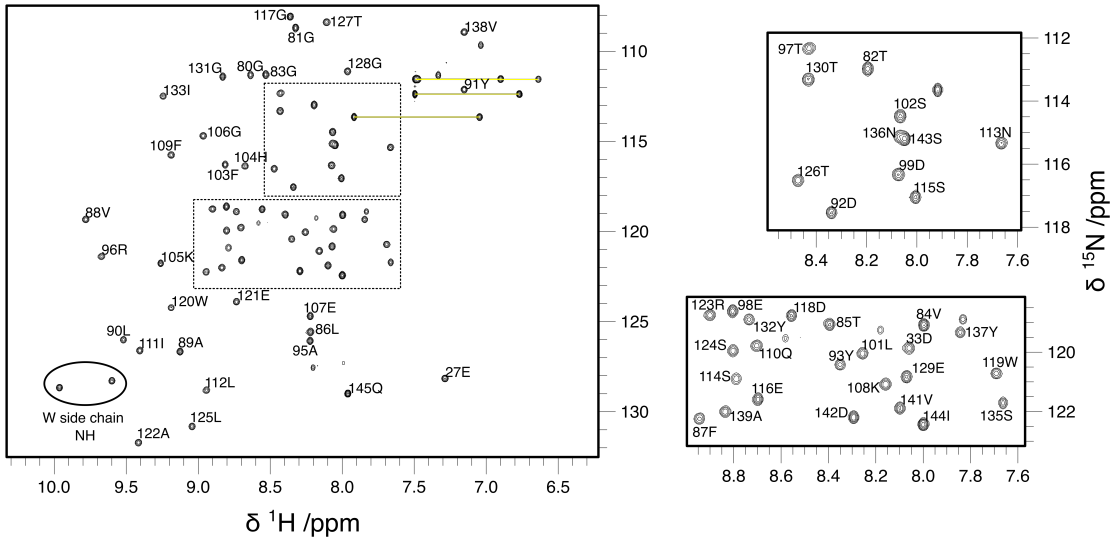

Figure 3.2: ^{1}H-^{15}N-HSQC spectrum of the hFynSH3. Assigned are 63 backbone amide peaks from the 80 - 145 AA sequence of hFynSH3. NH_2 groups at Asn and Gln sidechains can be recognised by two ^{1}H peaks at the same ^{15}N resonance (connected with yellow lines), each. Trp indoles produce a single peak near the lower left edge of the spectrum (circled). Sample conditions: 0.65 mM hFynSH3 in H_2O analysis buffer and 5% D_2O (300 μl sample in SHIGEMI tube); spectrum recorded at 16.45 T with the Prodigy TCI CryoProbe (Bruker, US) at room temperature.

3.2.1.2 Approach

The current strategy for the assignment of the ^{1}H-^{15}N HSQC spectra is based on triple resonance experiments, namely the HNCACB[59] and CBCA(CO)NH[58]. These two experiments correlate the resonances of the alpha-, Cα, and beta-carbons, Cβ, to the backbone amide groups, where the resonance of the carbon nuclei is recorded, building a direct link to the amide resonances in the ^{1}H-^{15}N HSQC spectrum. The initial magnetisation is generated on the ^{1}Hα and ^{1}Hβ protons and transferred through-bond via INEPT to the Cα and Cβ carbons, respectively. Subsequent magnetisation transfer is carried towards Cα before it reaches the amide proton for detection. For each backbone amide, where the resonance is detected, magnetisation from the same (i) and the preceding (i-1) residue is collected, therefore four ^{13}C signals are recorded at each NH resonance, as displayed in fig. 3.3 B. The elegant feature of the HNCACB spectrum is

that, due to one more magnetisation transfer step, Cβ signals are easily distinguishable from Cα signals as they appear with opposite phase in the spectrum.

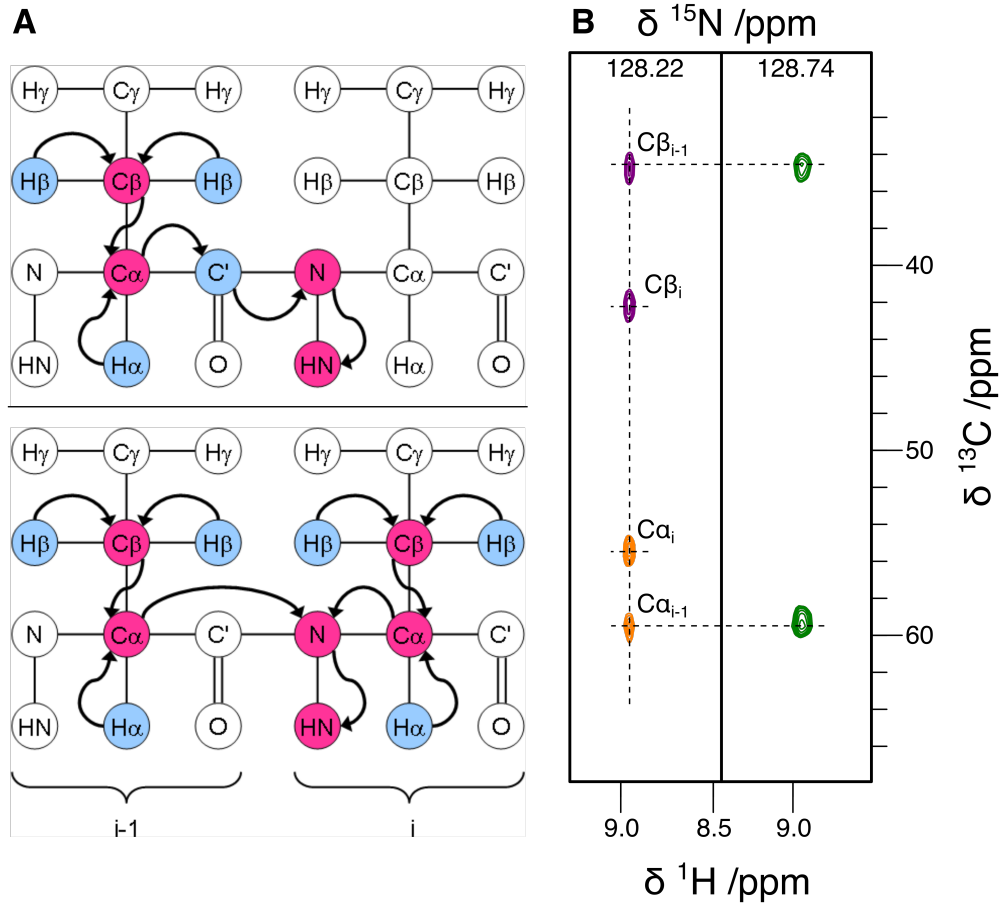

Figure 3.3: Diagram representation (A) of the magnetisation transfer carried out during the CBCA(CO)NH (top) and HNCACB (bottom) experiments. The colouring scheme differentiates the nuclei where chemical shift evolution is carried out (red) from those involved only in magnetisation transfer (blue), therefore the resulting spectra (B) provide resonances for ^{13}Cα, ^{13}Cβ carbons, and both the ^{15}N and ^{1}H of the backbone amide groups but not ^{1}Hα or ^{1}Hβ. In the HNCACB (left) spectrum, two pairs of Cα and Cβ signals, from the same (i) and neighbouring (i-1) residue, are recorded at the same (i) NH resonance. Conversely, in the CBCA(CO)NH (right) spectrum only the Cα and Cβ signals from the neighbouring (i-1) residue are recorded at the equivalent NH resonance, therefore easing the assignment. Diagram representations were reproduced from 'Protein NMR: A practical guide' (https://www.protein-nmr.org.uk/) with permission from the author.

In order to correctly assign the observed Cα and Cβ resonances, the HNCACB is always compared with the CBCA(CO)NH spectrum. In this experiment the magnetisation is generated the same way as for HNCACB, however the final coherence transfer is carried out from the sidechain Cα selectively via the carbonyl group, before detection at each (i) amide resonance. In the resulting spectrum only two same-phase signals are visible, representing the Cα and Cβ resonances of the preceding (i-1) residue. Simply comparing the two spectra, as presented in fig. 3.3 B, allows to blindly assign neighbouring AA residues and connect those to the corresponding NH signals in the ^{1}H-^{15}N

HSQC spectrum. After individual AA pairs are identified, longer chains of potential assignment stretches are created. Specific residue identities are determined by comparing the observed Cα and Cβ chemical shifts with the reference database (RefDB) available via the BioMagRes Bank (http://www.bmrb.wisc.edu). Stretches of matched Cα and Cβ pairs are screened against the known protein sequence in order to find full assignment and relied back to the amide resonances in the ^{1}H-^{15}N HSQC spectrum. Figure 3.4 gives an example of the Cα, Cβ assignment stretch of the Thr^{97}-Glu^{107} residues, identified on the hFynSH3 protein as result of the discussed strategy. Based on the above, backbone amide resonances for AA residues 80-145 of hFynSH3 were assigned, excluding the non-detectable Pro^{134} and Pro^{140}. This accounts for 81% of all AA residues in the protein construct and 97% within the core hFynSH3 sequence. Difficulty to assign the N-term residues is due to likely unstructured and flexible character of this region. Likewise, Pro^{70} is expected to be undergoing *cis* − *trans* isomerisation which can cause additional line-broadening of the neighbouring residue signals.

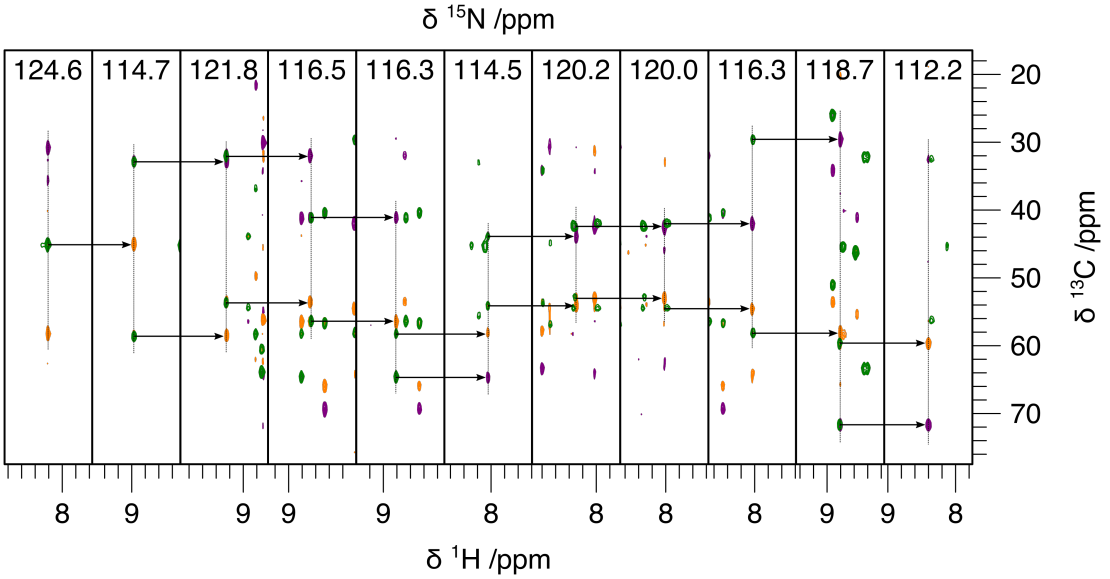

Figure 3.4: Superimposed HNCACB and CBCA(CO)NH spectra showing the assignment link for Thr^{97}-Glu^{107} (right to left) of hFynSH3. A stretch of neighbouring residues is first identified based on the matching Cα and Cβ present in both spectra, and subsequently mapped onto known protein sequence. This strategy was utilised to identify the backbone signals in the ^{1}H/^{15}N-HSQC spectra of free hFynSH3. Sample conditions: 0.65 mM hFynSH3 in H_2O analysis buffer and 5% D_2O (300 μl sample in SHIGEMI tube); spectrum recorded at 16.45 T with the Prodigy TCI CryoProbe (Bruker, US) at room temperature.

3.2.2 Sidechain and surface profile

The assignment strategy discussed so far was extended to identify atoms in the AA sidechains, which further determine the protein's chemical functionality. CC(CO)NH[60] and H(CCO)NH[60,112] are triple resonance experiments that correlate the sidechain

aliphatic carbons and protons, respectively, to the preceding (i-1) backbone amide group assigned in the ^{1}H-^{15}N HSQC spectrum. Both experiments can be considered as adaptations of the CBCA(CO)NH experiment discussed earlier. The magnetisation transfer pathway is very similar, however the initial magnetisation is generated on all aliphatic protons, before it is transferred via the attached ^{13}C nuclei and carbonyl carbon towards the backbone amide for detection. Evolution of the chemical shift is carried out either on the aliphatic protons, for the H(CCO)NH, or carbons, for the CC(CO)NH, therefore those are resolved and linked back to the assigned NH signals in the ^{1}H-^{15}N HSQC spectrum. CBCA(CO)NH and CC(CO)NH spectra can be directly overlaid to confirm the position of the Cα and Cβ peaks for each AA residue, while higher order carbon resonances, and protons resolved in the H(CCO)NH experiment, are identified by matching them to the chemical shifts from the reference database. Exemplary H(CCO)NH and CC(CO)NH spectra, highlighting the chemical shifts of the sidechain aliphatic protons and carbons of Val^{138} are presented in fig. 3.5 A and B, respectively.

Based on the above method, 96% of the aliphatic carbon and proton signals from the identified Gly^{80} - Gln^{145} hFynSH3 sequence were assigned. The corresponding proton and carbon chemical shifts were projected onto the two-dimensional ^{1}H-^{13}C HMQC spectrum (fig. 3.5 C) analogous to the fingerprint ^{1}H-^{15}N HSQC discussed earlier. At first sight this spectrum appears very crowded, however it offers significant advantages over many triple-resonance experiments. Less complicated pulse sequence results in notable sensitivity gain and most signals originating from the CH, CH_2, and CH_3 groups on the protein are well resolved and separated into characteristic regions. Easy access to the methyl groups has become specifically useful in protein NMR. In general, they provide strong signals and are universally distributed throughout the protein structure, therefore become excellent probes for dynamic processes such as protein-protein interactions. Furthermore, due to favourable relaxation properties they also remain accessible even for large proteins and supra-molecular complexes[128,146,172].

Final steps towards the assignment of the sidechain signals for hFynSH3 were taken by acquisition of spectra able to resolve the signals of the aromatic groups. An effective pulse sequence was developed by Yamazaki et al.[184], where the magnetisation transfer is carried out exclusively via the sequential J-couplings between the Hβ/Cβ and Hδ/Cδ or Hϵ/Cϵ[184]. Resulting 2D spectra resolve specifically the chemical shifts of the Hδ and Hϵ protons on the aromatic sidechains, which report at the Cβ chemical shift of the same residue therefore easing their assignment. Additional advantage of this approach is the notable sensitivity gain as the initial magnetisation is generated on two Hβ protons before transfer towards the aromatic sidechain. After the identification of the individual Hδ and Hϵ resonances, the corresponding Cδ and Cϵ chemical shifts are identified from the full ^{1}H-^{13}C HSQC/HMQC spectrum.

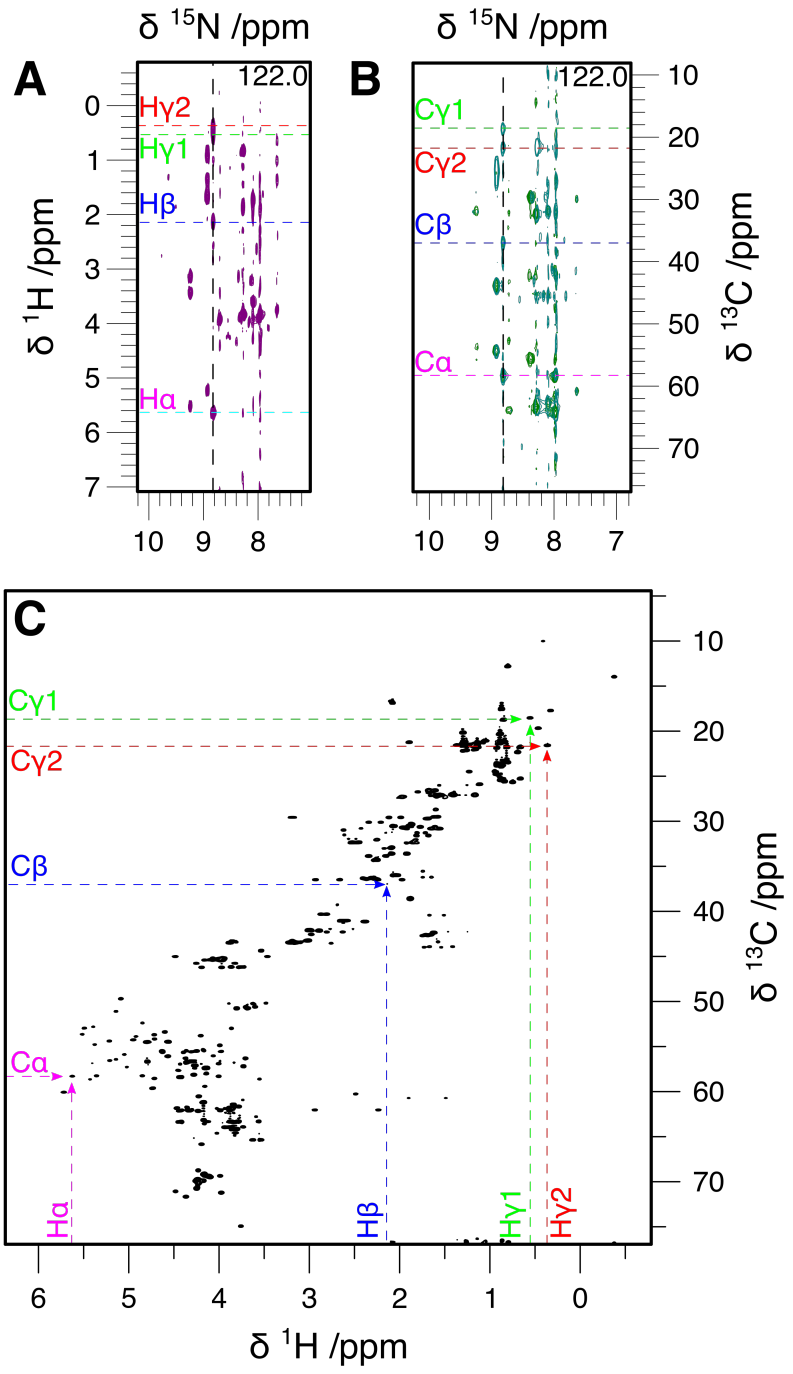

Figure 3.5: Demonstration of the sidechain assignment carried out for hFynSH3. Anchored to the NH resonance of Ala^{139}, Val^{138} sidechain (A) proton and (B) carbon peaks are identified in the CC(CO)NH and H(CCO)NH spectra, respectively. Such assigned resonances are then projected (C) onto the full ^{1}H-^{13}C-HSQC spectrum where corresponding cross-peaks can be identified. Sample conditions: 0.3 mM hFynSH3 in H_2O analysis buffer and 5% D_2O (300 μl sample in SHIGEMI tube); spectrum recorded at 16.45 T with the Prodigy TCI CryoProbe (Bruker, US) at room temperature.

3.2.3 The hFynSH3 - p85$\alpha_{\text{P91-T104}}$ complex

Assignment of the protein signals was carried out for both the free-form hFynSH3 and the hFynSH3 - p85$\alpha_{\text{P91-T104}}$ complex, at over 20 times molar excess of the ligand. The strategy laid out in section 3.2, based on acquisition of the ^{1}H-^{15}N and

^{1}H-^{13}C HSQC/HMQC, CBCA(CO)NH, HNCACB, CC(CO)NH, H(CCO)NH spectra was followed for the hFynSH3 - p85$\alpha_{\text{P91-T104}}$ complex, allowing to identify the maximum change in the chemical shifts, $\Delta\delta_{max}$, of individual signals induced by the ligand. Those can be mapped onto the known protein structure, where immediately highly-responsive atoms can be identified, as presented in fig. 3.6. Individual signals, that perturb above the cut-off threshold (σ_c) are listed in tables A.2 and A.3 in the appendix. Atomic resolution provided by this dataset is unique among other biophysical techniques, yet the analysis is far from trivial. First, one needs to consider that the changes in chemical environment can have diversified effect on the chemical shifts of different nuclei. ^{1}HN and ^{15}N shifts are especially affected by hydrogen bonding and ring currents, while they remain relatively insensitive to hydrophobic interactions, Cα and Cβ on the other hand are sensitive almost exclusively to conformation changes[145,155,173]. As a result, no one proven method is established when analysing individual shift contributions towards a multidimensional data set, such as most widely used ^{1}H-^{15}N HSQC. Commonly, a weighting factor, α, is applied to scale the contribution of the heteroatom, as discussed further, varying anywhere between 0.1 - 0.45[2,24,62], while also specific values can be designated to individual AA residues, e.g. glycines[165,174,176]. Further questions can be posed for the appropriate choice of the cut-off value. The most elegant method was proposed by Schumann et al.[145], where first the standard deviation, σ, for all $\Delta\delta_{max}$ values is calculated. Subsequently values above 3σ are rejected and the standard deviation is reevaluated. This process is repeated until no further shifts are excluded and the corrected standard deviation, σ_c, is accepted as the cut-off value. The $\Delta\delta_{max}$ distribution highlighted in fig. 3.6 provides good initial guess towards the structural characterisation of ligand binding. This information alone is not sufficient to distinguish between direct contacts and secondary changes induced by the ligand, however the common observation is that the largest changes occur in response to direct ligand binding[173].

3.2.3.1 Ligand binding surface on hFynSH3

The determined structure of the hFynSH3 - p85$\alpha_{\text{P91-T104}}$ complex allowed to identify the ligand binding surface on hFynSH3. It is classically located between the n-Src and the RT loops, including the conserved Asn^{136} and Tyr^{137} residues within the 3_{10} helix[114,131]. Individually resolved CSPs confirm this observation. In the ^{1}H-^{15}N HSQC spectrum, all of the pronounced signals are either located within the three structures, or in their direct vicinity. This picture is supported by the CSPs of the assigned sidechain CH, CH_2 and CH_3 groups, however those are scattered more evenly across the hFynSH3 structure, often close together within the protein core, indicating a common secondary response to ligand binding. Based on the assigned ^{1}H-^{15}N and ^{1}H-^{13}C HSQC/HMQC spectra and the *a priori* knowledge of the binding site, a good choice of signals can be made to best characterise the binding. Assignments extending towards

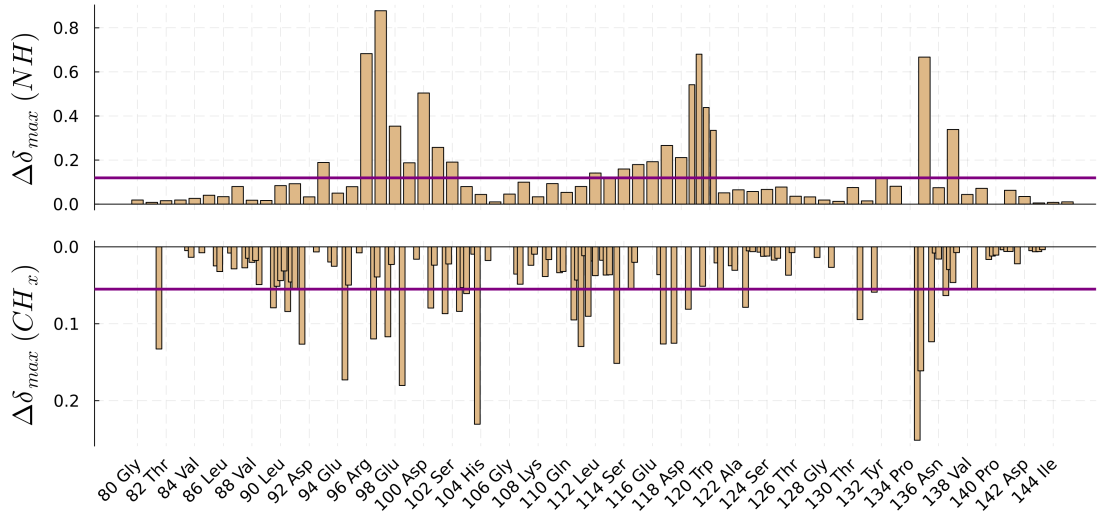

Figure 3.6: Distribution of the ligand-induced CSPs across the structure of hFynSH3. The histograms show the highest CSP values, $\Delta\delta_{max}$, for individual the amide signals (top) and sidechain methyl, methylene and methine groups (bottom). The horizontal lines are the σ_c cut-off value above which significant CSPs are qualified. For clarity, only the altering residues are labelled along the X axis.

the aromatic sidechains complete this picture. Out of the eleven aromatic residues in the hFynSH3 construct, the highest $\Delta\delta_{max}$ were identified for Tyr^{91} Hδ/Cδ, Tyr^{93} Hδ/Cδ and HϵCϵ, Phe^{103} Hϵ/Cϵ, and both tryptophan (119, 120) Hδ/Cδ resonances. Importance of Tyr^{91} and Tyr^{93} was elucidated previously and both are expected to accommodate a single proline residue from the PxxP motif of the ligand [43,131]. Likewise, the sidechain of Trp^{119} extends towards the surface of hFynSH3 and is involved in recognition of the critical arginine residue, Arg^{93}, of the p85$\alpha_{\text{P91-T104}}$ peptide.

From all identified CSPs in the ^{1}H-^{13}C and ^{1}H-^{15}N HSQC spectra, the signals that indisputably report direct contacts with the ligand are the Trp^{119} Hϵ/Nϵ and Asp^{118} Hβ/Cβ, spaced less than 2.6 Å away from Pro^{94} and Arg^{93} of the ligand. However, large number of CSPs distributed further away from the binding surface suggest that the mobility of hFynSH3 in response to the ligand is not only limited to the surface. Specifically, ligand binding is expected to induce notable aromatic ring reorientation and stabilisation to maximise the contacts with the ligand. Aromatic rings are associated with the delocalised π-electron clouds which are free to circulate parallel to the ring's plane. Such electron motions generate a magnetic field that has influence over the chemical shifts of the nuclei within the aromatic ring as well as those in it's vicinity [99]. For hFynSH3, this effect is considered responsible for the CSPs observed for Tyr^{91}, Tyr^{93}, Trp^{119} directly, and indirectly for Ala^{95} Hβ/Cβ, Thr^{97} Hγ/Cγ, Phe^{103} Hα/Cα and Hϵ/Cϵ. Curious case is observed for the most pronounced methyl CSPs, namely on Ile^{111}, Ile^{133} and Val^{138}, all of which remain buried closely together within the β-sheet core of hFynSH3. Such perturbations may be explained by the rearrangement of the neighbouring Trp^{120},

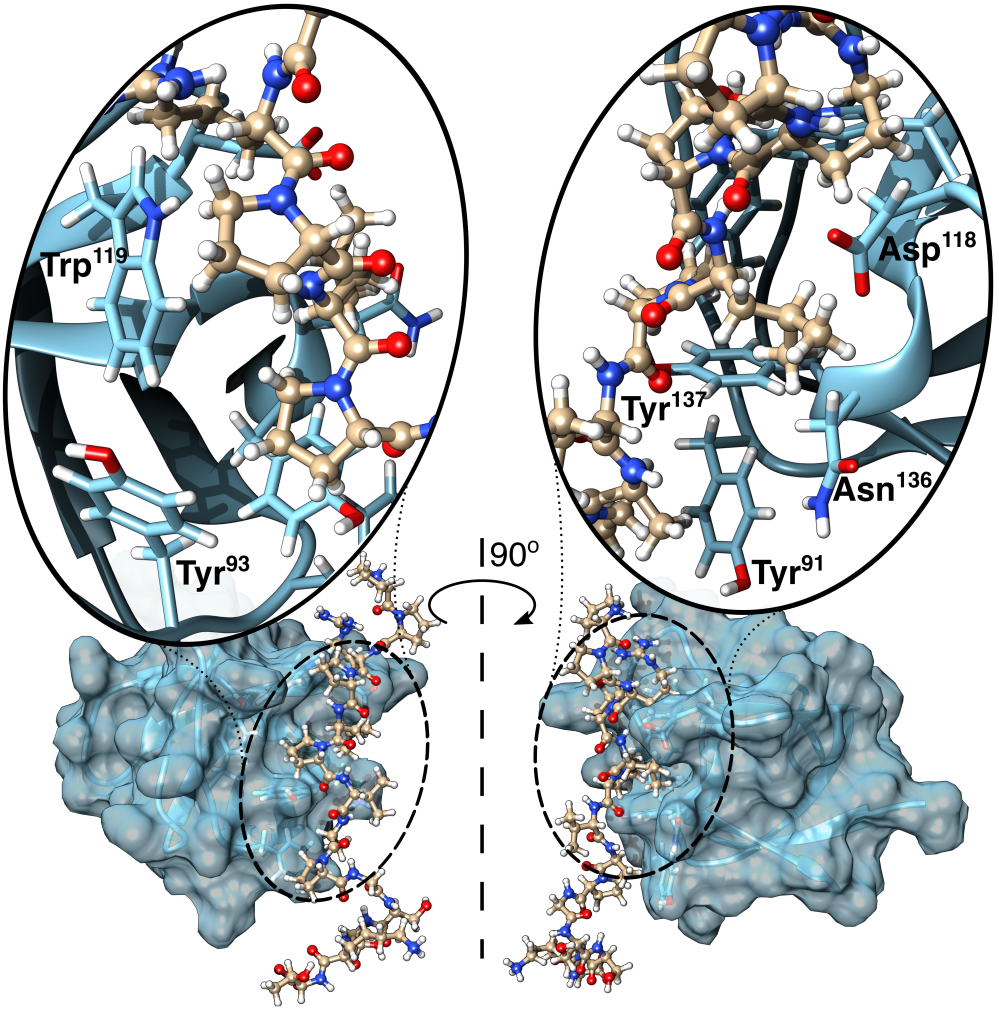

Figure 3.7: Orientation of the p85$\alpha_{\text{P91-T104}}$ ligand within the binding surface of hFynSH3. Molecular structure of hFynSH3 is represented in light blue colouring, including the half-transparent surface and backbone. The p85$\alpha_{\text{P91-T104}}$ ligand is shown in ball and stick representation using standard atom colour coding. The structure is shown twice, with 90° rotation with respect to the ligand. Expansions of the binding surface indicated by the dashed ovals are shown above the structures. Relevant residues that exhibit significant changes at their chemical shifts upon binding are highlighted in the blow outs. Figure generated using UCSF Chimera, based on the previously resolved structure[131]; PDB entry: 1AZG.

itself not involved in ligand binding but influenced by the mobility of the n-Src loop. The relevance of the Trp^{119} and Trp^{120} residues is critical, both displaying major mobility decrease when complexed with the ligand[131]. Based on all available information, a hypothesis is proposed that upon binding the system rigidifies in order to maximise the hydrophobic contacts between hFynSH3 and p85$\alpha_{\text{P91-T104}}$. Earlier studies have proven that the p85$\alpha_{\text{P91-T104}}$ peptide itself is natively unstructured and only assumes the PPII helix upon binding[131]. Distribution of the CSPs on hFynSH3 around the naturally flexible loop regions suggests those structures display a considerable motion in response to the ligand. All of these changes impose a notable entropic penalty on the system

which, in order to accommodate the observed binding, needs to be compensated by favourable enthalipc effects. Formation of hydrogen bonds and/or salt bridges, e.g. as the one proposed between Asp^{100} on hFynSH3 and Arg^{93} of p85$\alpha_{\text{P91-T104}}$ [187], would add significant enthalpic contributions, yet neither were experimentally confirmed [131]. The current understanding is that the stability of the hFynSH3 - p85$\alpha_{\text{P91-T104}}$ complex is determined mainly by hydrophobic contacts, which is reflected by a relatively low affinity [114,131].

Figure 3.7 demonstrates the orientation of the p85$\alpha_{\text{P91-T104}}$ peptide within the binding surface of hFynSH3. Identified are the residues on hFynSH3 that define the binding pocket. Tyr^{91} and Tyr^{93} each accommodate a proline residue from the PxxP motif on the ligand. Tyr^{137} is also involved in recognition of the second proline residue [43], and along with Hβ/Cβ of Asn^{136} it provides sizeable hydrophobic contacts to Leu^{95} of p85$\alpha_{\text{P91-T104}}$. Asp^{118} and Trp^{119} are the only two residues whose CSPs in the ^{1}H-^{13}C and ^{1}H-^{15}N HSQC/HMQC spectra report direct contacts to the ligand.

3.2.3.2 Secondary structure

The distribution of ligand-induced CSPs highlighted in fig. 3.6 includes multiple backbone amide as well as Cα and Cβ signals, and could suggest a conformation change is taking place within the hFynSH3 structure upon binding of p85$\alpha_{\text{P91-T104}}$. Such dynamics are common for many proteins, however conformation changes were not previously reported for this system. Fortunately, the wealth of information available within the heteronuclear NMR spectra is such that evaluation of conformation changes can be made based on the chemical shift information. So-called secondary shifts, $\Delta\delta_s$, show a direct correlation to the protein secondary structure and can be easily calculated as the difference between the observed (δ_{obs}) and random coil ($\delta_{r.c.}$) chemical shifts [13,78,147,175,176]:

$$\Delta\delta_s = \delta_{obs} - \delta_{r.c.} \tag{3.1}$$

Specifically, Cα atoms tend to demonstrate positive $\Delta\delta_s$ in α-helices, and negative in β-strands. The Cα secondary shifts distribution for hFynSH3 is presented in fig. 3.8, in blue the $\Delta\delta_s$ values for the free-form hFynSH3 are presented, paired with the corresponding secondary shifts of the hFynSH3 - p85$\alpha_{\text{P91-T104}}$ complex, in red. On top, the expected secondary structures are aligned with the protein AA sequence. Only minor differences can be observed between individual Cα secondary shifts, therefore a conclusion is drawn that no major-scale changes of the protein secondary structure are induced by the ligand binding. As such, these findings are well aligned with prior reports from Morton et al. [114] and Renzoni et al. [131].

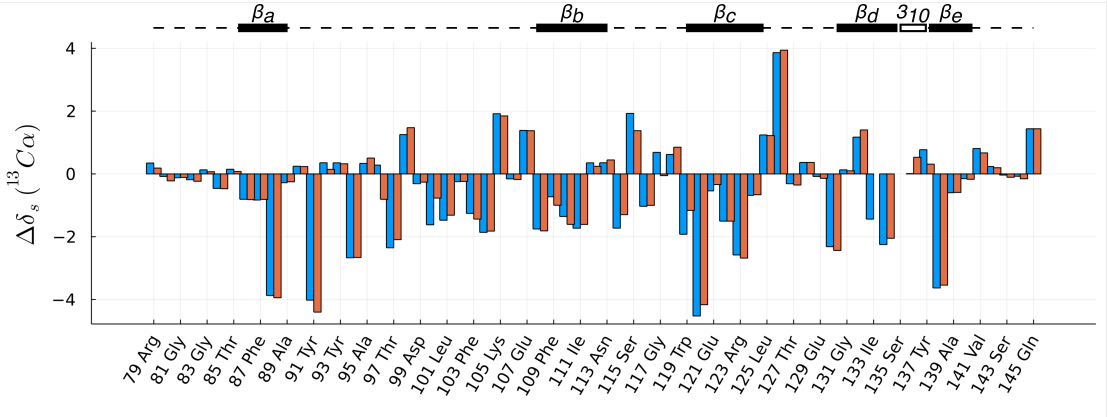

Figure 3.8: Secondary Cα shifts calculated for the free hFynSH3 (blue) and the hFynSH3 - p85$\alpha_{\text{P91-T104}}$ complex (red) structures based on the reported chemical shifts. On top, the position and identity of the recognised secondary structures is shown, β strands are represented in black while the single 3_{10} helix is shown in white.

3.3 hFynSH3 - p85$\alpha_{\text{P91-T104}}$ binding analysis

3.3.1 Approach

Having assigned the resonances of both the free-form hFynSH3 and the hFynSH3 - p85$\alpha_{\text{P91-T104}}$ complex, the interaction profile for this molecular system was completed by observation of the transient states between the free and fully saturated hFynSH3 protein. In a conventional NMR approach two 550μl samples were prepared, both containing 0.1 mM concentration of hFynSH3, and one with 2.1 mM p85$\alpha_{\text{P91-T104}}$, as detailed in table 6.1. By repeated exchange of volumes between the two samples a ligand-to-protein molar ratio (L/P) between 0.0 - 27.0 was generated. At each point ^{1}H-^{13}C and ^{1}H-^{15}N HSQC spectra were recorded. The overlay of all spectra is shown in fig. 3.9, where the full ^{1}H-^{15}N HSQC spectrum is presented in fig. 3.9 A and the methyl section of the ^{1}H-^{13}C HMQC is presented in fig. 3.9 B. Individual chemical shift perturbations of the protein peaks can be observed in both sets of spectra. The linear profile of all CSPs suggests that only two states of the protein are available, i.e. the free and saturated hFynSH3, in line with the previously defined interaction profile for the hFynSH3 - p85$\alpha_{\text{P91-T104}}$ pair[114,131]. Within the experimental conditions the binding equilibrium is in fast exchange, hence only one population-averaged peak is observed for each resonance at a given L/P, as explained in section 2.1.5. The system approaches saturation at L/P $\sim$ 5.0, where no more changes to the chemical shifts of individual signals can be observed.

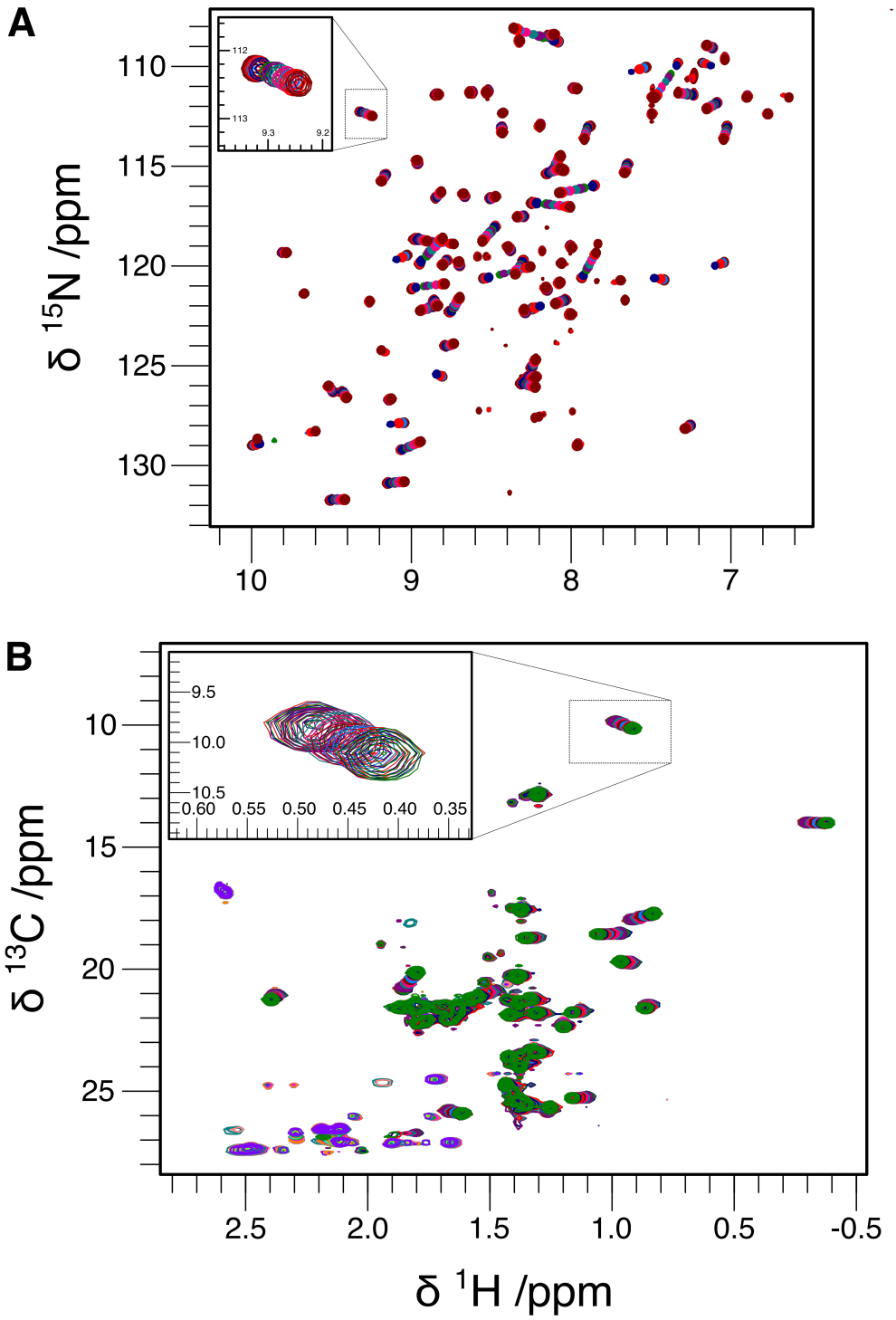

Figure 3.9: Superposition of the (A) ^{1}H-^{15}N-HSQC and (B) the methyl region of ^{1}H-^{13}C-HMQC spectra recorded for each point during the hFynSH3 - p85$\alpha_{\text{P91-T104}}$ titration. Sample conditions: 0.1 mM hFynSH3, 0 - 2.1 mM p85$\alpha_{\text{P91-T104}}$ in H_2O analysis buffer and 5% D_2O (550 μl); spectra recorded at 16.45 T with the Prodigy TCI CryoProbe (Bruker, US) at room temperature.

3.3.2 K_D, thermodynamics and kinetic profile

As visible in fig. 3.9, the basis for the hFynSH3 - p85$\alpha_{91\text{-}104}$ binding characterisation are the chemical shift perturbations of individual protein signals, induced by the concentration of the ligand. Individual CSPs, $\Delta\delta$, are calculated as following:

$$\Delta\delta_{N/H/C} = \delta_i - \delta_0, \tag{3.2}$$

where δ_i is the chemical shift position of an individual signal on the δ ^{1}H, δ ^{15}N or δ ^{13}C axis at a given concentration of p85$\alpha_{91\text{-}104}$, while δ_0 is the equivalent position of the same signal for the free-form hFynSH3. Reducing the two-dimensional representation of individual signals, the isotope-weighed CSPs, $\Delta\delta_{comb}$, are calculated as weighted Euclidean distance[173]:

$$\Delta\delta_{comb} = \sqrt{\frac{{\delta_H}^2 + (\alpha\ {\delta_X}^2)}{2}}, \tag{3.3}$$

where X corresponds to the identity of the hetroatom (^{13}C or ^{15}N) and α is the isotope scaling factor. In this work the suggestion of Williamson[173] was followed and $\alpha = 0.14$ was applied universally.

The characterisation of the hFynSH3 - p85$\alpha_{\text{P91-T104}}$ binding is carried out based on the time-dependent nature of molecular interactions where the protein, P, and ligand, L, associate to form a protein - ligand complex, PL. The process is represented by:

$$P + L \underset{k_{\text{off}}}{\overset{k_{\text{on}}}{\rightleftharpoons}} PL \tag{3.4}$$

where k_{on} and k_{off} are the kinetic rate constants relating to the association and dissociation of the two species. In equilibrium, the process is defined by the dissociation constant, K_D, expressed in mol/dm^3 units, which relates to the ligand concentration at which half of all protein molecules are populated with the ligand:

$$K_D = \frac{k_{\text{off}}}{k_{\text{on}}} = \frac{[P][L]}{[PL]} \tag{3.5}$$

The K_D is a universal measure of affinity, however in practical terms the stability of the protein - ligand complex is defined by Gibbs free energy, ΔG:

$$\Delta G = -RT \ln K_D = \Delta H - T\Delta S \tag{3.6}$$

where R is the universal gas constant (8.314 J K^{-1} mol^{-1}), T is temperature measured in Kelvin, ΔH and ΔS are the enthalpic and entropic contributions, respectively. For the purpose of the CSP analysis eq. (3.5) can be rewritten as (details in section 6.5.2):

$$\frac{\Delta\delta_{comb}}{\Delta\delta_{max}} = \frac{(K_D + [L] + [P]) - \sqrt{(K_D + [L] + [P])^2 + 4[L][P]}}{2[P]} \tag{3.7}$$

where $\Delta\delta_{max}$ is the isotope-weighted CSP observed for a fully saturated hFynSH3 signals, $[L]$ and $[P]$ represent the total ligand and protein concentrations at a given ligand-to-protein ratio. Next, experimentally derived CSPs are plotted against the L/P and the data are fitted to the model, described by eq. (3.7), where K_D is treated as a free parameter. Exemplary binding curves, calculated for the Trp^{119} indole Hϵ/Nϵ and Asp^{118} Hβ/Cβ signals identified to have direct contact with the ligand, are shown in fig. 3.10. Fitted K_D values are 16.13 $\pm$ 0.57 μM and 15.64 $\pm$ 1.83 μM, respectively. Individual K_D values were determined for all CSPs above the σ_c significance threshold. Specific examples are presented in table 3.1, while the complete list is included in tables A.2 and A.3 in the appendix. All values are in good agreement, converging to a common mean of 17.8 μM and 3.9 μM standard deviation. Similar values were obtained when taking into account the errors associated with the preparation of the samples, explained in section 6.5.1. Moreover, all K_D values replicate closely the isothermal titration calorimetry (ITC) measurements reported previously by Renzoni et al.[131]. The following results prove NMR as a reliable method for characterisation of ligand binding. Furthermore, the atomic-scale resolution unattainable by most methods allows to clarify that all signals sufficiently perturbed by the binding event report the same K_D, regardless of their position within, in the proximity of the binding site or further away.

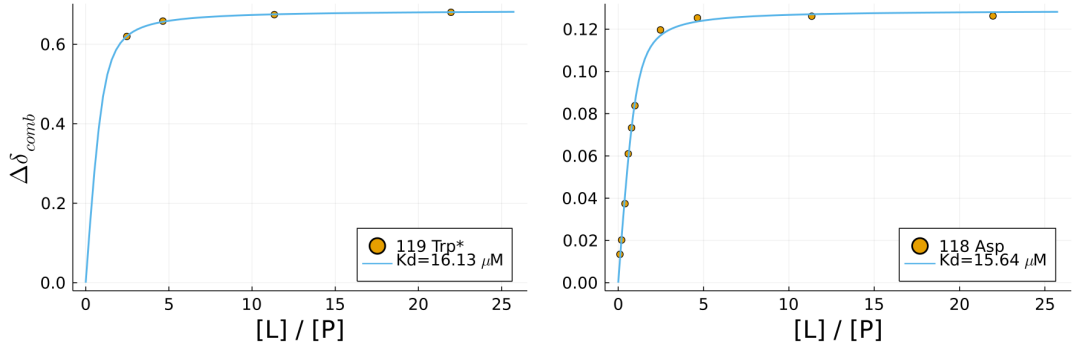

Figure 3.10: Exemplary binding isotherms for the sidechain indole NH of Trp^{119} (left) and Asp^{118} Hβ/Cβ (right) signals reporting direct contacts to the p85$\alpha_{\text{P91-T104}}$ peptide. Scattered are the experimental data, while the solid line represents the best fit model to eq. (3.7).

Following from eqs. (3.5) and (3.6) further claims can be made regarding the thermodynamic and kinetic profile of this interaction. The Gibbs free energy, ΔG, is the ultimate measure of stability of the protein - ligand complex and represents the free energy change in the system transitioning between the available thermodynamic states. For the hFynSH3 - p85$\alpha_{91\text{-}104}$ binding the overall calculated ΔG is 27.1 kJ mol^{-1}, while individually calculated values are also listed in table 3.1. ΔG is a global measure of the system, governed by its enthalipc and entropic contributions. As explained earlier, the favourable, i.e. negative, ΔG in this case is attributed mainly to the enthalpic effects associated with formation of hydrophobic interactions, while a notable entropic penalty

is exerted on the system upon binding as the p85$\alpha_{\text{P91-T104}}$ peptide assumes the PPII helix and the hFynSH3 structure rigidifies in response to aromatic ring reorientation and stabilisation of the n-Src and RT loops. This is likely to affect the binding kinetics defined by the k_{on} and k_{off} kinetic rate constants. For most protein - small ligand binding events, the k_{on} can be assumed to be diffusion limited, i.e. in the order of $\sim 10^7$ s^{-1} M^{-1}, therefore allowing for straightforward estimation of k_{off}, based on eq. (3.5). Assuming the above, the resulting k_{off} is approximately 170 s^{-1}, however the reorientation of the ligand into the PPII helix is likely to result in lower k_{on}. In such case, for the binding to be represented the same K_D, the k_{off} would need to be equivalently reduced.

Resonance	K_D / μ**M**	**Error /**μ**M**	ΔG **/kJ mol**$^{-1}$
Ala^{95} (Hγ/Cγ)	18.44	2.77	27.0
Tyr^{132} (Hα/Cα)	14.94	3.40	27.5
Asp^{100} (NH)	19.17	7.08	26.9
Tyr^{137} (NH)	16.38	1.20	27.3

Table 3.1: Exemplary K_D values calculated according to the sidechain and backbone detected CSPs. All individual K_D values ale listed in tables A.2 and A.3 in the appendix.

3.4 Conclusions

This chapter has described the strategies and efforts undertaken to best characterise the structural aspects of the hFynSH3 - p85$\alpha_{\text{P91-T104}}$ binding, based on heteronuclear NMR data. In the analysis, over 95 % of the backbone amide and aliphatic side chain signals of hFynSH3 were assigned, while the assignments were also extended onto the protein aromatic groups. Individual signals responsive to the binding were identified on hFynSH3, those were located mainly within the binding surface. No change to the protein secondary structure was observed upon binding. Perturbations of the protein chemical shifts were recorded in response to the increasing concentration of the ligand, based on which the evaluation of the equilibrium dissociation constant, K_D was possible. The resulting K_D was 18 $\pm$ 4 μM, which is fully supported by the previously published data. The breadth of the information provided by NMR demonstrates the unique capacity of this method to provide atomic-scale information about biomolecules and their interactions in solution.

Chapter 4

System design, operation and validation of the automated LoC-μNMR device

The following is an extension of the "Microfluidic platform for serial mixing experiments with *in operando* nuclear magnetic resonance spectroscopy" article by M. Plata, W. Hale, M. Sharma, J. M. Werner and M. Utz published in February 2021 in the Royal Society of Chemistry's *Lab on a Chip*. The chapter describes the design and function of the microfluidic device developed in the course of the 'Protein NMR on a Chip' project and provides it's performance characteristics for implementation of serial mixing experiments.

4.1 Background

Lab-on-a-Chip devices allow efficient experimentation with sub-μL sample volumes, and quite complex experimental protocols can be implemented using pneumatically actuated valves[164], digital microfluidics[140], and ultrasound separation[119]. Commonly, data readout in LoC systems is based on fluorescence spectroscopy[65,109], mass spectrometry[17], UV-vis spectroscopy[91], plasmonics[185] or electrochemistry[46].

In contrast, NMR has largely remained outside of the focus of microfluidics, despite its wide range of applications. The versatile, specific and non-invasive character of NMR allows to examine, in parallel, different characteristics of the same sample. For example, detailed reaction monitoring[97] may be coupled with chemical analysis[33] and molecular structure determination[100]. Conventional liquid-state NMR uses relatively large samples, of the order of ~ 500 μL, and reaches concentration limits of detection around 10 $\mu\mathrm{M}\sqrt{\mathrm{s}}$. Miniaturised receiver coils offer significantly improved mass limits

of detection[10,121,178]. A number of low-volume detectors[108,132,134] and capillary flow NMR systems[33,63,69,77] have been described on this basis. In some cases, systems with simple planar microfluidic devices that can be inserted and removed from the micro-NMR probe have been proposed[47,138,150,153]. However, it is challenging to integrate non-trivial microfluidic functionality such as valving and pumping into such μNMR platforms[188]. Complexity on the chip tends to lead to a loss in spectral resolution due to differences in magnetic susceptibility of the components[137]. Moreover, ancillary hardware such as solenoid valves are not compatible with high magnetic fields, and the space inside the NMR bore is very constrained. A common approach has been to carry out most of the flow manipulation away from the spectrometer[26,63,77,89,97] and deliver the final sample to the NMR detector by a several meters long capillary.

An exception is the work by Swyer et al.[157] who have successfully integrated electrically actuated digital microfluidics (DMF) with NMR. Based on electrowetting phenomena, DMF allows flexible manipulation of liquid droplets in contact with a dielectric surface. The current chapter demonstrates that NMR can also be successfully combined with conventional, pressure-driven microfluidics and pneumatically actuated valves. While DMF is very versatile, pressure-driven microfluidics has advantages in certain circumstances. It is insensitive to the type of fluid being used, whereas DMF requires ionic solutions, or at least a solvent with high dielectric constant. DMF devices also require lithographic processes to define the electrodes, along with careful control of surface properties, while pressure-driven fluidic devices are simple and can be produced cost-effectively. This work demonstrates that with rapid prototyping techniques such as laser cutting, heat binding and 3D printing conventional pneumatically actuated on-chip valving[11,56,164] and pumping can be implemented on a microfluidic device capable of *in situ* operation inside the NMR spectrometer.

In the following, a device is described which implements serial mixing experiments, executed autonomously, coupled to and *in operando* detection by high-resolution μNMR spectroscopy. Serial mixing experiments, where two solutions are mixed in systematically varying proportion, are widely used in chemistry and life sciences. They are fundamental for the determination of binding constants[66], to acquire kinetic data[66,115], and for toxicity studies,[52] to name but a few examples. Microfluidic implementation of such experiments offers automation of what is otherwise a very repetitive task, with advantages in cost and reliability. Also, miniaturisation is an advantage if one of the reactants involved is costly and/or only available in small quantities. Mixing of the liquids however, is a common bottleneck for microfluidics systems. One effective solution is offered by circular micromixers[31,163], often with pneumatically actuated microvalves and pumps[56,164], which rely on deformation of elastomer membranes, usually PDMS. Elastomer structures are problematic in the context of NMR as they cause broad background signals that are difficult to suppress. It is therefore necessary to keep the elastomer away from the NMR detection area[186].

4.2 System design

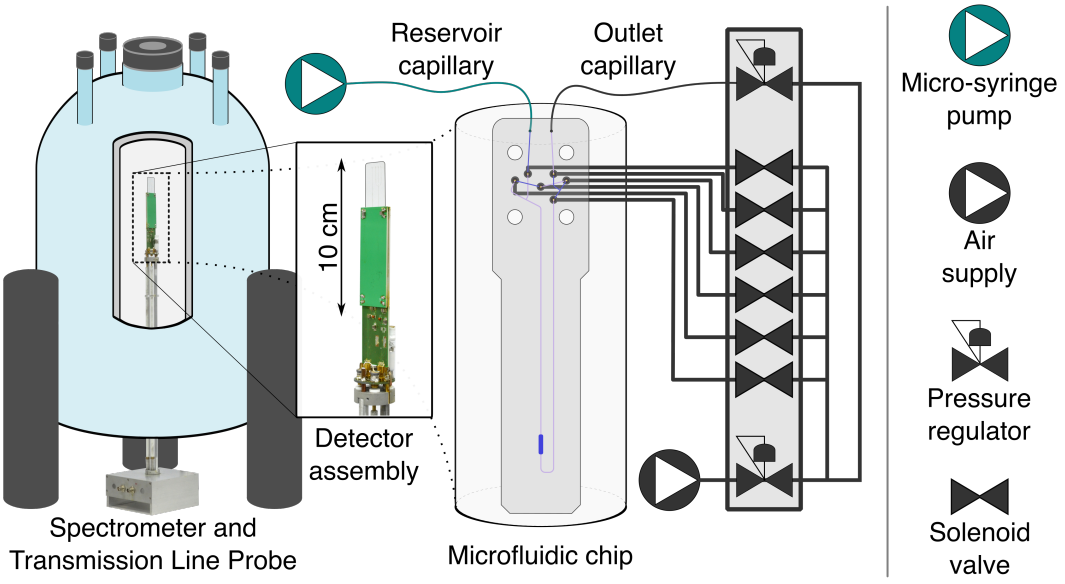

Figure 4.1: Macroscale to microscale representation of the microfluidic device and its fit inside the NMR spectrometer. From the left the position of the device and the probe inside the spectrometer is shown, the following is a blow out of the probe detector with the microfluidic chip inserted, in the middle a drawing of the chip design is presented with schematic connections to the control devices, which are located outside of the spectrometer. Those are drawn in a simplified form and labelled.

The LoC-μNMR system builds on the double-resonance transmission line probe developed in the Utz lab[47,150,186]. This probe was designed to accommodate generic microfluidic devices inside a standard NMR spectrometer, and record NMR signal from a 2.5 μl chamber on the microfluidic device. The probe and microfluidic device are of a corresponding geometry, such that, when placed inside the magnet, the detection chamber is exposed to maximum static and RF magnetic fields[47]. Apart from the fixed size and position of the detection chamber the LoC-μNMR system does not constrain the fluidic design, allowing for a wide range of functionalities can be implemented. In the present case, the microfluidic chip accommodates a number of microvalves, which are actuated pneumatically using solenoid valves located outside of the NMR magnet. A micro-syringe pump, also kept externally, is used to inject precisely measured aliquots into the chip.

Figure 4.2 A shows the chip design developed to address the demands of the 'Protein NMR on a Chip' project. Those are: minimised volume of operation, ability to repeatedly and adequately mix two solutions and operate autonomously inside the NMR

spectrometer. The critical element of this design is a set of six microvalves[11] (numbered 1 - 6 in fig. 4.2 A) actuated pneumatically and positioned away from the detection area, which dictate the behaviour of the sample liquid. The larger microfluidic circuit on the chip consists of the detection chamber, connected to the chip inlet and outlet through a pair of cut-off valves (1 and 2 in fig. 4.2 A). A bridge pathway, equipped with valves 3–6, allows peristaltic circulation (mixing) of the liquid contained on the chip. During injection and filling, cutoff valves are kept open, whereas the bridge pathway is closed using valve 4. During mixing, the chip is isolated from the supply by closing the cutoff valves, and valves 3–5 are actuated periodically with a phase shift to create a peristaltic motion of the liquid[164]. The total volume subject to circular peristaltic mixing (V_s), consisting of the detector chamber, valves 3–6, and connecting channels amounts to $\sim$ 10 μL. This is highlighted in fig. 4.2 C as the mixing circuit.

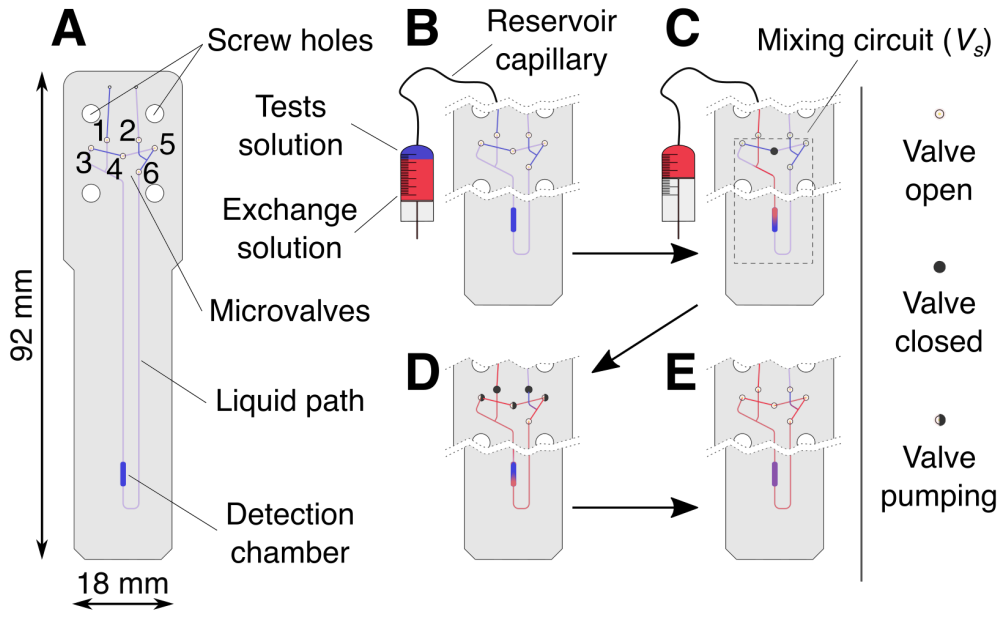

Figure 4.2: Model of the microfluidic chip designed for the serial mixing experiment (A) and graphic representation of the experimental procedure including injection (B→C), mixing (D), and acquisition (E). For visualisation purposes, solution mixture normally present only inside the reservoir capillary and microfluidic chip, here is demonstrated to fill the syringe volume.

The full-scale microfluidic device is built from two fundamental elements: **a**) the microfluidic chip, where the sample is maintained, and **b**) the chip holder matrix that facilitates dynamic manipulation of the sample (see fig. 4.3). Device assembled from both elements is small enough to fit inside the confined space of the NMR spectrometer bore. To function, the chip holder is interfaced with 1/16" capillary tubing for liquids and 3 mm tubing for pneumatics that extend to the micro-syringe pump and solenoid valves, located outside of the spectrometer. Actuation of the chip microvalves relies on the deformation of two elastomer membranes, i.e. PDMS and nitrile rubber (NBR)

placed between the chip and the holder, in response to ∼ 5 bar of pressurised air regulated by opening and closing of the solenoid valves. Two PDMS membranes are placed between the chip and chip holder to act as an o-ring and provide sealing for the liquid. NBR is utilised as gas barrier, to prevent the pressurised air to seep into the sample liquid. This membrane is placed between the chip holder and the PDMS membrane covering the valves on the microfluidic chip.

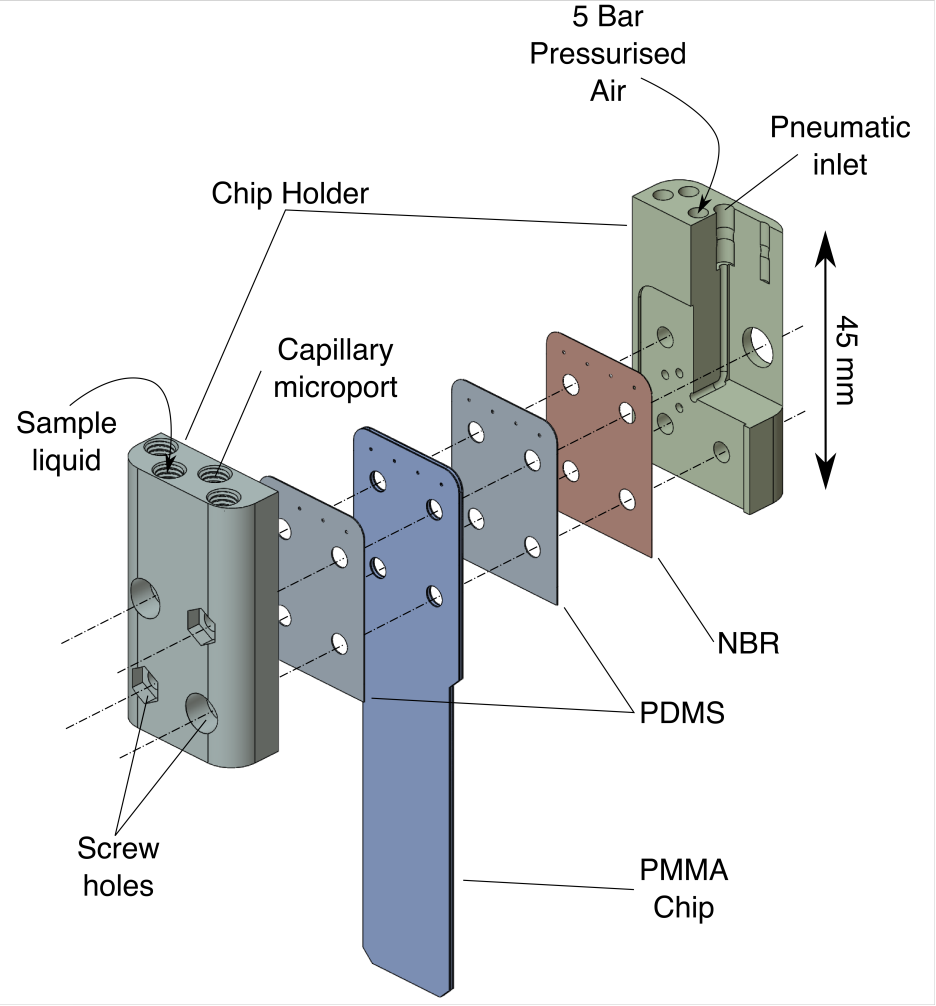

Figure 4.3: A 3D render demonstrating the assembly of the microfluidic device from all components.

The operator maintains full control over the device and can choose to actuate individual valves or execute the pre-defined mixing routine by choosing the duration and frequency of valve actuation. The flow of the sample into the device is dictated by the connected micro-syringe, where the operator specifies desired volume and flow rate. Supplementary to the manual operation of individual components, an automated script was written in LabVIEW with assistance from Dr Manvendra Sharma, which executes the pre-defined experimental schedule according to the operator's choice of parameters. The details on the device operation are laid out in the following section.

4.3 Experimental protocol

The experimental procedure is controlled by the operator via the LabVIEW script, which transmits individual commands to the three separate hardware units: the micro-syringe pump responsible for the injection of the sample into the device, Arduino controller that governs the actuation of the solenoid valves, and the spectrometer for data acquisition. The script implements a state machine model with two modes of operation. The general scheme is shown in fig. 4.4 while the detailed pattern is described in fig. B.1 in the appendix. The (A) manual state is designed for the operator to assemble and fill the device with the sample before placing it inside of the spectrometer, while (B) the automated state only requires the operator to specify a set of parameters that govern the execution of the pre-defined experimental schedule, i.e. the serial mixing experiment. In the preparation stage (detailed in section 6.1.2), the reservoir capillary is filled with two solutions, 15 - 20 μL each, as demonstrated in fig. 4.2 B. During (A) the reservoir capillary is connected to the device inlet, while the outlet is connected to 1.5 - 3 bar of pressurised air. Approximately 12 - 15 μL push by the micro-syringe is needed to fill the mixing circuit of the device with only the 'test' solution, while the 'exchange' solution remains outside of the circuit. Filling is carried out in two steps. First, the majority of the mixing circuit, including the detection chamber, is filled by ~ 9 μL push of the micro-syringe supplemented by the closing of valve 4, as presented in fig. 4.2 C. Secondly, the bridge pathway is purged of the remaining air, as ~ 3 μL is pushed through the chip's fluidic circuit with valve 6 closed. The filled device is placed inside the spectrometer for calibration, allowing to record the initial spectra. Next, the operator needs to define the following parameters: the number, rate and volume of injection steps, mixing time, and delay times corresponding to the acquisition of individual spectra, before (B) is executed. The acquisition schedule is specified separately in TopSpin® (Bruker, US) as a list of queued experiments. Experiments to be carried out after each injection and mixing contain a conditional statement which awaits a 5 V pulse, before the acquisition is carried out. The 5 V 'trigger' pulses are sent to the spectrometer from the Arduino controller, following the execution of each injection and mixing. The steps carried out during (B) are broadly similar to those of the filling routine. Once (B) is initiated, the specified volume increment (V_i) of the exchange solution is pushed by micro-syringe action towards the detection chamber as valve 4 is closed, displacing an equivalent volume of the test solution out of the mixing circuit (fig. 4.2 C). Once the micro-syringe has stopped, a trigger pulse is sent to the spectrometer to acquire the first injection spectrum. The state machine then awaits for the acquisition to be complete, according to the scan delay parameter specified by the operator. Following this period, valves 1 & 2 seal the V_s (fig. 4.2 D), and with sequential triggering of the valves 3, 4, 5 a peristaltic flow is induced in order to mix the two volumes. Once the specified mixing period has passed, the second trigger pulse is dispatched to the spectrometer while the state machine again remains idle during the designated scan

delay. Next, the loop counter evaluates the number of remaining injection steps before the new V_i increment is pushed. The experiment is completed once all injection steps have been implemented. Alternatively, the operator also has the ability to terminate the experiment at any time.

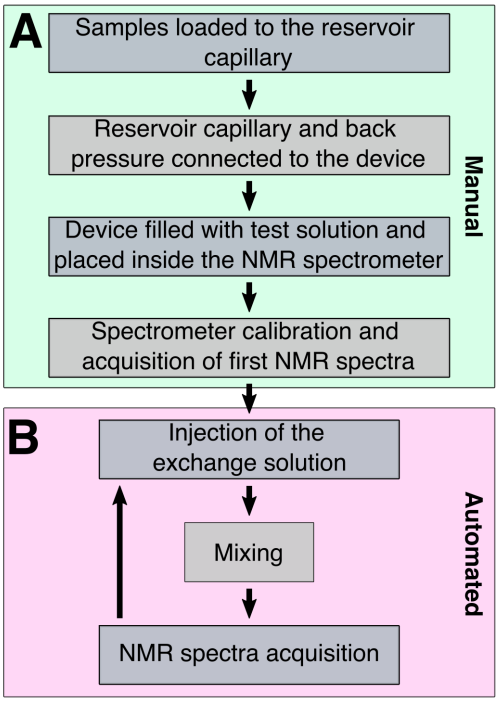

Figure 4.4: LoC-μNMR operation algorithm for a two-solution serial mixing. Two periods can be distinguished: manual (A), when the operator prepares the experiment, and automated (B), associated with the experimental run according to the pre-specified schedule.

4.4 Functional characterisation

4.4.1 Microvalve function

The performance of the microvalves is critical to the overall function of the LoC device. During the serial mixing experiments they serve two distinct functions: **a**) closing of specific valves determines the flow path of the sample liquid, and **b**) sequential valve triggering pattern creates the peristaltic flow needed for sample mixing. Valve closing is achieved when the applied pressure to the valves exceeds the pressure generated by the flow of the liquid, and is sufficient to push the elastomer membranes against the valve floor (see fig. 4.5 D). Required pressure was determined experimentally for each of the valves. A water filled capillary was connected to the device inlet and the flow was generated with application of 4 bar air pressure at the capillary end. The flow was observed by naked eye at the device outlet. For all tested chips, 5 bar air pressure

applied to each of the valves was effective to stop the flow of the liquid through the device. Function of the microvalves was unaffected by the long ($\sim$ 4 m) pneumatic tubing.

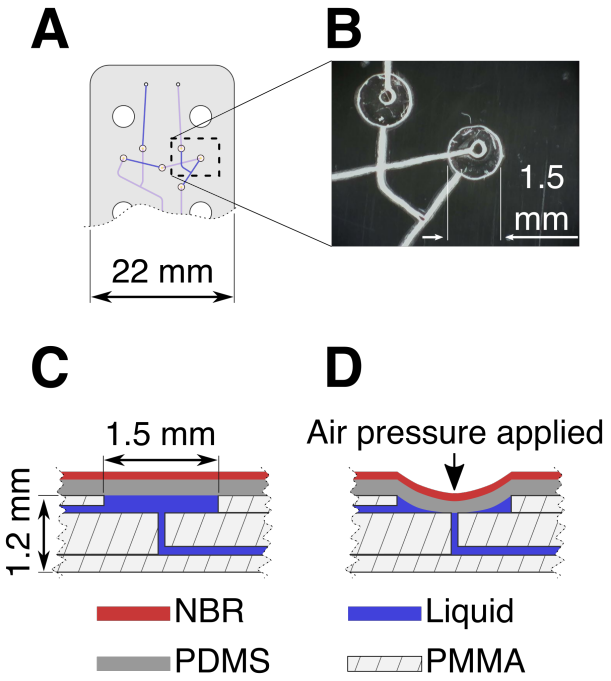

Figure 4.5: Detail view (A) and micrograph (B) of the chip microvalves. Cross section of a single microvalve (C) and its actuation principle (D).

It is clear from the device design (fig. 4.2 A) that the 2.5 μl detection chamber only represents a fraction of the mixing circuit (V_s) of the microfluidic chip. During the serial mixing experiment, each injection alters the mixture composition inside the V_s. Taking into account the dimensions of only the detection chamber and the standard rate of diffusion it can be expected that in a low *Re* system, such as this one, it would take well over one hour for the mixture to become homogenous if no active mixing mechanism is involved. This signifies the importance of the peristaltic flow induced with the microvalve action.

Due to the asymmetrical circuit design it is possible to distinguish two opposite directions of the flow inside the V_s. Here, those are referred to as clockwise and anticlockwise. While the flow is created by sequential actuation of valves 3, 4, 5 (fig. 4.2A), valve 6 remains open during this routine and contributes to the fluidic capacitance of the circuit. In the clockwise direction valve 6 is positioned downstream from valves 3, 4, 5, and upstream in the anticlockwise direction. This asymmetry is reflected in the liquid flow observed inside the V_s. In a series of serial mixing experiments, injection of Bromophenol Blue (BpB) dye to the V_s was carried out in order to visualise the flow, and the time needed to reach sample homogeneity was measured. Such results are shown in fig. 4.6. At $t = 0$, 1.5 μL of the BpB solution was injected into the detection

chamber. The injection flow is downward, as indicated by an arrow in the figure. The boundary between the BpB and test solution (H_2O) is clearly visible in the detection chamber. The peristaltic flow in the clockwise direction was initiated, leading to an upward movement of the liquid in the image (arrow). After 40 s, the blue boundary between the fluids reaches the detection chamber from below. The liquid continues to flow around the mixing circuit, gradually getting mixed in the process. After 60 s, the colour gradient is still visible, while it can no longer be distinguished by eye after 120 s of mixing.

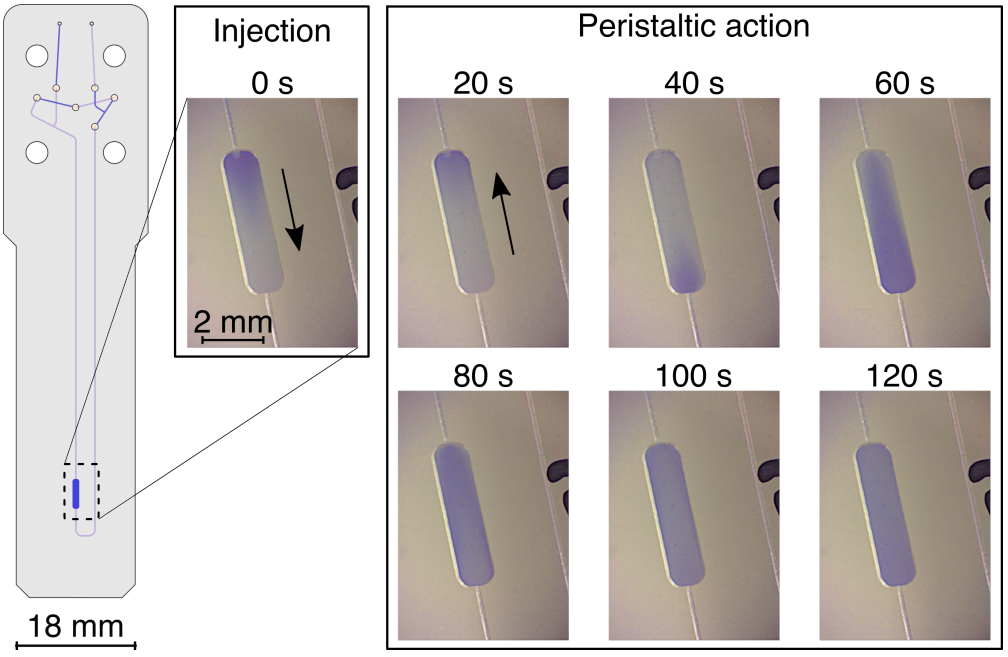

Figure 4.6: Visualisation of the flow inside the detection chamber of the microfluidic chip. Images were taken at specified time points after initial injection of the BpB dye. Arrows indicate the direction of the flow at each step.

Similar observations were made to evaluate the flow rates produced by the peristaltic action. A 1 - 3 μL volume of a perfluorinated oil (Fluoinert^{TM} FC-43; Sigma-Aldrich, UK) was injected into the aqueous solution present in the mixing circuit before the peristaltic action was initiated. As the two solutions were essentially non-mixing, the circulating oil droplet could be observed within V_s. From the known volume of the detection chamber and the time needed for the droplet to cover that volume, the flow rates reached by the peristaltic action were estimated. The average values are 5 ± 2.5 μl/min clockwise, and 1.5 ± 0.7 μl/min anticlockwise. The variability in the flow rate is attributed to the fabrication tolerances of the microfluidic chips. Further experiments were carried out inside the spectrometer, where a solution of sodium trimethylsilyl-propanesulfonate (DSS) dissolved in fumaric acid was injected into the fumaric acid only solution at the same concentration. Mixing efficiency was evaluated by observing the intensity change of the appropriate NMR signals, 0 ppm for the methyl protons

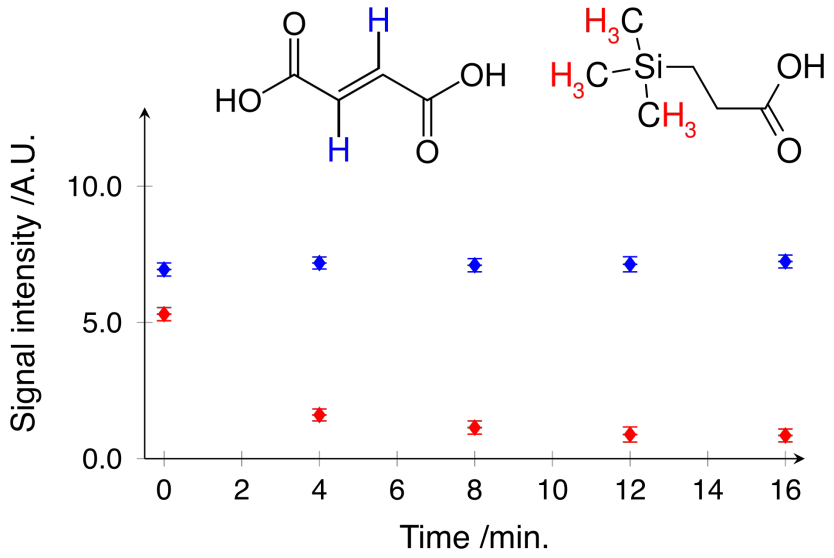

Figure 4.7: In-spectrometer evaluation of the mixing efficiency for the microfluidic device. The scattered data show the intensity values for the 0 ppm and 6.52 ppm peaks originating from the methyl protons on DSS and methine protons on the fumaric acid, respectively. Signal intensities are normalised with respect to the number of contributing protons. Data were acquired after initial injection of DSS and Fumaric Acid solution into the Fumaric Acid only solution (time point 0), and following specified mixing intervals.

on DSS and 6.52 ppm for the methine protons on the fumaric acid, after a given mixing period. In fig. 4.7 the intensities of the NMR signals, normalised by the number of contributing protons, are plotted against the cumulative mixing time. It is clearly visible that after injection (time point 0), the intensity of the DSS signal is very strong, signifying high concentration in the detection chamber. After 4 minutes of mixing, the DSS signal has decreased by about two thirds, while the signal for the fumaric acid has not changed. This signifies that after mixing, the concentration of DSS is distributed more evenly within the mixing circuit, at concentration lower than that of the injected solution. Gradual decrease of the DSS signal is observed further until 8 - 12 minutes of mixing. Based on these observations the mixing time for all following experiments was set to 12 minutes.

4.4.2 NMR detected serial mixing

The evaluation of the *in situ* serial mixing procedure was carried out inside the spectrometer, where the intensities of the fumaric acid and DSS NMR signals were followed between consecutive injection and mixing steps. The two compounds, together with sodium acetate used as internal concentration standard, were chosen because they do not react and have well separated ^{1}H chemical shifts. The main resonances appear at 0 ppm, 1.92 ppm, and 6.52 ppm for the nine equivalent methyl protons on DSS, three

methyl protons on sodium acetate, and two equivalent methine protons on fumaric acid, respectively. Secondary signals due to methylene protons on DSS at 0.62 ppm, 1.77 ppm, and 2.92 ppm can be observed above ~ 5 mM.

The experiment was prepared with 20 μL each of the fumarate (exchange) and DSS (test) solutions in the reservoir capillary. The initial spectrum ($V = 0$ in fig. 4.8) was acquired after filling the device with 18 ± 1 μL of the test solution, according to the protocol outlined in section 4.3. The acetate and DSS signals are clearly visible in the spectrum, while the 6.52 ppm fumaric acid peak is barely above the noise level. Afterwards, eleven injection steps were carried out, with $V_i = 2 \pm 0.25$ μL, followed by 240 s of peristaltic mixing before acquisition. The gradual reduction in intensity for DSS, and increase for fumaric acid can clearly be observed in all subsequent spectra shown in fig. 4.8. Concentrations of DSS and fumaric acid were computed from the spectra based on the known concentration of acetate according to:

$$[\mathrm{X}] = \frac{I_\mathrm{X}}{I_\mathrm{Ac}} \frac{n_\mathrm{Ac}}{n_\mathrm{X}} [\mathrm{Ac}], \tag{4.1}$$

where $[\mathrm{X}]$ denotes the concentration of X in the detection volume, I_X is the integral of the corresponding NMR peak, and n_X is the number of protons per molecule contributing to that peak. $[\mathrm{Ac}]$, I_Ac and n_Ac are the corresponding identities of sodium acetate. Figure 4.9 shows the resulting concentrations of DSS and fumaric acid as a function of injected volume (solid diamonds). Vertical error bars are derived from the integration error due to spectral noise and estimated pipetting errors in preparation of the acetate stock solution (details in section 6.1.2). Horizontal error bars reflect the $\pm$ 0.25 μL repeating accuracy of the syringe pump. The solid lines in fig. 4.9 represent

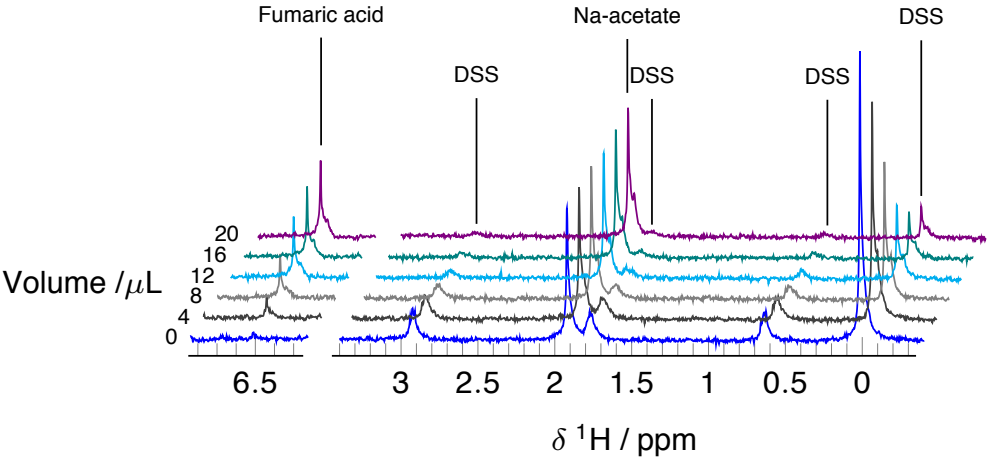

Figure 4.8: Series of ^{1}H spectra obtained during the serial mixing experiment between 35 mM DSS and 40 mM fumaric acid solutions in 50 mM sodium acetate at pH 13. Spectra are referenced to 0 ppm using the main DSS resonance and the traces are stacked according to the combined injection volume.

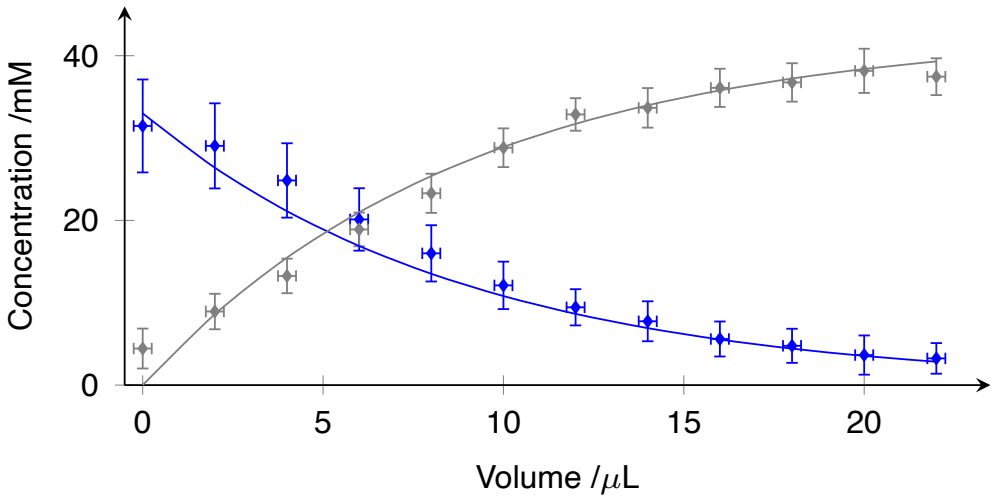

Figure 4.9: Concentration changes observed during serial mixing of DSS (blue) and fumaric acid solutions (gray). All values are normalised with respect to the signal intensity of the internal standard (sodium acetate). Scattered points represent the experimental data while the line-plots demonstrate the best fit model as specified by eq. (4.3). Concentration errors for the series shown are result of the propagation of errors associated wit the preparation of the samples and were calculated according to eq. (6.3). Volume uncertainties reflect the metering accuracy of the micro-syringe pump.

a least-squares fit of eq. (4.3) to the data, where V_s has been treated as the fitting parameter. While the microfluidic chips were designed for a nominal value of $V_s = 10$ μL, fabrication tolerances invariably lead to small differences. The accuracy of V_i is limited by the metering accuracy of the micro-syringe. The supplier offers a range of syringe sizes, each with specified metering accuracy. Here, a single 80 μL syringe (SG-080-C360; LabSmith, US) was used to reach the desired level of volume control. More precise operation can be carried out with parallel use of syringes of various sizes (e.g. 8 and 80 μL) via a Y junction, each designated for fine and bulk control.

4.4.3 Titration model

The concentration of a compound A in the detection volume after the k-th injection and mixing cycle is expected to be:

$$[A]_k = (1 - \frac{V_i}{V_s})[A]_{k-1} + \frac{V_i}{V_s}[A]_e, \tag{4.2}$$

where $[A]_e$ is the concentration of A in the exchange solution. The initial concentration $[A]_0$ is that of the test solution $[A]_t$. The composition after n steps is therefore:

$$[A]_n = (1 - \frac{V_i}{V_s})^n[A]_t + [1 - (1 - \frac{V_i}{V_s})^n][A]_e. \tag{4.3}$$

The above model allows to predict the concentration changes of the compounds in the analysed solution with respect to the repeated displacement of the volume of the mixing circuit by the specified V_i of the exchange solution. In the case where individual compounds are present only in the test and exchange solutions, a gradual and proportional increase and decrease can be observed, as exemplified by fumaric acid and DSS in fig. 4.9. Following from eq. (4.3) and the known concentrations of fumaric acid and DSS in the prepared solutions, the modelled changes are included as line-plots in fig. 4.9. Taking into account the estimated errors the model provides an adequate explanation of the data. However, there are few features in the data that suggest a more suitable model could be proposed. It can be noted that the initial concentration of fumaric acid in the analysed solution (at 0 μL in fig. 4.9) is higher than expected and is not explained by the associated errors. Furthermore, the fumaric acid signal is observed after filling the device with only $\sim$ 18 μL of the test solution, while 20 μL was loaded into the reservoir capillary. Similar observations were made on several occasions, where the initial NMR signal of the exchange solution was consistently detected 2 - 3 μL "sooner" than expected. Some of this effect can be contributed to the metering accuracy of the micro-syringe pump, however consistency of these observations suggest that some pre-mixing occurs between the two solutions before the initial injection of the exchange solution. This is not unexpected as the solutions remain in contact in the reservoir capillary. In a static system the contact surface is defined by the inner diameter of the capillary, i.e. 80 μm. A factor that is unaccounted for relates to the pressure driven flow, employed for loading of the solutions into the capillary and filling the microfluidic device. A model which takes into account the the extent of pre-mixing is yet to be defined. In its absence the approach is to use $\sim$ 5 μL excess of the test solution to fill the device, to ensure it is the only solution present in the mixing circuit at the start of the experiment.

4.5 Conclusions

The above summarises the design and operation of the microfluidic device capable of carrying serial mixing experiments while placed *in situ* inside the high-field NMR spectrometer. The highlight of this system is the automation and high-precision operation at microlitre volumes of tasks that are tedious and error prone when carried out manually. Results presented prove the device offers control over the concentrations of compounds inside the detection chamber as a function of the volume injected into the chip circuit. The current shortcomings are associated with the analytical model, which does not take into account the pre-mixing that occurs between the two solutions in the reservoir capillary. Another issue relates to the dead volumes of the microfluidic device, which approximately equal those of the detection chamber and microvalves

combined. The latter problem is mainly associated with the fabrication methods available in the Utz lab, however microfluidic techniques exist with the capacity to produce devices at higher precision. Therefore devices with significantly lower dead volumes could be fabricated based on the same design, further limiting sample use. More rigorous modelling, taking into account the pre-mixing, could offer the operating precision for applications where the sample's response to initial changes is highly pronounced. This would constitute an additional level of control and expand the platform's applications perspectives towards systems that depend on highly accurate reporting on the dose-response.

Chapter 5

Automated LoC-μNMR experiments for characterisation of hFynSH3-p85$\alpha_{\text{P91-T104}}$ binding by heteronuclear protein NMR

This chapter extends on the "Fully automated characterization of protein-peptide binding by microfluidic 2D NMR" article by M. Plata, M. Sharma, M. Utz and J. M. Werner, published in January 2023 in the *Journal of the American Chemical Society*. The work presented provides the proof-of-principle validation of the 'Protein NMR on a Chip' platform. Two fully automated experiments are described, where a series of ^{1}H-^{13}C and ^{1}H-^{15}N HSQC spectra of hFynSH3 was recorded with a gradually increasing concentration of the p85$\alpha_{\text{P91-T104}}$ peptide, implemented via the automated serial mixing protocol described in chapter 4. The acquired data are used to characterise the hFynSH3 - p85$\alpha_{\text{P91-T104}}$ binding, both in the structural and thermodynamic context. Finally, these results are qualitatively and quantitatively compared to equivalent data obtained with the commercially available state-of-the-art NMR hardware.

5.1 Background

Microfluidic Lab-On-A-Chip devices are finding increasing use in the life sciences as they provide unique, convenient and reproducible platforms for the interrogation of complex biological systems in highly controlled conditions and for quantifying their responses to defined stimuli using a variety of readout methods[19,35]. Limited sample use and integration of complex functionalities in LoC devices are intrinsically suited to the miniaturization and parallelization of biomedical workflows[92]. Biological systems

at all scales, ranging from whole organisms down to subcellular organelles and molecular assemblies have been studied in this way[39,83,95,135,182]. LoC devices have also been used for the study of protein-ligand interactions. However, these studies have so far relied on readout methods which require ligand modifications and lack detailed atomic information[7].

NMR is uniquely placed in characterizing macromolecular systems including protein-ligand interactions. It has the ability to determine the number and location of interaction sites, allosteric effects, the atomic structures and dynamics of ligands as well as protein, and a full thermodynamic evaluation of an interaction. NMR offers unique tools for structural and molecular biologists as well as medicinal chemists, because it does not rely on any protein or ligand modification for detection as well as offering substantial freedom in the choice and variation of buffer conditions. In addition, NMR is capable of probing a broad range of affinities (nM - mM)[50].

Typically large sample requirements in NMR, in the order of $\sim$ 500 μL and milligrams of protein, have been addressed by the development of detectors that require only microlitre sample volumes[10,121,188], and their applicability towards protein-detected high-resolution NMR has already been verified[125,134]. The contents of this chapter demonstrate how this mode of detection can be integrated with microfluidic sample manipulation to yield a modular LoC analytical experimental platform. Significantly, the experimental procedure is fully automated and integrated with commercially available NMR spectrometers and operating software. This reduces the efforts of the experimenter to the loading of the initial samples, specification of the titration schedule and the NMR acquisition parameters, in contrast to the continual manual sample manipulation for a conventional NMR titration, discussed in section 3.3.1.

5.2 Approach

The following demonstrates the NMR detection coupled with a microfluidic system that automatically controls serial mixing experiments, as described in chapter 4, for the characterization of protein-ligand interactions by high-resolution heteronuclear protein-detected NMR. In this modality, a series of 2D heteronuclear spectra of a uniformly labelled protein (either ^{15}N or ^{13}C) are acquired with increasing ligand-to-protein molar ratios. The fraction bound of protein is observed as CSPs of individual protein atoms. While conventional implementation of such experiments require repeated manipulation of $\sim$ 500 μL samples, therefore using a significant amount of labelled protein, the automated system presented here uses less than 40 μL for the entire titration experiment. This provides both atomic-scale identification of the binding site and quantification of the dissociation constant for the ligand, K_D[173]. Analysis of CSPs of the backbone amides using ^{1}H-^{15}N HSQC experiments takes advantage of the fact that

amides provide a single probe at every backbone position of a protein, with exception of prolines, but are typically limited to proteins below $\sim$ 50-100 kDa[51,124,141]. Focusing on protein methyl groups allows to study structure and interactions of much larger proteins or molecular assemblies even to MDa protein complexes[128,146,172] due to the favourable relaxation properties.

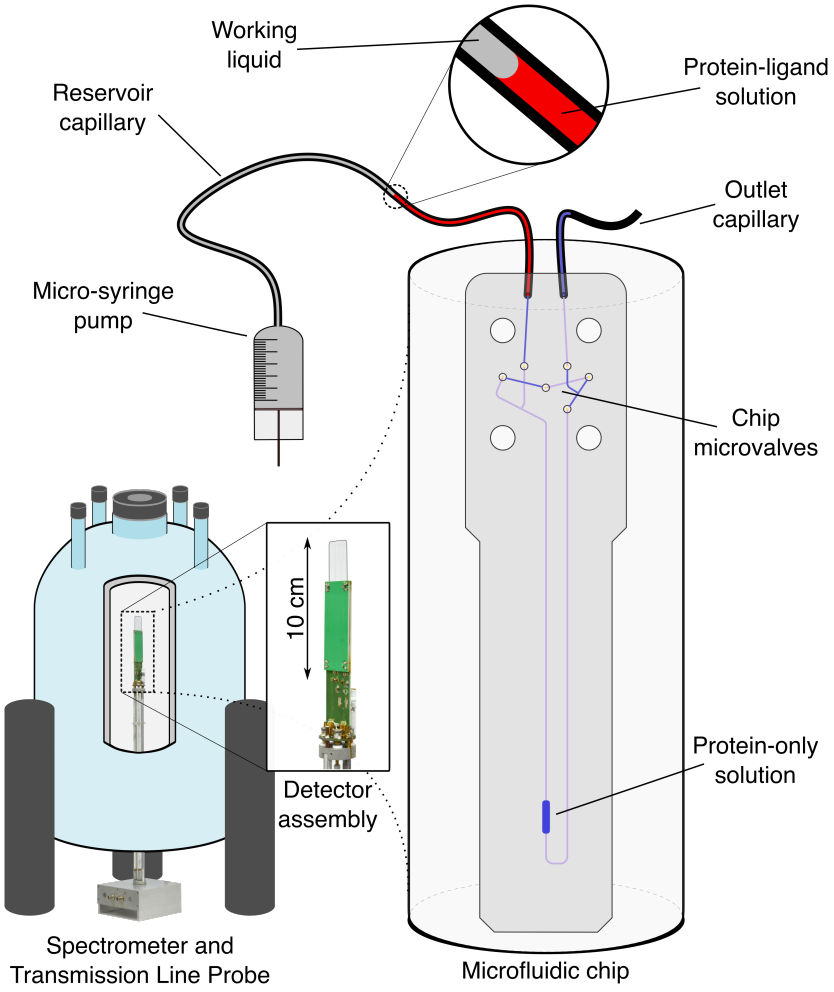

Figure 5.1: Schematic representation of the microfluidic device setup at the start of the titration experiment. After filling, the microfluidic chip contains $\sim$10 μL of the protein-only solution while 15-20 μL of the protein-ligand solution is present in the connecting reservoir capillary. By the action of the micro-syringe pump, connected at the end of the reservoir capillary, specified volume of the protein-ligand solution is injected into the chip circuit. Subsequently, the chip microvalves are employed to created a peristaltic flow inside the closed circuit on the chip and the two solutions are mixed until equilibration, before the multidimensional HSQC spectrum is recorded.

As explained in section 4.2, the experimental procedure is carried out using two solutions, one containing only the protein of interest, hFynSH3, the other containing the protein and excess of ligand, p85α$_{P91\text{-}T104}$, sufficient for the saturation of the protein. Only 20 μL of each solution is necessary to carry out the entire experiment. The device

is assembled and filled, so that only the protein sample is present within the chip mixing circuit at the start of the experiment, when the device is placed inside the spectrometer, as pictured in fig. 5.1. Initial acquisition is carried out to define the baseline, i.e. chemical shifts of the free protein, before the serial mixing procedure is implemented. In between of successive heteronuclear spectra, a single ^{1}H spectrum is acquired after each injection and mixing step to follow the intensity of the 0 ppm TSP signal, present in known excess in the protein-ligand solution. Therefore, the intensity of the TSP signal maintains linear correlation to the concentration of p85α$_{P91\text{-}T104}$ and provides reliable readout of the fraction bound of hFynSH3 in the analysed mixture at each step of the experiment. The fully automated process delivers a series of 2D HSQC spectra, from which the CSPs of individual signals are calculated. These data are then fitted using an appropriate binding model in order to determine the dissociation constant, K_D [173]. Having previously assigned the majority of the signals in the ^{1}H-^{13}C and ^{1}H-^{15}N HSQC spectra, as presented in chapter 3, the binding surface can also be identified from the same set of spectra.

5.3 Binding characterisation based on the μNMR data

Validation of the 'Protein NMR on a Chip' platform is based on two automated titration experiments with acquisition of full ^{1}H-^{15}N HSQC spectra and ^{1}H-^{13}C HSQC spectra focused on the hFynSH3 methyl groups. Figures 5.2 and 5.3 show an overlay of the selected spectra, at increasing p85α$_{P91\text{-}T104}$ concentration, acquired throughout the automated procedure. For clarity, only seven of each ^{1}H-^{13}C and ^{1}H-^{15}N HSQC spectra are shown, with the molar ratios of ligand-to-protein for each spectrum detailed on the right-hand side panel of the figure. Each spectrum was recorded with approximately 43 or 61 μg of ^{13}C- or ^{15}N-labelled hFynSH3 in the 2.5 μL volume of the detection chamber, respectively. Using a standard HSQC sequence [15] the entire titration series of 11 experiments in each case was completed in approximately 24 hours. The quality of acquired spectra allow to unambiguously assign 89 % and 65 % of the observable amide and methyl signals of hFynSH3, respectively, and to distinguish chemical shift differences above 31 Hz / 51 ppb or 20 Hz / 34 ppb, which relates to 8 - 21 % and 26 - 54 % of the maximum CSPs for the individual signals in the ^{1}H-^{15}N and ^{1}H-^{13}C HSQC spectra. The binding equilibrium for hFynSH3 and p85α$_{P91\text{-}T104}$ is in fast exchange and approaches saturation at a ligand-to-protein molar ratio of about two, as can be seen from from the minimal change in the chemical shifts at the molar ratios above $\sim$ 1.6 in figs. 5.2 to 5.4. Similarly to the results shown in section 3.3.1 all observed CPSs follow a straight line between free and bound form of hFynSH3, validating the choice of the two-state interaction model for the analysis.

Acquisition of the ^{1}H-^{15}N HSQC spectra allows to map the individual CSPs onto the backbone of the known structure of hFynSH3, as presented in fig. 5.6. From a total

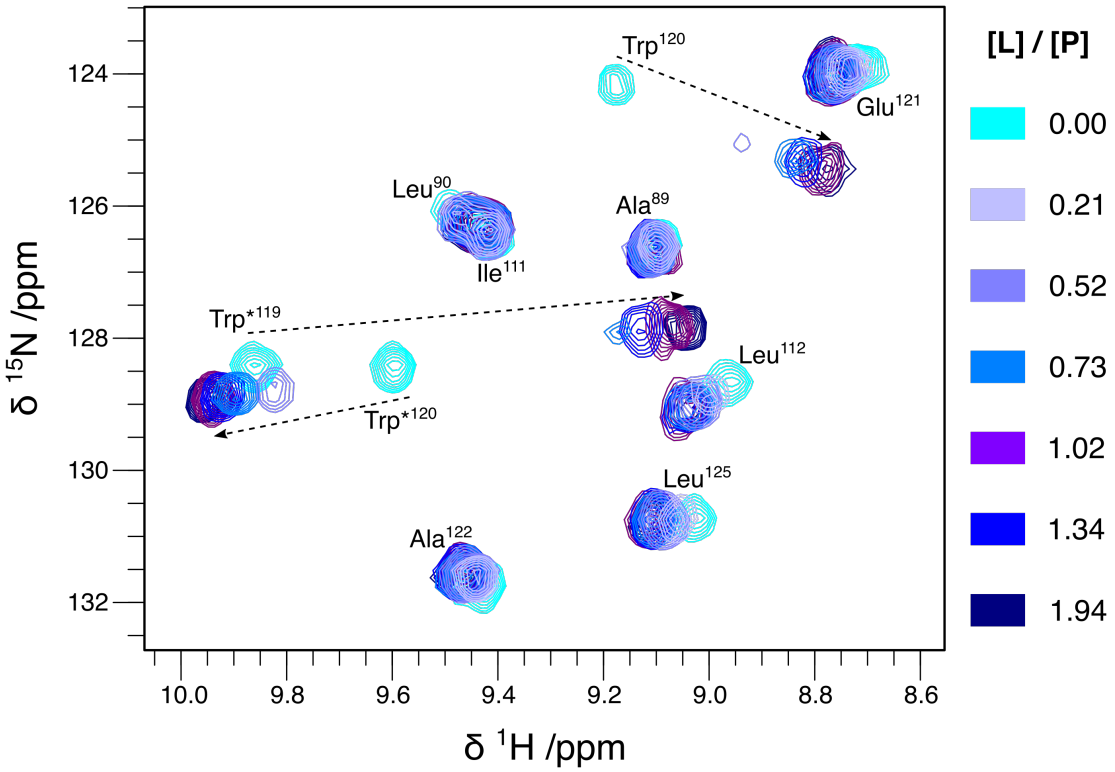

Figure 5.2: Overlay of the selected ^{1}H-^{15}N HSQC spectra of hFynSH3, obtained during the LoC-μNMR titration experiment with p85α$_{P91\text{-}T104}$. Colouring scheme is organised according to the increasing concentration of p85α$_{P91\text{-}T104}$ and explained on the right-hand side panel. Starred Trp* labels refer to signals originating from the sidechain indole amides rather than the backbone. Sample conditions: 2.8 mM hFynSH3, 0 - 5.0 mM p85α$_{P91\text{-}T104}$ in H_2O analysis buffer (2.5 μL); spectra recorded at 14.1 T with the homebuilt transmission line probe at room temperature.

of 73 resolved NH signals in the μNMR ^{1}H-^{15}N HSQC spectra, 14 have shown perturbations grater than $\sigma_{c,NH} = 0.23$ ppm, that was deemed significant[145]. Out of this group, 10 signals originate from the backbone amides, which map onto three separate patches between Arg^{96}-Asp^{100}, Gly^{117}-Trp^{120} and Tyr^{132}-Tyr^{137} on the hFynSH3 backbone, which coincides with the previously published data[114] and those presented in chapter 3. Two more CSPs in the ^{1}H-^{15}N HSQC spectra originate from the Hϵ/Nϵ of the Trp^{119} and Trp^{120} sidechain indoles, while the other two remain unassigned, however are known to originate from Hϵ/Nϵ of the same Asn or Gln residue. Based on the resolved hFynSH3 structure, Asn^{136} is considered a very likely candidate. Likewise, CSPs were also identified for the ^{1}H-^{13}C HSQC spectra covering the methyl region of hFynSH3, as visible in fig. 5.3. Those over $\sigma_{c,CH_3} = 53$ ppb were deemed significant and were identified on Ala^{95}, Thr^{97}, Ile^{111} and Ile^{133}, which covers 5 out of the total of 31 methyl groups on hFynSH3 and agrees with the titration data recorded using the conventional NMR setup, presented in chapter 3.

Isotope weighted ^{1}H/^{13}C and ^{1}H/^{15}N fractional shifts, $\theta = \Delta\delta_{comb}/\Delta\delta_{max}$, were fitted collectively and individually for each dataset to a two-state binding model to determine

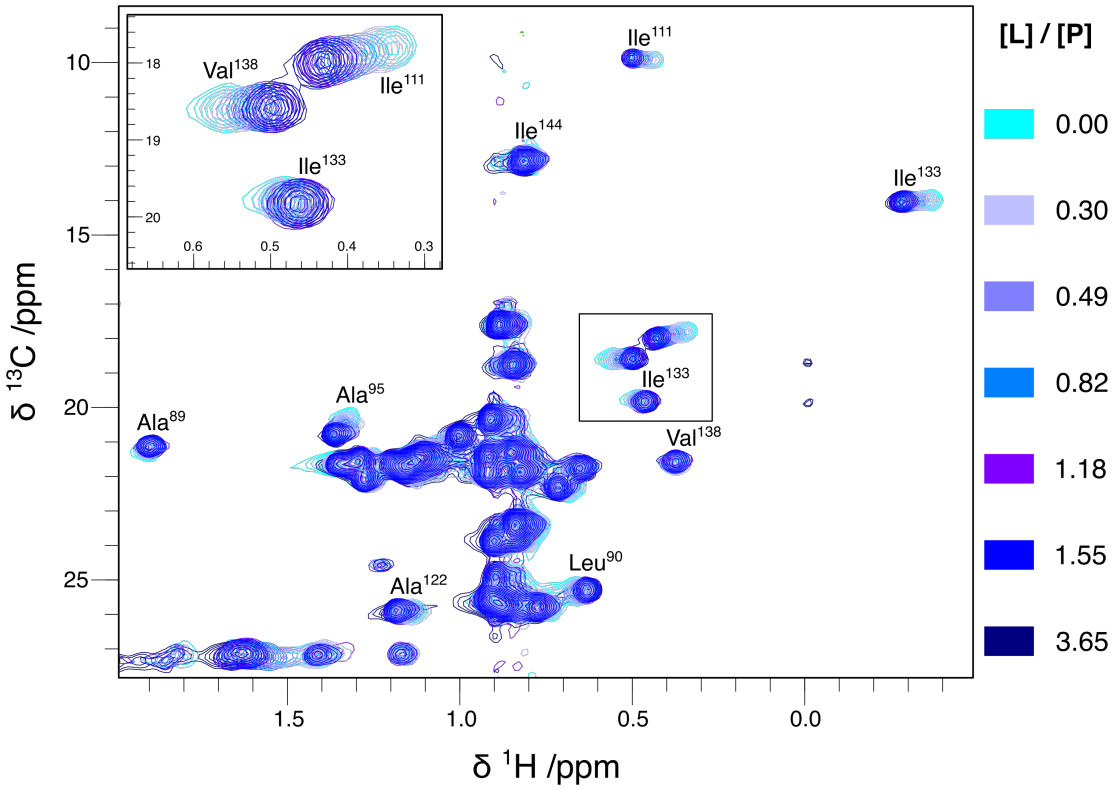

Figure 5.3: Overlay of selected ^{1}H-^{13}C HSQC spectra of hFynSH3, obtained during the LoC-μNMR titration experiment with p85α$_{P91\text{-}T104}$. Colouring scheme from light blue to navy corresponds to increasing concentration of the p85α$_{P91\text{-}T104}$ ligand, molar ratios are indicated on the right-hand side. Selection of the assigned methyl signals are shown. The insert in the top left corner represents the expansion that is boxed in the centre of the spectrum. Sample conditions: 2.1 mM hFynSH3, 0 - 6.0 mM p85α$_{P91\text{-}T104}$ in D_2O analysis buffer (2.5 μL); spectra recorded at 14.1 T with the homebuilt transmission line probe at room temperature.

the K_D for the hFynSH3 - p85α$_{P91\text{-}T104}$ binding equilibrium. Collectively, as presented in fig. 5.4, all heteronuclear NMR data has returned the K_D of 80 ± 12 μM, which is in good agreement with the 50 μM value[114] published previously. Individually fitted K_D values for the ^{1}H-^{13}C and ^{1}H-^{15}N HSQC datasets were 144 ± 29 μM and 30 ± 10 μM, respectively, however this representation fails the *F*-statistic (details in section 6.5.3) when compared to the collective fit. It is the conviction of the author that the discrepancy between the individually fitted K_D values is dictated by resolution, where considerably lower chemical shift span, $\Delta\delta_{max}$, in the ^{1}H-^{13}C HSQC spectra determines that the σ_{c,CH_3} for the CSPs is less than twice the resolution threshold, therefore limiting the precision of measurement. For the ^{1}H-^{15}N HSQC, the corresponding $\sigma_{c,NH}$ is over four times the resolution threshold and the data return the K_D closely resembling the previously published values[114,131]. Importantly, all previous NMR-based K_D evaluations were derived from the CSPs of the hFynSH3 amide resonances, while the characterisation of p85α$_{P91\text{-}T104}$ ligand binding based on protein methyl groups have not been carried out for hFynSH3 before.

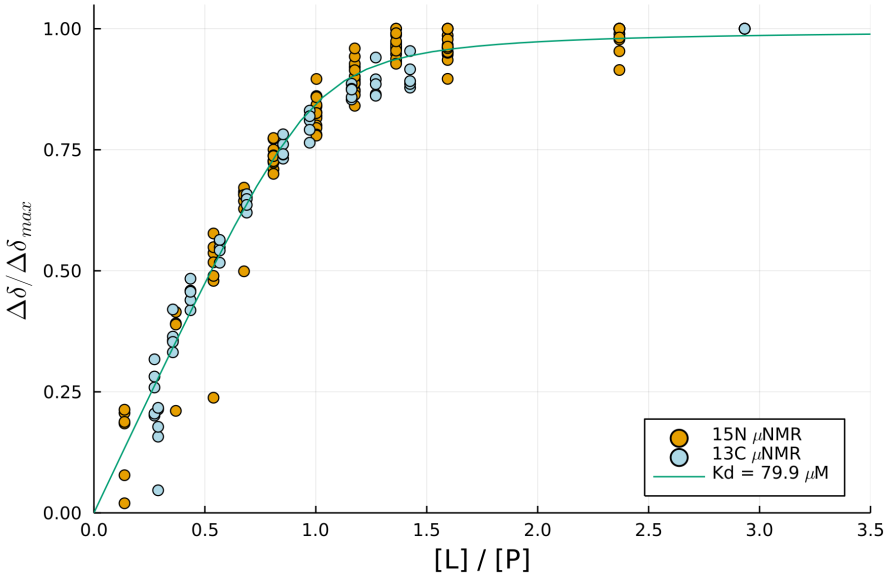

Figure 5.4: Binding isotherm for all significant CSPs detected in the μNMR titration. Data from both ^{1}H-^{13}C and ^{1}H-^{15}N HSQC spectra were fitted collectively returning a common K_D of $\sim$ 80 μM.

5.4 Relevance of the μNMR titration results

Apparent discrepancies in the K_D measurements for the hFynSH3 - p85α$_{P91\text{-}T104}$ model system presented above need to be considered with respect to the physical behaviour of biomolecules in solution. As result of this work it became clear that hFynSH3, while maintaining good solubility, at concentrations above $\sim$ 0.2 mM is affected by self-aggregation. This phenomenon was not previously reported and is very likely to have an effect on the binding to the p85α$_{P91\text{-}T104}$ ligand.

Similar to the ligand induced CSPs, changes to the chemical shifts of individual signals were observed in the ^{1}H-^{15}N HSQC spectrum of hFynSH3 when recorded at increasing protein concentration. Figure 5.5 displays an overlay of a selected region of the ^{1}H-^{15}N HSQC spectrum of hFynSH3 at concentrations between 0.17 - 2.66 mM. In fig. 5.5, a clear CSP is observed for the Arg^{96} backbone NH peak and similar behaviour was observed for another 17 signals assigned in the ^{1}H-^{15}N HSQC spectrum of hFynSH3. The distribution of the aggregation-induced CSPs in the hFynSH3 structure is shown in fig. 5.6, while those above the cut-off threshold, $\sigma_{c,Agg}$, are listed in table A.6 in the appendix. In an analogous fashion to the ligand binding analysis, a potential aggregation surface and the aggregation dissociation constant, K_{Da}, was evaluated. Significant aggregation-induced CSPs were identified for Gly^{80}, Thr^{85} - Phe^{87}, Arg^{96} - Leu^{101}, Asn^{113} - Trp^{119}, including the Trp^{119} sidechain indole Hϵ/Nϵ signal. The two extended patches, Arg^{96} - Leu^{101} and Asn^{113} - Trp^{119}, are located on the n-Src and RT loops involved in ligand binding. Therefore, interference of aggregation of hFynSH3 with the

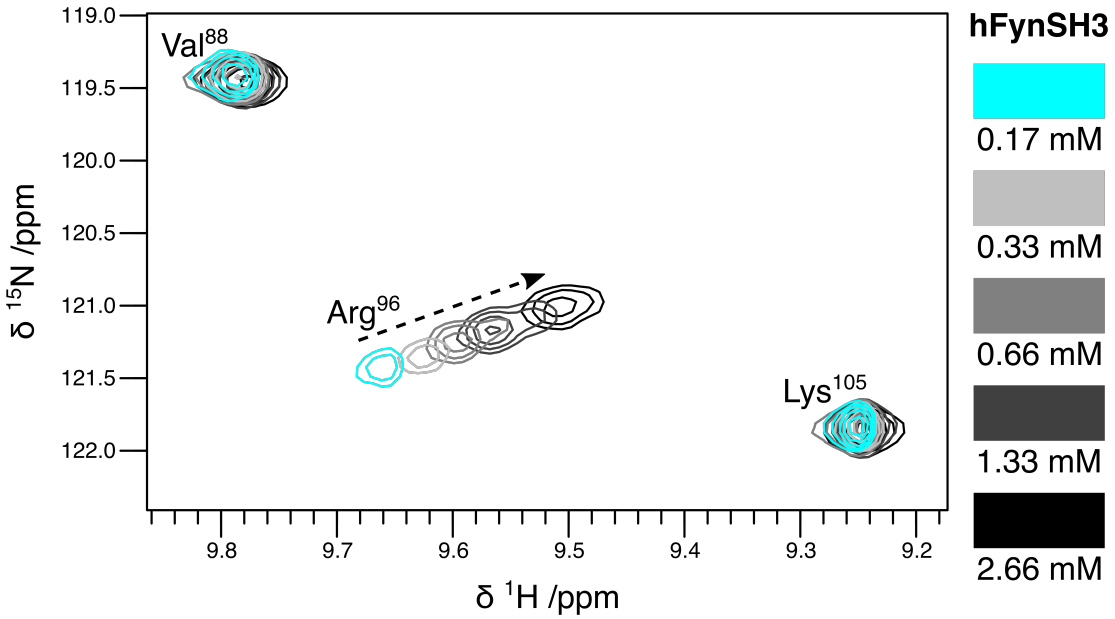

Figure 5.5: Overlay of a selected fragment of four ^{1}H-^{15}15 HSQC spectra of hFynSH3 at varying protein concentration. The arrow is pointing out the direction of the chemical shift change for the NH signal of Arg^{96} as a consequence of an increasing concentration of hFynSH3 from 0.18 to 2.8 mM. Sample conditions: 0.18 - 2.8 mM hFynSH3 in H_2O analysis buffer and 5% D_2O (15 μL); spectra recorded at 16.45 T with 1.7 mm TCI MicroCryoProbe^{TM} (Bruker, US) at room temperature.

binding to p85α$_{P91-T104}$ is highly likely. Furthermore, this provides reasoning as to why different K_D values were obtained based on the ^{1}H-^{15}N HSQC spectra at two different concentrations, 18 μM at 0.1 mM hFynSH3 for the conventional NMR titration, and 30 μM at 2.8 mM hFynSH3 for the automated μNMR. Likewise, Morton et al.[114] have reported the 50 μM K_D based on ^{1}H-^{15}N HSQC spectra recorded between 2 - 3 mM hFynSH3[114], while circular dichroism measurements at similar concentration have returned the K_D of 31 μM[131]. Given the characteristics of the system, it can be envisaged how minor changes to the buffer conditions, temperature or choice of significant CSPs could render a varying K_D value.

Based on the ^{1}H-^{15}N HSQC spectra recorded at 0.17 - 2.66 mM hFynSH3, and assuming the simplest aggregation (dimerisation) process, the K_{Da} was evaluated to be 6.4 ± 0.3 mM, therefore much weaker than the affinity towards p85α$_{P91-T104}$. A model considering potential aggregation and ligand binding states at the conditions of the automated μNMR titration experiments is proposed in fig. 5.7. Four distinct populations are considered: the monomeric hFynSH3, aggregate hFynSH3, and the monomeric and aggregate forms of the hFynSH3 - p85α$_{P91-T104}$ complex. In such a multiequilibrium system at least six possible interchange pathways can be contemplated (numbered in fig. 5.7), therefore a single dissociation constant is unlikely to provide a comprehensive representation of the system. In fact, abundance of competing equilibria can account for vastly differing K_D measurements, as observed for individual signals in the two

sets of μNMR experiments. Those are listed in tables A.4 and A.5 in the appendix. In summary, the author wishes to clarify this is a purely speculative model, nonetheless helpful to illustrate the elevated complexity of the system under investigation, and highlighting limitations of the available data to clarify it.

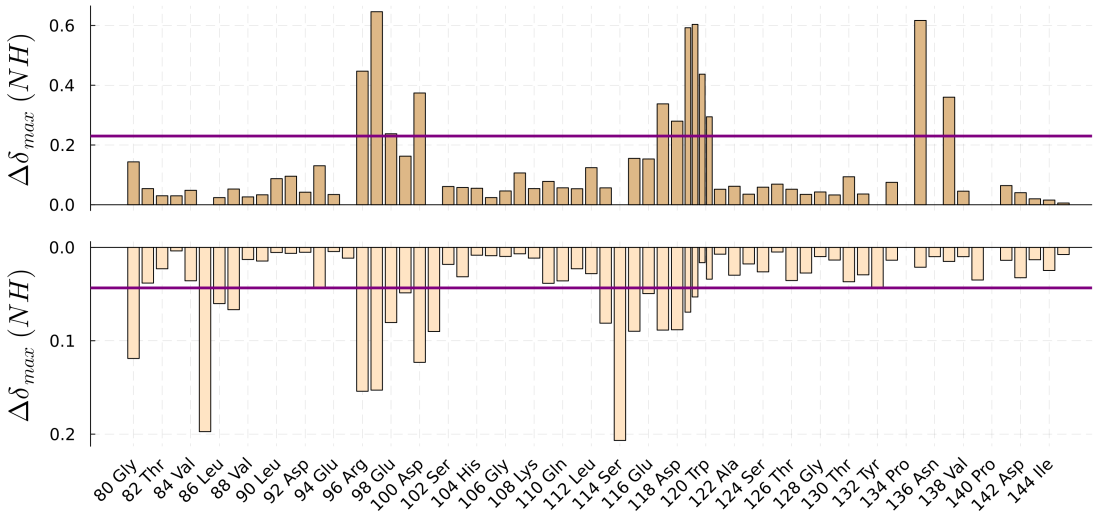

Figure 5.6: CSP distribution within the hFynSH3 backbone based on the μNMR ^{1}H-^{15}N HSQC data. Plotted are the $\Delta\delta_{max}$ values for each individual amide signal observed in response to titration with p85α$_{P91\text{-}T104}$ (top) and increasing hFynSH3 concentration between 0.17 - 2.66 mM (bottom). The horizontal lines represent the cut-off thresholds above which significant CSPs are qualified. For clarity, only altering residues are labelled on the x axis.

Using all recorded ^{1}H-^{15}N HSQC spectra of hFynSH3 an attempt was made to evaluate the effect of aggregation on the binding to the p85α$_{P91\text{-}T104}$ ligand. Figure 5.8 lists all the $\Delta\delta_{max}$ values obtained from the titration experiments carried out at 0.1 mM and 2.8 mM hFynSH3. On the top, the histogram displays the individual $\Delta\delta_{max}$ values with respect to the hFynSH3 sequence. The distribution of CSPs for the two conditions is maintained, however changes in the magnitude of corresponding signals can be observed, and are most pronounced between Arg^{96} and Ser^{102}. In the bottom panel in fig. 5.8 the $\Delta\delta_{max}$ values are plotted horizontally for 0.1 mM hFynSH3 and vertically for 2.8 mM hFynSH3. Colour coded are the NH signals whose $\Delta\delta_{max}$ is above (positive response, blue) or below (negative response, yellow) the cut-off threshold, $\sigma_{c,Agg}$, for the aggregation-induced CSPs. Following this selection mode, the K_D for each group was re-evaluated from the μNMR ^{1}H-^{15}N HSQC data. The resulting values were 22 μM and 109 μM, respectively. Oddly, this could suggest that aggregation-affected signals show an increased affinity towards the ligand. However, the more likely explanation is the fact that the majority (7 out of 12) of the assigned ligand-responsive signals, as well as those with largest $\Delta\delta_{max}$, are also present in the aggregation positive response group, hence the K_D is much tighter for this group. This is not surprising knowing that

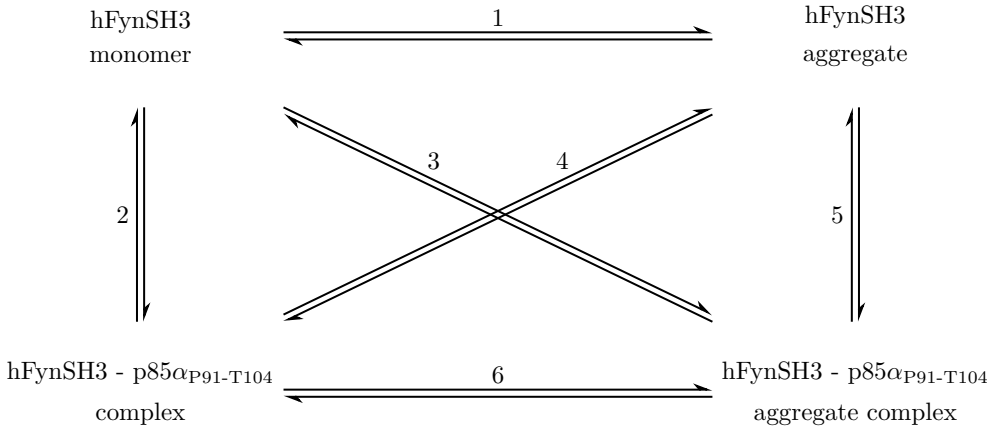

Figure 5.7: Diagram representing the possible states of the hFynSH3 - p85α$_{P91\text{-}T104}$ system at high hFynSH3 concentration. With four states available, six equilibrium constants (numbered) need to be taken into account.

the aggregation-affected peaks, as well as those involved in ligand binding, are mostly located on the n-Src and RT loops of hFynSH3.

5.5 Comparing the conventional and μNMR titration data

The binding of p85α$_{P91\text{-}T104}$ to hFynSH3, as reviewed in chapter 3, occurs in a 1:1 ratio, however the system analysed in the automated μNMR titration is notably more complex as result of the higher protein concentration. It is considered that the K_D value of 18 μM, obtained from the conventional NMR experiments at 0.1 mM hFynSH3, gives an accurate representation of the binding affinity towards the p85α$_{P91\text{-}T104}$ ligand in an unperturbed system. K_D values fitted for individual signals, as listed in tables A.2 and A.3, show minimal scatter around the mean with a standard deviation of 3.9 μM, indicating a single binding event. This is true for both the ^{1}H-^{15}N and ^{1}H-^{13}C HSQC datasets. Likewise, the ITC measurements carried out previously by Renzoni et al.[131] at the same hFynSH3 concentration has returned the K_D value of 16 μM, fully supporting our observation. For the system investigated at high hFynSH3 concentrations, the reported K_D is likely to include contributions from other equilibrium processes, such as those in fig. 5.7. It is possible that an accurate hFynSH3 - p85α$_{P91\text{-}T104}$ dissociation constant could be calculated based on the available data, however the appropriate model is yet to be formulated.

The aggregation-induced CSPs map onto the n-Src and RT loops of hFynSH3, however the only interference with a known element of the ligand binding pocket occurs at the indole amide of Trp^{119}. Furthermore, the correlation analysis presented in fig. 5.8 has failed to conclusively tie the aggregation affected signals to a specific outcome in terms of the dissociation constant. It is therefore proposed that the aggregation face

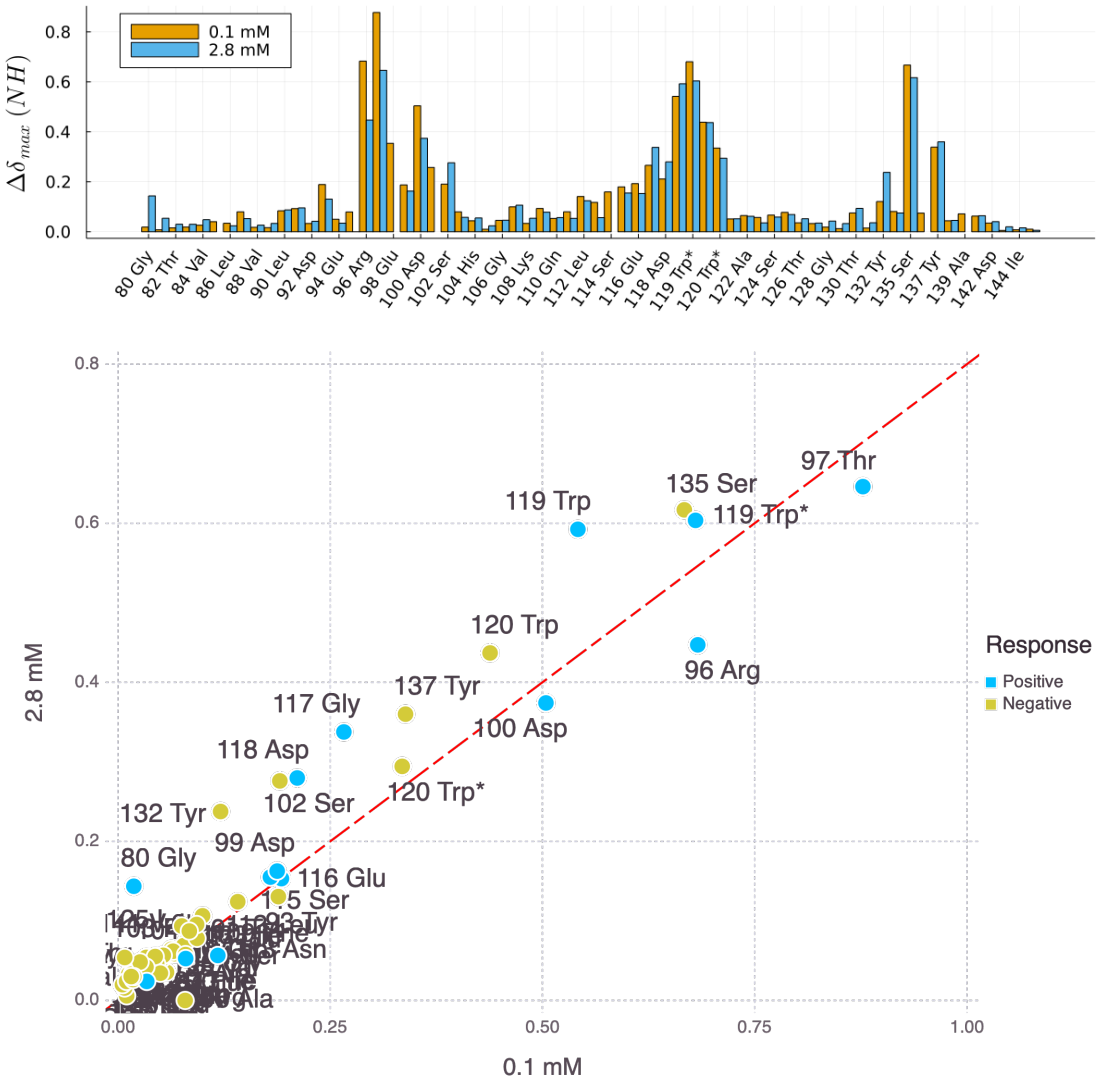

Figure 5.8: The ligand-induced $\Delta\delta_{max}$ values for the hFynSH3 amide signals, as reported at 0.1 mM and 2.8 mM protein concentration, in the conventional 500 μL sample and μNMR 2.5 μL, respectively. The histogram (top) gives the distribution of individual values with respect to the hFynSH3 sequence plotted on the x axis. The legend in the top left corner explains the histogram's colouring scheme. In the correlation plot (bottom) individual $\Delta\delta_{max}$ values at 0.1 mM hFynSH3 are plotted on the horizontal axis, against the same signals observed at 2.8 mM hFynSH3, plotted vertically. On the diagonal is plotted a theoretical line of maximum correlation between the data. Signals are labelled individually and colour coded according to their response to protein aggregation. Signals whose chemical shift changes significantly ($\Delta\delta_{max} \geqslant \sigma_{c,Agg}$) between 0.1 mM and 2.8 mM hFynSH3 are termed positive (blue) and the remaining signals are negative (yellow).

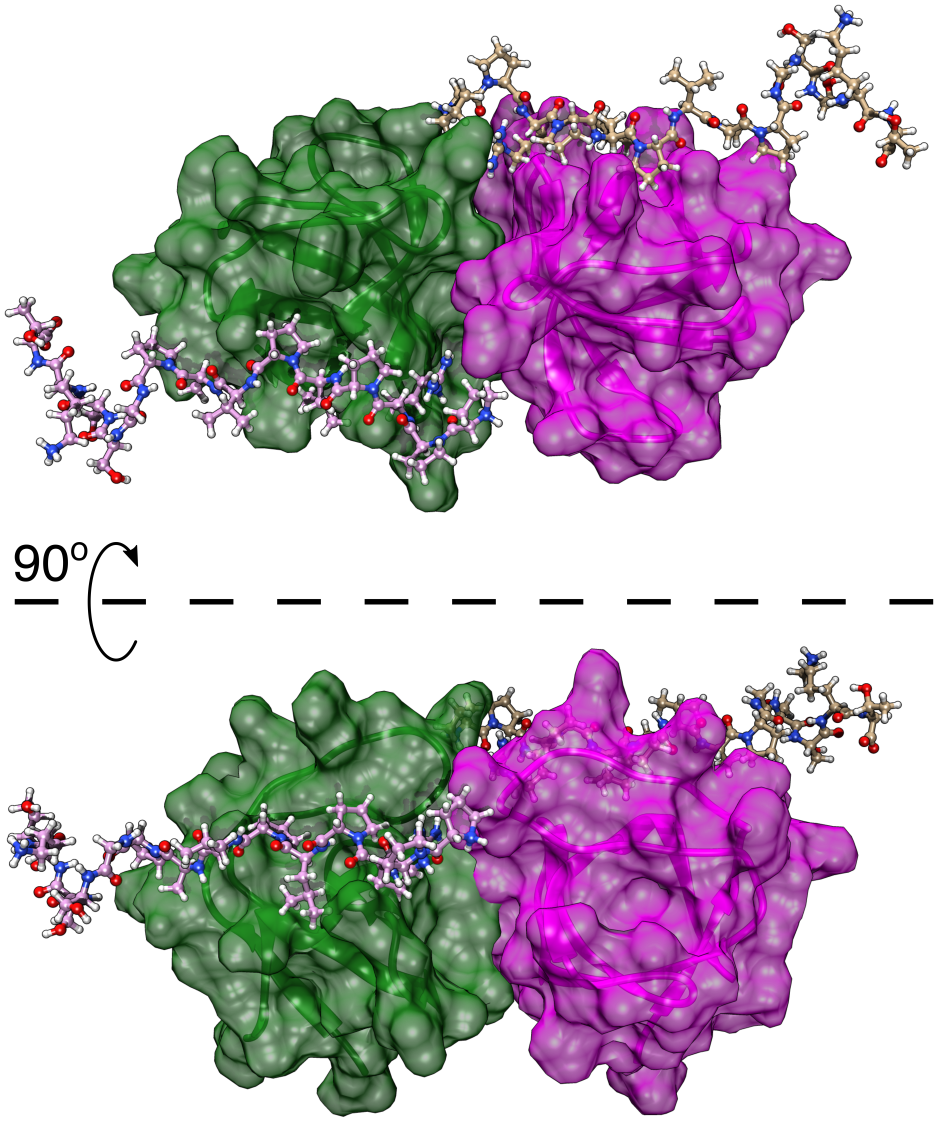

Figure 5.9: Postulated aggregation state for hFynSH3 at concentrations above 0.2 mM. Two hFynSH3 molecules are represented in green and purple with half-transparent surface. The p85α$_{P91\text{-}T104}$ ligand is shown in its binding orientation, in ball and stick representation using standard atom colouring. Structures are shown twice, with 90° rotation around the indicated (dashed line) axis. Figure generated using UCSF Chimera, based on the previously resolved hFynSH3 structure[131]; PDB entry: 1AZG.

on hFynSH3 is positioned perpendicular to the ligand binding surface and in the aggregated form the binding site for p85α$_{P91\text{-}T104}$ is not obscured, as presented in fig. 5.9. In such an arrangement the aggregated hFynSH3 forms a dimer, where the two units have a potential to rotate around the axis perpendicular to the aggregation surface. As the binding site is expected to remain accessible to the ligand, and the affinity towards p85α$_{P91\text{-}T104}$ is higher than that between two hFynSH3 molecules, it is possible for the ligand binding to be maintained in the dimeric form. Another possibility, even though the excess of hFynSH3 molecules are not expected to be in direct competition with

p85$\alpha_{\text{P91-T104}}$, is that in the dimeric form hFynSH3 offers a limited access to the ligand, therefore lowering the on rate, k_{on}, which is inversely proportional to K_D. Considering the above, there is a potential for cooperative binding of two p85$\alpha_{\text{P91-T104}}$ molecules to the same hFynSH3 dimer. In such case, one would need to consider what is the relative stability of the hFynSH3 - p85$\alpha_{\text{P91-T104}}$ dimer complex in comparison to its monomeric counterpart and what are the possible dissociation pathways. Again, all of these considerations are purely speculative, however demonstrate the level of complexity that needs to be resolved in order to fully represent the system.

5.6 Sample use

For the automated μNMR titration experiments in each case only 40 uL of the protein sample was used at 2.1 or 2.8 mM concentration. This accounts for 43 or 61 μg of isotope-labelled hFynSH3 in the 2.5 μL detection volume at each step of the experiment and 0.69 or 1.17 mg of protein in total. This is compared to 0.47 mg needed to prepare a single $\sim$ 500 μL sample at 0.1 mM protein for the conventional NMR approach, of which two were used to complete the titration. This gives the overall protein requirement of 0.95 mg for analogous experiments using the state-of-the-art Prodigy TCI CryoProbe (Bruker, US). Looking at the characteristics of the microfluidic device it is obvious that the gross volume of the sample fills the mixing circuit, rather than the 2.5 μL volume of the detection chamber. Contemporary microfluidic fabrication methods have the capacity to produce devices with much higher precision than what is available at the Utz lab, therefore devices with significantly lower dead volumes could be fabricated based on the same design, further limiting the sample use. It is the absolute conviction of the author that an optimised system would be able to execute the full titration experiment with a total sample volume equal to only twice the volume of the mixing circuit (V_s), i.e. no more than 20 μL overall.

5.7 Data quality

The heteronuclear HSQC spectra obtained for the automated μNMR titrations were qualitatively compared to equivalent experiments acquired using the state-of-the-art miniaturised detector 1.7 mm TCI MicroCryoProbe^{TM} (Bruker, US). Of the upmost concern were the critical aspects of sensitivity and resolution discussed in section 2.2, dictated by signal-to-noise ratio, SNR, and peak linewidth, $\Delta\omega_{1/2}$. The SNR was evaluated from the ^{1}H projection of the first t_1 transient in the HSQC spectrum, while the linewidth was measured for the equivalent 2D peaks in the full HSQC spectrum according to eq. (3.3). Between different data the acquisition time and processing parameters

were kept equal. The evaluated characteristics are listed in tables 5.1 and 5.2. As anticipated, the performance of the TCI probe is noticeably higher, especially in terms of signal-to-noise, however the $nLOD_f^m$ measure (explained in section 2.2) confirms the excellent mass sensitivity profile of the TLP. Sensitivity is related to spectral resolution according to eq. (2.27), where again the TCI probe has a better performance. For the TLP, the improved linewidth for the ^{1}H-^{13}C HSQC experiments is associated with favourable relaxation properties of the methyl groups. This comparison is not intended to downplay the performance of the system at hand, rather illustrate the benefits to be achieved by joining the current-state NMR hardware with microfluidic operation, demonstrated by this work.

	TLP	**TCI**
SNR	2.6	27.7
$nLOD_f^m$ /nmol Hz$^{1/2}$	18.9	10.1

Table 5.1: Critical sensitivity parameters for the homebuilt transmission line probe (TLP) and state-of-the-art miniaturised detector 1.7 mm TCI MicroCryoProbe^{TM} (Bruker, US).

	TLP		TCI
Spectra	^{1}H-^{15}N HSQC	^{1}H-^{13}C HSQC	^{1}H-^{15}N HSQC
Linewidth	49.7 Hz / 83 ppb	32.8 Hz / 55 ppb	14.7 Hz / 2 ppb
Resolution (ε)	30.8 Hz / 51 ppb	20.3 Hz / 34 ppb	2.8 Hz / 4 ppb

Table 5.2: Critical resolution parameters for heteronuclear experiments on hFynSH3 achieved for the transmission line probe (TLP), in comparison with the state-of-the-art miniaturised detector 1.7 mm TCI MicroCryoProbe^{TM} (Bruker, US). Data were acquired at 14.1 T (600 MHz) and 16.4 T (700 MHz) for the TLP and TCI, respectively.

5.8 Conclusions

This chapter summarises the main achievements of the 'Protein NMR on a Chip' project. The work described validates a system linking three unique functionalities in application to protein - ligand binding analysis. Those are: automated operation, minimised sample use and atomic-scale resolution. Two sets of titration experiments were carried out with acquisition of protein-detected heteronuclear NMR spectra. Both datasets allow to identify chemical shift changes of individual hFynSH3 protein signals in response to the binding of the p85α$_{P91\text{-}T104}$ peptide. To record individual spectra,

only 43 - 61 μg of isotope-labelled protein was needed and the entire experiment, including repeated injection, mixing and acquisition steps was carried out autonomously within $\sim$ 24 hours. This is the first demonstration of such experiments that the author is aware of and provides basis for improving the throughput of NMR for biomolecular characterisation.

Notable limitations need to be discussed, those are related to the platform's applicability towards biomolecular systems. Trying to minimise the volumetric sample use, the mass sensitivity requirements have dictated that sample concentration needed to be significantly increased. As it turns out, even the most robust proteins, such as hFynSH3, at 2 - 3 mM concentrations experience vastly different conditions than those at the physiological state. This is reflected by the differing K_D values obtained in the conventional and μNMR titration experiments, 18 $\pm$ 4 μM and 80 $\pm$ 12 μM, respectively. Fortunately, the design flexibility of the μNMR platform is such that practical solutions are readily available, and likely to overcome the experienced setbacks. Maintaining the mass sensitivity requirements, same quality spectra would be acquired with only $\sim$ 0.3 mM protein if the detection volume was to be increased to $\sim$ 25 μL. Thanks to the flexible design of the microfluidic chip, such adjustments can be easily implemented.

Further applications can be envisaged for studying multi-ligand equilibria, fragment screening or evaluation of protein dynamics, e.g. in response to changing buffer conditions. In line with miniaturisation efforts available for molecular biology, elements such as cell-free protein expression and selective labelling could be connected with μNMR to common pipeline workflows. Here, it is worth to mention the inherent non-invasive nature of NMR, making it perfectly suitable to work in conjunction with other analytical tools. Current advancements within the field, e.g. hyperpolarisation efforts, offer significant sensitivity improvements. Implementation of those in a μNMR setup would bring even more unique capabilities to the molecular biology toolkit.

Chapter 6

Materials & methods

6.1 The LoC device

6.1.1 Device design, fabrication and assembly

The production of all microfluidic chips was carried out on-site in the Utz lab. Each chip consists of a central 500 μm thick PMMA layer that is sandwiched between two outer 200 μm thick layers. The design features of the PMMA layers are specified in a AutoCAD (Autodesk, US) file and cut from commercially available PMMA sheets using CO_2 laser cutter (HPC Laser Ltd., UK). Adjusting the power and speed of the laser provides control over the depth and width of the cut. Microfluidic channels in the chip are produced to an approximate width and depth of 150 μm, while the detection chamber and valve elements are fully cut-through. Such prepared layers are washed with isopropanol, when dry treated with O_2 plasma (Diener, CH), and bonded with plasticiser (2.5 % v/v dibutyl phalate in isopropyl alcohol) under heat and pressure, according to a previously established protocol[186]. The device assembly is completed with three elastomer membranes, two 200 μm thick PDMS, and a single 100 μm thick nitrile rubber (NBR), and two holder blocks that cover the the upper part of the microfluidic chip. Like PMMA layers, the elastomer membranes are cut from the respective sheets with the CO_2 laser. The chip holder is custom designed in SolidWorks (3DS, FR) and produced from Accura® Xtreme™ 200 Plastic by SL 3D-printing (Protolabs, UK). The specific chip designed for this project contains five microvalves (see fig. 4.5) consistent with the plunger architecture fist demonstrated by Baek *et al*[11]. The holder contains the necessary liquid and gas channels and microports, to connect the device to external pressure and liquid supply systems. Assembled device is held together by four M3 screws. Figure 4.2 A shows the chip design, while fig. 4.3 demonstrates how the microfluidic device is assembled from all components. A picture of the non-standard hardware and the microfluidic device is included in fig. 6.1.

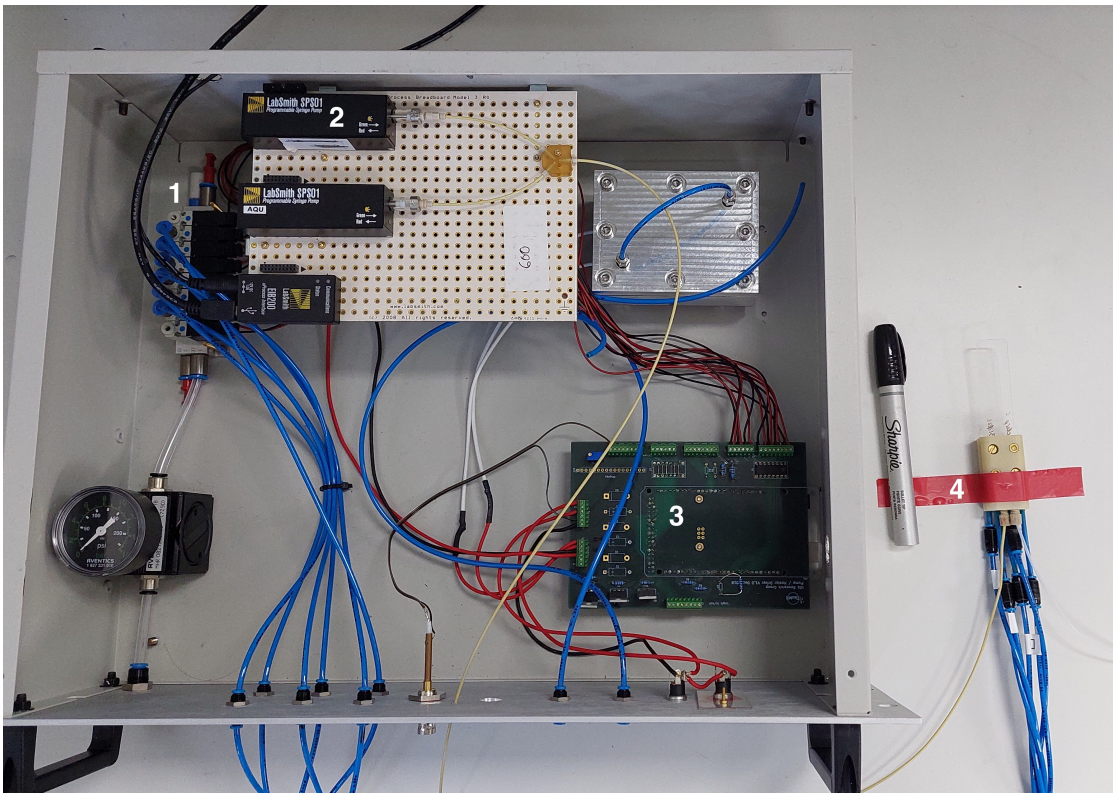

Figure 6.1: Photograph of the developed LoC-μNMR system. Numbered are solenoid valves (1), micro-syringe pump (2), Arduino Mega 2560 board (3) and the assembled device (4), including the microfluidic chip, chip holders and the connecting pressure and liquid leads.

6.1.2 Sample loading

A 80 μm ID Polyethylene ether ketone (PEEK) capillary connects the microfluidic device to the SPS01 micro-syringe stepper-motor pump (LabSmith, US). To start with, the volume of the syringe and connecting capillary is filled with perfluorinated oil (Fluoinert^{TM} FC-43; Sigma-Aldrich, UK). Sample is loaded into the capillary from a length-modified pressure resistant NMR tube (Wilmad-LabGlass, US) serving as the initial reservoir. The loading end of the capillary is immersed in the sample liquid and $\sim$ 3 bar of pressure is supplied to the NMR tube. Action of the micro-syringe at the other end of the capillary controls the volume drawn into the capillary loading end. The same procedure is repeated to load the second sample solution. Subsequently, the loading end of the capillary is connected to the assembled microfluidic device and 1.5 - 3 bar air pressure is applied to the device outlet. The microfluidic chip is filled with the sample liquid by the micro-syringe action.

6.1.3 Microvalve control

The microvalves on the chip are actuated via approximately 4 m leads operating at 5 bar air pressure. Using a common manifold, a single pressure input is separated into six leads that extend to the individual microvalves. The manifold holds six solenoid valves (Festo, DE), controlled by the Arduino Mega 2560 (Arduino, US) board. The board regulates the transmission of pressurised air from the manifold to the individual leads and microvalves.

6.1.4 Software

Firmware controlling the solenoid valves was written in Arduino IDE (Arduino, US) and allows for individual and sequential actuation of the valves with varying patterns and frequency. Micro-syringe is controlled with manufacturer supplied uProcess^{TM} software (LabSmith, US). Operation of both systems was interfaced into a common LabVIEW script which also triggers the NMR spectrometer for spectra acquisition, as detailed in fig. B.1.

6.2 Improved Transmission Line Probe

Initial feasibility for multidimensional NMR was proved using an existing modular TLP probe, described in detail by Sharma and Utz[150]. This probe uses a circuit in which the two detector planes are connected at the far end through a pair of capacitors. This design leads to a relatively low inductance of the detector assembly at low frequencies, which makes it difficult to tune and match the system to the ^{15}N frequency. As a result, the probe initially available was only tunable to ^{13}C. In a joint effort with Dr Manvendra Sharma a new variant of the probe, designed for efficient acquisition of ^{1}H-^{15}N HSQC spectra with optimal sensitivity, was constructed.

Efficient coupling to the low Larmor frequency of ^{15}N at 14.7 T is facilitated by a high inductance of the detector coil. The two conductor planes that make up the transmission line detector were therefore directly connected at the top by replacing the capacitive connection with conducting blocks of copper, as shown in fig. 6.2. In addition, the tank circuit band reject filter of the original TLP design that insulates the ^{15}N channel from the ^{1}H frequency was replaced by a shorted $\lambda/4$ line, as shown in the figure. This probe was found to perform very well, with a RF efficiency of 26 and 82 $\mu T/\sqrt{W}$ for the ^{1}H and ^{15}N channels, yielding 90° pulse lengths of 3.2 μs and 10 μs, respectively.

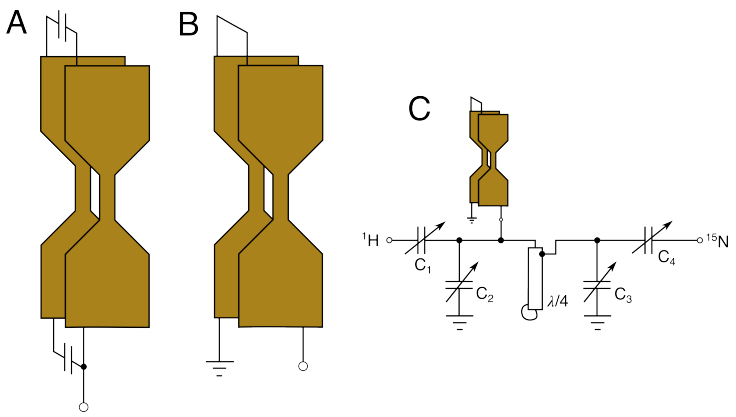

Figure 6.2: Schematics of the transmission line detector. Shown are the original transmission line resonator as described by Sharma and Utz[150] with capacitive coupling of the detector planes (A), improved detector with increased inductance due to direct coupling of the detector planes at the top (B) and circuit diagram of the improved ^{1}H-^{15}N double resonance probe (C).

6.3 Sample preparation

6.3.1 hFynSH3 protein expression and purification

All hFynSH3 protein samples were produced on site, through well-established *E. coli* recombinant protein expression system and further purification. The BL21-CodonPlus (DE3)-RIPL competent *E. coli* cells (Agilent, US) were heat-shock transformed with pGEX-2T-hFynSH3 plasmid containing the following DNA expression construct:

GSPHMTGTLRTRGGTGVTLFVALYDYEARTEDDLSFHKGEKFQILNSSEGD
WWEARSLTTGETGYIPSNYVAPVDSIQ.

The underlined sequence holds 100 % identity to human and murine Fyn-kinase SH3 domain. The full sequence shows 13 AA difference in comparison to the construct used to determine the hFynSH3 structure by NMR[114]. This includes a 16 AA insert at the N-term and 3 AA deletion at the C-term, neither of which alter the core hFynSH3 sequence (underlined).

As a construct of the pGEX-2T plasmid (GE Healthcare, US), the hFynSH3 was expressed in the *E. coli* host cells as a fusion protein with Glutathione S-transferase (GST). Expression was carried out in the Luria-Bertani broth (LB) for the unlabelled protein, and M9 minimal media with incorporation of ^{13}C glucose and/or $(^{15}NH_4)_2SO_4$, depending on the labelling requirements for heteronuclear NMR experiments. All growth media were made to contain 100 μg/mL Ampicillin and 34 μg/mL Chloramphenicol to select for only the transformed *E. coli*, which acquired antibiotic resistance. *E. coli* cultures were first grown at 37° C in 100 mL starter cultures. Optical density at 600 nm (OD_{600}) of each culture was checked regularly. At $OD_{600} \sim 0.7$ cultures were transferred

into overall 500 mL and allowed to grow again until $OD_{600} \sim 0.7$, before induction with 0.25 mM Isopropyl β-D-1-thiogalactopyranoside (IPTG). After induction cultures were grown at 30°C for 18 hrs, then harvested by centrifugation (5400 g, 20 min, 4°C) and stored at -20°C.

In the purification process cell paste was thawed and resuspended in lysis buffer: 75 mM Tris-HCl pH 8, 200 mM NaCl, 5 mM β-mercaptoethanol, 0.1 % v/v Triton X-100, 2 mM Ethylenediaminetetraacetic Acid (EDTA), cOmplete^{TM} mini (Roche, CH) protease inhibitor. Suspension was sonicated (6 * 20 s) at 0° C for cell lysis. Subsequently, cell debris was collected by centrifugation (17000 g, 50 min, 4°C) and discarded. Supernatant was passed through a column of Glutathione-Sepharose 4B beads (GE Healthcare, US) in resin buffer (20 mM Tris-HCl pH 8, 150 mM NaCl, 2.5 β-mercaptoethanol) to retain the GST-hFynSH3 fusion protein. Column was extensively washed with resin buffer and Phosphate Buffered Saline (PBS) pH 7.4 before incubation at room temperature with Thrombin protease (1 U per 100 μg of target protein) to cleave off the target hFynSH3 protein from the GST tag. After 16 - 18 hrs the protease activity was arrested by introduction of 1 mM Phenylmethylsulfonyl Fluoride (PMSF). The column flow-through was collected and the column was washed extensively with PBS and 10 mM Glutathione (GSH) in PBS to remove the bound GST. Fractions containing the hFynSH3 protein were concentrated using the 3 MWCO Vivaspin 20 (Sartorius, DE) centrifugal concentrators and applied to the HiLoad 16/600 Superdex 75 column (GE Healthcare, US) under PBS for size exclusion chromatography. Eluted hFynSH3 fractions were pooled and concentrated with buffer exchange for the analysis buffer (20 mM KH_2PO_4/K_2HPO_4 pH 6 containing 0.02% NaN_3 in H_2O or D_2O).

6.3.2 The p85$\alpha_{\text{P91-T104}}$ peptide

Synthetic peptide was obtained as > 70 % purity lyophilised powder from the supplier (ChinaPeptides, CN). Samples for analysis by NMR were prepared by dissolving the powder in 1 mL of H_2O and twice dialysing in a 1/1000 volume ratio using the 0.5 MWCO Float-A-Lyzer^{TM} G2 device (Repligen, US). Following dialysis, the 1 mL sample was lyophilised for storage and dissolved in a designated volume of the analysis buffer in preparation for the NMR experiments.

6.3.3 Titration samples

For the accurate evaluation of the K_D values, concentrations of the involved species, namely hFynSH3 and p85$\alpha_{\text{P91-T104}}$ needed to be measured precisely. Following the expression and purification protocols, described in section 6.3.1, hFynSH3 concentrations were evaluated based on the light absorbance measurements at 280 nm, A_{280}, from a 1-2 μL sample, acquired using the NanoDrop 2000/2000c instrument (ThermoFisher,

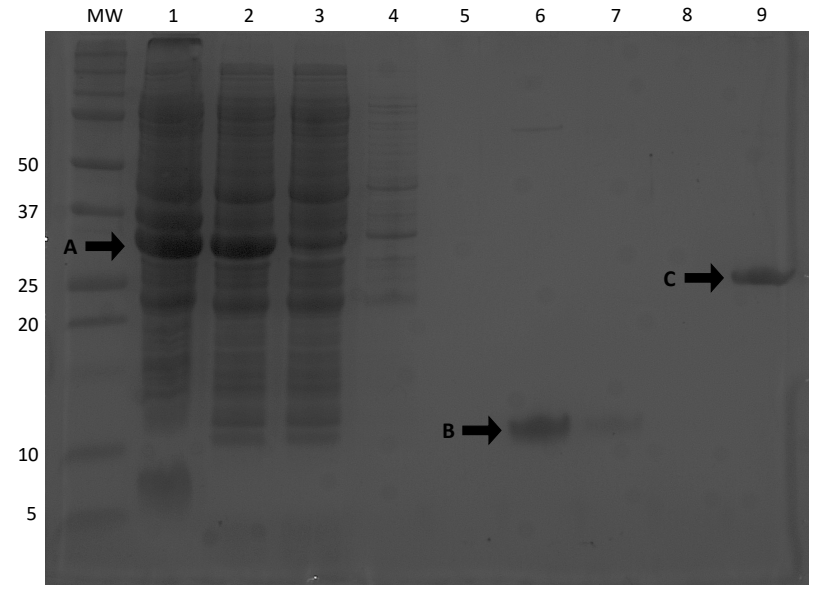

Figure 6.3: SDS-PAGE of samples from the purification process for hFynSH3. Lanes are protein marker (MW), cell lysate (1), centrifugation supernatant (2), flow-through after binding with GSH-Sepharose (3), resin buffer wash (4), PBS wash (5), flow-through after thrombin cleavage (6), PBS wash (7-8) and GSH elution (9). Arrows indicate the GST-hFynSH3 fusion protein (A), free hFynSH3 (B) and free GST (C). Protein marker weights (kDa) listed on the left, marker: Precision Plus Protein^{TM} Standards (Bio-Rad, US).

US). Absorbance measurements were converted into concentration values based on the Beer-Lamber law:

$$A_{280} = \epsilon \, l \, c, \tag{6.1}$$

where ϵ, l, c relate to the molar extinction coefficient, optical path length and concentration values, respectively. The ϵ is an intrinsic property of given species, in the case of protein A_{280} it is almost exclusively dependent on the number of aromatic residues, especially Trp, within the protein structure. For hFynSH3, the ϵ value was calculated using the PROTPARAM tool, available at the Swiss Bioinformatics Resource Portal (www.expasy.org), according to the known AA sequence. Due to the lack of optically active residues within the p85$\alpha_{\text{P91-T104}}$ sequence, ligand concentrations were evaluated based on ^{1}H NMR spectra in a solution of known concentration of TSP. Having assigned the methyl region of the ^{1}H spectrum for p85$\alpha_{\text{P91-T104}}$, the composite 0.93 ppm peak, with contributions from four methyl groups on Val and Leu residues, was compared with the 0 ppm signal for TSP. Concentration calculations were carried out according to:

$$f(I_x, I_a, n_x, n_a, [A]) = \frac{I_x}{I_a} \frac{n_a}{n_x} [A], \tag{6.2}$$

where I_x and I_a are the peak integral values for the analysed (p85$\alpha_{\text{P91-T104}}$) and reference (TSP) species, respectively. Likewise, n_a and n_x refer to the number of protons

contributing to each signal and $[A]$ is the known concentration of the reference compound. Individual titration samples were prepared by combining known volumes of the hFynSH3 solution with the p85$\alpha_{\text{P91-T104}}$ + TSP stock. Accurate description of each sample, taking into account the measurement and pipetting errors, is presented in table 6.1. Evaluation of the errors involved in sample preparation is explained in section 6.5.1.

	Conventional	**μNMR (^{15}NH)**	**μNMR ($^{13}CH_3$)**
Buffer, pH	20 mM K_2HPO_4/KH_2PO_4 in H_2O, pH 6		20mM K_2HPO_4/KH_2PO_4 in D_2O, pH 6
protein-only sample	100 μL * 0.53 $\pm$ 0.03 mM hFynSH3 + 450 μL buffer	95 μL * 4.43 $\pm$ 0.29 mM hFynSH3 + 55 μL buffer	70 μL * 2.44 $\pm$ 0.16 mM hFynSH3 + 20 μL buffer
protein-ligand sample	100 μL * 0.53 $\pm$ 0.03 mM hFynSH3 + 236 μL * 4.97 $\pm$ 0.4 mM p85$\alpha_{\text{P91-T104}}$ + 204 μL buffer	95 μL * 4.43 $\pm$ 0.29 mM hFynSH3 + 55 μL * 13.5 $\pm$ 1.6 mM p85a	70 μL * 2.44 $\pm$ 0.16 mM hFynSH3 + 20 μL * 27.2 $\pm$ 2.7 mM p85$\alpha_{\text{P91-T104}}$
[TSP] in the protein-only sample	10 $\pm$ 1 μM	200 $\pm$ 18 mM	165 $\pm$ 15 mM
hFynSH3 labelling	$^{13}C/^{15}N$	^{15}N	^{13}C
[hFynSH3]	97 $\pm$ 11 μM	2.8 $\pm$ 0.18 mM	2.1 $\pm$ 0.14 mM
[p85$\alpha_{\text{P91-T104}}$] /mM	2.13 $\pm$ 0.16	4.98 $\pm$ 0.4	6.0 $\pm$ 0.6
[L]/[P] range	0 - 26.6	0 - 2.0	0 - 3.4

Table 6.1: Individual composition of the samples prepared for the NMR titration experiments

6.3.4 Other chemicals

The solutions used for the calibration of the LoC-μNMR system, described in section 4.4.2, namely fumaric acid, 3-trimethylsilyl-1-propanesulfonate (DSS) and sodium acetate were prepared as following: 43.9 mg of DSS and 23.5 mg fumaric acid were dissolved in 4 mL of previously prepared 50 mM sodium acetate stock, each. In both samples the pH was adjusted to 13 $\pm$ 0.5 using the 50 mM sodium acetate + 1.5 M NaOH solution.

6.4 NMR data acquisition and processing

6.4.1 Assignment experiments

Protein samples were prepared as outlined above. The analysed sample was made to 0.65 mM $^{13}C/^{15}N$-labelled hFynSH3 with 5% D_2O in 300 μL SHIGEMI tube. All measurements were performed at room temperature using the Prodigy TCI CryoProbe at 16.45 T Ascend 700 NB magnet with AVANCE NEO console (all Bruker, US). Experiments for protein signal assignment discussed in chapter 3 were carried out as implemented in the Bruker TopSpin® software.

6.4.2 hFynSH3 - p85$\alpha_{\mathbf{P91\text{-}T104}}$ titration

6.4.2.1 Conventional NMR experiments

Two primary 550 μL titration samples were prepared to contain 0.1 mM $^{13}C/^{15}N$-labelled hFynSH3, one with excess (2.1 mM) of the p85$\alpha_{\text{P91-T104}}$ peptide, as detailed in table 6.1. Titration was carried out by repeated pipetting of known volumes between the two samples. As consequence the following ligand-to-protein ratios were generated: 0.0, 0.1, 0.2, 0.4, 0.6, 0.8, 1.0, 2.5, 4.6, 11.3 and 22.0. All measurements were performed at room temperature using the nitrogen-cooled Prodigy TCI CryoProbe at 16.45 T Ascend 700 NB magnet with AVANCE NEO console (all Bruker, US). Following experiments were carried out: $^{1}H/^{15}N$-[113] and $^{1}H/^{13}C$-HSQC[166] with application of PFGs for coherence selection as implemented in the Bruker TopSpin® software. The FIDs were processed with zero-filling and sine-bell apodization using the NMRPipe Spectral Processing Software[28].

6.4.2.2 LoC-μNMR

Two separate experiments were carried out with ^{13}C- and ^{15}N-labelled hFynSH3 protein. The sample preparation details are listed in table 6.1. In each experiment two samples were prepared containing only the hFynSH3 protein, and hFynSH3 with saturating concentration of the p85$\alpha_{\text{P91-T104}}$ peptide. Experiments were carried out according to the protocol outlined in section 4.3, while additional spectra were also acquired for the prepared solutions, separately. All measurements were performed at room temperature using the TLP at 14 T Bruker AS 600 WB magnet with a Bruker AVANCE NEO console. ^{1}H-^{13}C and ^{1}H-^{15}N HSQC[15] experiments were carried in double resonance mode limited by the TLP, with 32 step phase cycle needed for coherence selection. The FIDs were processed with zero-filling and sine-bell apodization using the NMRPipe Spectral Processing Software[28].

6.4.3 Calibration of the LoC-μNMR serial mixing modality

All NMR measurements were performed at 11.7 T Bruker Active Shield II WB magnet equipped with a Bruker AVANCE III console. Spectra, consisting of 8 transients each, were recorded with repetition delay of 8 s and 2 s acquisition time. Water signals were suppressed by 3 s of presaturation with a nutation frequency of 100 Hz. The FIDs were processed with 0.5 Hz of Lorentzian line broadening and automatic baseline correction. All processing was implemented using the NMR.jl (https://github.com/marcel-utz/NMR.jl) package for the Julia[14] programming language.

6.4.4 Aggregation of hFynSH3

Measurements were carried out on 15 μL aliquot samples obtained by serial dilution, starting from 2.8 mM ^{15}N-labelled hFynSH3, using the 1.7 mm TCI MicroCryoProbe^{TM} at 16.45 T Ascend 700 NB magnet with AVANCE III console (all Bruker, US). Special thanks go to Dr Christopher Williams (School of Cellular and Molecular Medicine) and Prof. Matthew Crump (School of Chemistry) at the university of Bristol for facilitating the acquisition of this data. The FIDs were processed with zero-filling and sine-bell apodization using the NMRPipe Spectral Processing Software[28].

6.5 NMR data analysis

6.5.1 Concentration calculations and propagation of errors

Based on eq. (6.2), the calculated concentration of p85$\alpha_{\text{P91-T104}}$ can be treated as a function of several variables, each with individually associated measurement error. The errors of each of the inputs are considered independent of the others, therefore covariance can be ignored. The integrated error to of estimated value, in this case [p85$\alpha_{\text{P91-T104}}$], can be calculated according to:

$$\Delta f = \sqrt{\left(\frac{\partial f}{\partial [A]}\right)^2 (\Delta[A])^2 + \left(\frac{\partial f}{\partial I_x}\right)^2 (\Delta I_x)^2 + \left(\frac{\partial f}{\partial I_a}\right)^2 (\Delta I_a)^2} \tag{6.3}$$

After solving the individual partial derivatives, and assuming ΔI_x and ΔI_a are equal and defined by the inherent noise of individual spectra, eq. (6.3) is rewritten as:

$$\Delta f = \frac{n_a}{n_x} \frac{\sqrt{{I_x}^2 (\Delta[A])^2 + [A]^2 \left(\Delta {I_x}^2 + {I_x}^2 / {I_a}^2\right)}}{I_a} \tag{6.4}$$

In the case of the p85$\alpha_{\text{P91-T104}}$ stock solution prepared for the conventional titration experiments n_a = 9, n_x = 12, $[A]$ = 10 uM, $\Delta[A]$ = 1.6 uM, ΔI is the RMSD of the noise,

therefore Δ[p85$\alpha_{\text{P91-T104}}$]=0.4 mM. Equivalent calculations were performed for all prepared samples as listed in table 6.1.

6.5.2 K_D calculations

K_D fitting was made in relation to eq. (3.5), which can be rewritten as:

$$[LP]^2 - [LP]([P] + [L] + K_D) + [P][L] = 0 \tag{6.5}$$

and therefore has a following solution:

$$[LP] = \frac{[P] + [L] + K_D \pm \sqrt{([P] + [L] + K_D)^2 - 4[P][L]}}{2} \tag{6.6}$$

As the fractional shifts of individual protein signals give a measure of the fraction bound of protein, eq. (6.6) can be adapted accordingly:

$$\theta = \frac{\Delta\delta_{comb.}}{\Delta\delta_{max}} = \frac{[LP]}{[P]} = \frac{[P] + [L] + K_D - \sqrt{([P] + [L] + K_D)^2 - 4[P][L]}}{2[P]} \tag{6.7}$$

or as:

$$\theta = 1/2 + \alpha + \beta_D - \sqrt{\alpha^2 + 2\alpha\beta_D + {\beta_D}^2 + 1/4 + \beta_D - \alpha} \tag{6.8}$$

where:

$$\alpha = \frac{[L]}{2[P]}$$
$$\beta_D = \frac{K_D}{2[P]}$$

In the course of this project four models were used for K_D fitting based on the CSP data. In model 1, calculated θ and the concentration values of hFynSH3 and p85$\alpha_{91\text{-}104}$ were the input variables to eq. (6.7), while K_D was the only free parameter. This model was employed for the conventional NMR dataset. For the μNMR results, the input variable was the measured intensity of the 0 ppm TSP peak, TSP_i, linearly related to α:

$$\alpha = m\ TSP_i + c \tag{6.9}$$

Measured concentration values for TSP, hFynSH3 and p85$\alpha_{\text{P91-T104}}$, as listed in table 6.1, were used to evaluate the initial guess values for m and c in relation to α:

$$\alpha = \left(\frac{TSP_i - TSP_{min}}{TSP_{max} - TSP_{min}} [L]_{max} \right) / 2[P] \tag{6.10}$$

where TSP_i corresponds to TSP peak integral value at each point of the titration experiment, $[L]_{max}$ is the concentration of p85$\alpha_{\text{P91-T104}}$ in the protein-ligand solution, TSP_{min}

and TSP_{max} are the integral values obtained for the protein-only and protein-ligand solutions, respectively. In model 2, calculated $\Delta\delta_{comb}$, concentration of hFynSH3 and α evaluated from TSP_i according to eq. (6.10) were the input variables while K_D and $\Delta\delta_{max}$ were the fitting parameters. Models 3 and 4 both used eq. (6.8), where the input variables were the calculated θ, TSP_i and measured concentration of hFynSH3, while m, c and K_D were the fitting parameters. Difference between models 3 and 4 relates to the treatment of K_D with respect to the heteronuclear μNMR datasets. In model 4 all data from the ^{1}H-^{13}C and ^{1}H-^{15}N HSQC spectra were collectively treated to fit a common K_D, while in model 3 individual K_D values were fitted to the corresponding ^{1}H-^{13}C and ^{1}H-^{15}N HSQC datasets. In all cases fitting was carried out using the Levenberg-Marquardt method, as implemented by the LsqFit package for the Julia programming language[14]. Detailed list of the fitting parameters is provided in table A.1.

6.5.3 The F statistic

To justify the choice of the best fit model to the CSP data calculations of the F statistic were made, comparing the variances between the alternative models. Individual variances, ${\sigma_n}^2$, are determined by:

$$ {\sigma_n}^2 = \frac{1}{df}\sum_{i=1}^{N}(y_i - \hat{y})^2 \tag{6.11} $$

where y_i are the individual input data, $\hat{y}$ are the modelled values and df defines the degrees of freedom for each model, calculated as the difference between the number of data points, N, and fit variables. The F statistic is subsequently calculated as:

$$ F = \frac{{\sigma_{1p}}^2}{{\sigma_{3p}}^2}\frac{n-3}{2}, \tag{6.12} $$

where ${\sigma_{1p}}^2$ and ${\sigma_{3p}}^2$ are the square residuals of the 1-parameter and the 3-parameter fits, respectively, and n is the number of fitted data points. This must be compared to the critical value $F^{0.05}_{n-3,n-1}$ for n data points and the rejection probability of 0.05. Results of the F statistic larger than the F critical were accepted as statistically significant grounds for choice of the best fit model. Individual ${\sigma_n}^2$ and F-values for the considered models are listed in table A.1.

Chapter 7

Conclusions

In this thesis efforts to combine microfluidic sample manipulation with NMR-based characterisation of protein-ligand interactions are described. The main advantages of this approach relate to the miniaturisation and automation offered by microfluidics, and label-free, non-invasive analysis by NMR at atomic resolution. The accomplishments of the 'Protein NMR on a Chip' project were achieved with pressure-driven microfluidic solutions and integrated operation of multiple hardware units. Three separate results sections are provided, relating to the study of the molecular model system by conventional state-of-the-art NMR, detailed description of the NMR-integrated microfluidics, and operation of the developed LoC-μNMR device in the context of protein-ligand interactions.

In chapter 3 the analytical power of NMR characterisation of protein-ligand interactions is presented, describing the model molecular system for this work: the hFynSH3 protein interacting with a short peptide fragment of the p85α subunit of the PI3-kinase, p85$\alpha_{\text{P91-T104}}$. Characterisation is based on heteronuclear NMR spectra, allowing to identify and assign signals originating from individual ^{1}H, ^{13}C and ^{15}N atoms within the hFynSH3 structure. Spectra recorded for the free-form hFynSH3 and hFynSH3 saturated with the p85$\alpha_{\text{P91-T104}}$ peptide are analysed to identify the structural changes induced by the ligand on the hFynSH3 protein, including the binding pocket. Separate round of experiments, where a set of two-dimensional HSQC spectra are recorded at an increasing molar ratio of ligand-to-protein are presented, based on which the ligand dissociation constant is obtained.

Chapter 4 describes the overall design of the microfluidic NMR system and its functionality in executing the automated serial mixing experiments coupled with *in operando* detection by NMR. The design involves multiple elements, including those necessary

for the fabrication and assembly of the device, ancillary hardware and software for remote and automated control over the experiment. The fundamental functionality of the device, i.e. the repeated mixing of two solutions within the common volume of the microfluidic chip was achieved by pneumatically actuated on-chip valves. Mixing capacity, the usual bottleneck in microfluidic systems is characterised qualitatively and quantitatively. Operation of this device *in situ* inside the NMR spectrometer is presented, where two solutions are gradually mixed in, demonstrating fine control over the concentrations of analysed solutions as a function of manipulated volume. This is the first implementation of such functionality at high magnetic field coupled with continual acquisition of NMR spectra that the author is aware of.

Finally, the applicability of the LoC-μNMR platform for protein study is demonstrated for the hFynSH3 - p85$\alpha_{\text{P91-T104}}$ molecular model system. Two sets of fully automated titration experiments are documented, where an increasing ligand-to-protein molar ratio is generated and integrated with acquisition of heteronuclear NMR spectra. In each case, much limited sample volume was used in comparison to the conventional NMR approach. The resulting data are analysed in the structural and thermodynamic context, by identification of the ligand-responsive atoms and evaluation of the dissociation constant of the protein-ligand complex. Acquired spectra are compared in terms of sensitivity and resolution to those recorded using the commercially available state-of-the-art miniaturised detector probe.

These results demonstrate that implementation of microfluidic operation to protein analysis by NMR can be successfully achieved and the function of either part need not be detrimental to the other. Likewise, based on the design flexibility and rapid prototyping capabilities further applications for this device can be considered, such as fragment screening, protein-protein interactions or studying multi-ligand equilibria. Despite the great advances demonstrated in this work, certain constraints were also reached. Those relate mainly to the hardware limitations of the transmission line probe. The current design allows only for double resonance, i.e. either $^{1}H/^{13}C$ or $^{1}H/^{15}N$. As such, implementation of triple resonance experiments needed for assignment of protein spectra is outside of the scope of this probe. However, the modular probe design was specifically chosen to accommodate further hardware improvements. Such could include additional tunable channel or a gradient coil, allowing for noticeable reduction of experimental time with coherence selection by PFGs or implementation of SOFAST HMQC experiments. Combined with the miniaturisation and automation offered by microfluidics this could open the avenue for high-throughput experimentation, which so far was beyond of the capabilities of NMR.

Appendix A

Supplementary results

A.1 Details of K_D fitting

	Conv.	μ**NMR (NH)**				μ**NMR (CH_3)**			
K_D **model**	1	2	3		4		3		2
Fit parameters	K_D	K_D, $\Delta\delta_{max}$	m, c, K_D		m, c, K_D		m, c, K_D		K_D, $\Delta\delta_{max}$
m **(nominal)**			$6.6e^{-8}$				$6.0e^{-7}$		
c **(nominal)**			$-2.9e^{-2}$				$-3.1e^{-1}$		
m **(fit)**			$(6.7\pm0.3)e^{-8}$		$(8.7\pm0.1)e^{-8}$		$(5.5\pm0.1)e^{-7}$	$(6.0\pm0.2)e^{-7}$	
c **(fit)**			$(3.1\pm1.3)e^{-2}$		$-(2.8\pm0.7)e^{-2}$		$-(1.7\pm0.1)e^{-2}$	$-(2.0\pm0.2)e^{-2}$	
K_D **(fit)** /μ**M**	18 ± 4	31 ± 7	30 ± 10		80 ± 12		143 ± 29	98 ± 29	
${\sigma_n}^2$	0.026	0.60	0.27		0.38		0.13	0.81	
F**-value**		2.17 (F critical = 1.38)						6.22 (F critical = 1.54)	
			1.06 (F critical = 1.22)						

Table A.1: List of K_D fitting parameters with respect to the considered models. Fitting parameters are listed for each model however the $\Delta\delta_{max}$ values are omitted as those were evaluated individually for each CSP signal. The final rows (${\sigma_n}^2$ and the F-value) refer to the F statistic parameters discussed in section 6.5.3. Joined rows give the F-value for the compared models, in the brackets the F critical is quoted, which signifies the cut-off above which the null hypothesis can be rejected. In all cases the assumed rejection probability is 0.05.

A.2 Individual K_D values

Residue	K_D / μM	Error / μM
Tyr^{93}	19.86	2.11
Arg^{96}	20.65	4.94
Thr^{97}	18.48	0.65
Glu^{98}	17.85	1.66
Asp^{99}	16.52	2.72
Asp^{100}	19.17	7.08
Leu^{101}	17.36	1.26
Ser^{102}	18.47	1.80
Leu^{112}	12.77	0.86
Ser^{114}	24.24	2.60
Ser^{115}	19.09	1.63
Glu^{116}	15.51	1.29
Gly^{117}	16.62	1.45
Asp^{118}	12.38	1.15
Trp^{119}	16.20	2.49
Trp^{*119}	16.13	0.57
Trp^{120}	15.79	1.66
Trp^{*120}	18.50	1.68
Ser^{135}	17.30	3.35
Tyr^{137}	16.38	1.20
$Asn/Gln^{!aa!}$	18.16	1.91
$Asn/Gln^{!ab!}$	16.10	1.57
$Asn/Gln^{!ba!}$	16.25	3.42
$Asn/Gln^{!bb!}$	16.69	2.13

Table A.2: Calculated K_D values for individual signals from the ^{1}H-^{15}N HSQC spectra acquired by the conventional NMR approach, at 0.1 mM hFynSH3. Starred Trp* inputs refer to the signals originating from the indole amide signals rather than the backbone. Likewise, the Asn/Gln$^{!\ldots!}$ inputs are associated with sidechain amide signals of Asn or Gln, which remain unassigned.

Residue	Atoms	K_D / μM	Error / μM
Leu^{90}	Hγ/Cγ	6.72	2.60
Ala^{95}	Hβ/Cβ	18.44	2.77
Glu^{98}	Hα/Cα	17.11	2.14
Phe^{103}	Hα/Cα	28.4	5.81
Phe^{103}	Hβ/Cβ	24.16	6.48
Ile^{111}	Hδ/Cδ	26.10	4.96
Ile^{111}	Hγ/Cγ	15.83	2.32
Ser^{115}	Hβ/Cβ	24.21	3.18
Asp^{118}	Hβ/Cβ	15.64	1.83
Trp^{120}	Hα/Cα	16.83	3.72
Ser^{124}	Hα/Cα	18.88	2.98
Tyr^{132}	Hα/Cα	14.94	3.40
Ile^{133}	Hδ/Cδ	19.62	2.52
Asn^{136}	Hα/Cα	12.37	4.00
Val^{138}	Hγ/Cγ	16.98	2.36

Table A.3: Calculated K_D values for individual signals from the ^{1}H-^{15}C HSQC spectra acquired by the conventional NMR approach, at 0.1 mM hFynSH3.

Residue	K_D / μM	Error / μM
Arg^{96}	1.54	3.43
Thr^{97}	63.58	49.06
Asp^{100}	848.78	310.01
Gly^{117}	222.18	38.48
Asp^{118}	10.50	25.13
Trp^{119}	22.04	5.93
Trp^{*119}	54.01	44.20
Trp^{*119}	60.39	15.49
Tyr^{132}	21.83	62.03
Ser^{135}	48.63	12.41
Tyr^{137}	158.96	36.52

Table A.4: Calculated K_D values for individual signals from the ^{1}H-^{15}N HSQC spectra acquired during the automated μNMR titration, at 2.8 mM hFynSH3.

Residue	Atoms	K_D / μM	Error / μM
Ala^{95}	Hβ/Cβ	301.75	84.49
Thr^{97}	Hγ/Cγ	121.91	83.93
Ile^{111}	Hγ/Cγ	154.50	61.12
Ile^{111}	Hδ/Cδ	212.27	83.74
Ile^{133}	Hδ/Cδ	201.17	45.58

Table A.5: Calculated K_D values for individual signals from the ^{1}H-^{15}C HSQC spectra acquired during the automated μNMR titration, at 2.1 mM hFynSH3.

A.3 Individual K_{Da} values

Residue	K_D / mM	Error / mM
Gly^{80}	9.52	5.55
Thr^{85}	4.93	2.57
Leu^{85}	5.60	0.44
Phe^{87}	4.94	0.52
Arg^{96}	8.91	2.79
Thr^{97}	5.97	4.04
Glu^{98}	2.81	1.18
Asp^{99}	6.00	2.38
Asp^{100}	8.33	2.54
Leu^{101}	4.99	0.73
Asn^{113}	5.79	1.45
Ser^{114}	6.18	1.97
Ser^{115}	8.75	2.50
Glu^{116}	10.16	3.14
Glu^{117}	7.09	1.94
Asp^{118}	8.57	4.24
Trp^{119}	10.53	5.35
Trp^{*119}	5.98	2.61
$Asn/Gln^{!}$	4.68	3.11

Table A.6: Calculated K_{Da} values for all individual amide signals in the ^{1}H-^{15}N HSQC spectra showing significant CSPs in response to the concentration of hFynSH3.

Appendix B

Details on μNMR hardware & firmware

B.1 LoC-μNMR automation flowchart

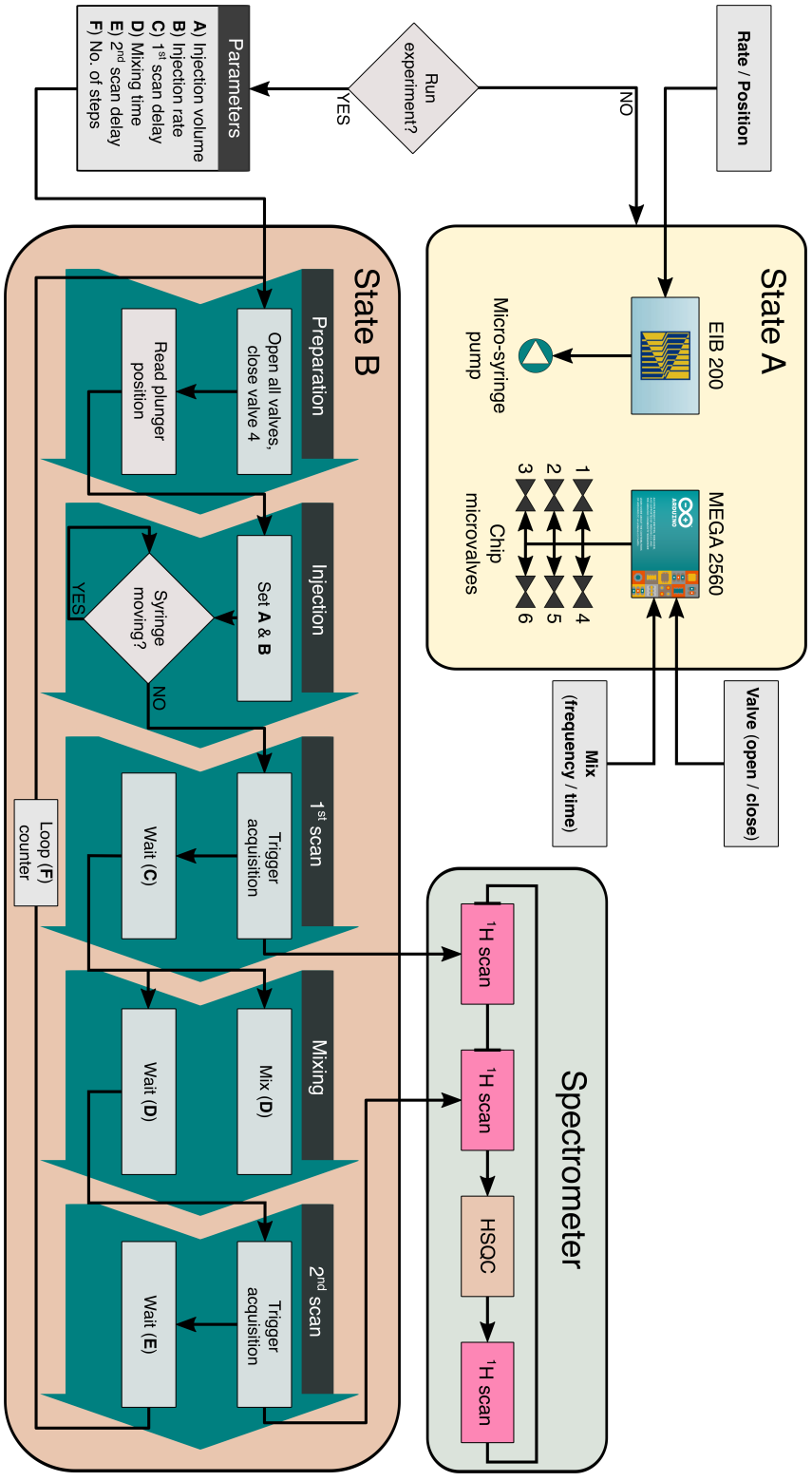

Figure B.1: Operation principle of the automated serial mixing experiment. Two operation states are programmed in the LabVIEW script that regulate the function of the three hardware components: EIB interface and micro-syringe pump (LabSmith, US), MEGA 2560 controller (Arduino, US), and the NMR spectrometer.

B.2 List of μNMR sensors

	Detector type	**Sample vol. /μl**	**Resolution /ppb**	**nLOD at 600MHz /nmol $s^{1/2}$**	**Reference**
a	Solenoid	0.005	2	0.13	Olson et al.[121]
b	Planar	0.03	300	20.9	Massin et al.[102]
c	Planar	0.47	300	262	
d	Solenoid	$4x10^{-8}$	1700	0.36	Ciobanu et al.[22]
e	Planar	0.393	12.4	13.8	Trumbull et al.[162]
f	Planar	0.57	100	163	Wensink et al.[170]
g	Stripline	0.012	80	18.3	family=Bentum et al.[38] and Kentgens et al.[75]
h	Planar	0.005	27	2.61	Ehrmann et al.[32]
i	Planar	0.00088	32	8.66	Stocker et al.[154]
j	Solenoid	$6.4x10^{-5}$	1700	16.5	Badilita et al.[9]
k	Phased array	0.77	11	7730	Gruschke et al.[57]
l	Planar	330	400	92 000	Renaud et al.[130]
m	Planar needle	0.5	50	12.3	Syms et al.[158]
n	Planar Helmholtz	10	20	125.6	Goloshevsky et al.[54]
o	Solenoid	0.03	2.33	141.1	Rogers et al.[133]
p	Solenoid	50	1000	30	Yamauchi et al.[183]
q	Planar	1.2	7.5	22	Ryan et al.[138]
r	Microslot	0.025	1.8	7	Maguire et al.[96]
s	Solenoid	0.0001	2600	0.1	Seeber et al.[148]
t	Microslot	0.0106	7.2	0.39	Krojanski et al.[80]
u	Planar Helmholtz	0.177	3.58	15.41	Spengler et al.[153]

Table B.1: Summary of μNMR detectors.

References

[1] A. Abragam. *The Principles of Nuclear Magnetism*. Clarendon Press. ISBN 978-0-19-852014-6.

[2] F.-T. Allain, Y.-M. Yen, J. Masse, P. Schultze, T. Dieckmann, R. Johnson, and J. Feigon. Solution structure of the HMG protein NHP6A and its interaction with DNA reveals the structural determinants for non-sequence-specific binding. 18 (9):2563–2579. ISSN 0261-4189. .

[3] I. D. Alves, S. M. Cowell, Z. Salamon, S. Devanathan, G. Tollin, and V. J. Hruby. Different Structural States of the Proteolipid Membrane Are Produced by Ligand Binding to the Human δ-Opioid Receptor as Shown by Plasmon-Waveguide Resonance Spectroscopy. 65(5):1248–1257. ISSN 0026-895X, 1521-0111. . URL http://molpharm.aspetjournals.org/content/65/5/1248.

[4] J. C. Andle and J. F. Vetelino. Acoustic wave biosensors. 44(3):167–176. ISSN 0924-4247. . URL https://www.sciencedirect.com/science/article/pii/0924424794008019.

[5] M. Arai, J. C. Ferreon, and P. E. Wright. Quantitative Analysis of Multisite Protein–Ligand Interactions by NMR: Binding of Intrinsically Disordered p53 Transactivation Subdomains with the TAZ2 Domain of CBP. 134(8):3792–3803. ISSN 0002-7863. . URL https://doi.org/10.1021/ja209936u.

[6] J. H. Ardenkjæ r Larsen, B. Fridlund, A. Gram, G. Hansson, L. Hansson, M. H. Lerche, R. Servin, M. Thaning, and K. Golman. Increase in signal-to-noise ratio of $>$ 10,000 times in liquid-state NMR. 100(18):10158–10163. . URL https://www.pnas.org/doi/10.1073/pnas.1733835100.

[7] W. E. Arter, A. Levin, G. Krainer, and T. P. J. Knowles. Microfluidic approaches for the analysis of protein–protein interactions in solution. 12(2):575–585. ISSN 1867-2450. . URL https://www.ncbi.nlm.nih.gov/pmc/articles/PMC7242286/.

[8] W. P. Aue, E. Bartholdi, and R. R. Ernst. Two-dimensional spectroscopy. Application to nuclear magnetic resonance. 64(5):2229–2246. ISSN 0021-9606. . URL https://aip.scitation.org/doi/10.1063/1.432450.

[9] V. Badilita, K. Kratt, N. Baxan, M. Mohmmadzadeh, T. Burger, H. Weber, p. u. family=Elverfeldt, given=Dominik, J. Hennig, J. G. Korvink, and U. Wallrabe. On-chip three dimensional microcoils for MRI at the microscale. 10(11): 1387–1390, . ISSN 1473-0189. . URL https://pubs.rsc.org/en/content/articlelanding/2010/lc/c000840k.

[10] V. Badilita, R. C. Meier, N. Spengler, U. Wallrabe, M. Utz, and J. G. Korvink. Microscale nuclear magnetic resonance: A tool for soft matter research. 8(41): 10583–10597, . ISSN 1744-6848. . URL https://pubs.rsc.org/en/content/articlelanding/2012/sm/c2sm26065d.

[11] J. Y. Baek, J. Y. Park, J. I. Ju, T. S. Lee, and S. H. Lee. A pneumatically controllable flexible and polymeric microfluidic valve fabricated viain situdevelopment. 15 (5):1015–1020. ISSN 0960-1317. . URL https://doi.org/10.1088%2F0960-1317%2F15%2F5%2F017.

[12] A. Bax and S. Grzesiek. Methodological advances in protein NMR. 26(4):131–138. ISSN 0001-4842. . URL https://doi.org/10.1021/ar00028a001.

[13] M. V. Berjanskii and D. S. Wishart. The RCI server: Rapid and accurate calculation of protein flexibility using chemical shifts. 35:W531–W537. ISSN 0305-1048. . URL https://doi.org/10.1093/nar/gkm328.

[14] J. Bezanson, A. Edelman, S. Karpinski, and V. B. Shah. Julia: A Fresh Approach to Numerical Computing. 59(1):65–98. ISSN 0036-1445, 1095-7200. . URL https://epubs.siam.org/doi/10.1137/141000671.

[15] G. Bodenhausen and D. J. Ruben. Natural abundance nitrogen-15 NMR by enhanced heteronuclear spectroscopy. 69(1):185–189. ISSN 0009-2614. . URL http://www.sciencedirect.com/science/article/pii/0009261480800418.

[16] W. W. Brey, A. S. Edison, R. E. Nast, J. R. Rocca, S. Saha, and R. S. Withers. Design, construction, and validation of a 1-mm triple-resonance high-temperature-superconducting probe for NMR. 179(2):290–293. ISSN 1090-7807. . URL https://www.sciencedirect.com/science/article/pii/S1090780705004210.

[17] M. C. Mitchell, V. Spikmans, and A. J. de Mello. Microchip-based synthesis and analysis: Control of multicomponent reaction products and intermediates. 126 (1):24–27. . URL https://pubs.rsc.org/en/content/articlelanding/2001/an/b007397k.

[18] G. Cai, L. Xue, H. Zhang, and J. Lin. A Review on Micromixers. 8(9):274. . URL https://www.mdpi.com/2072-666X/8/9/274.

[19] G. Caruso, N. Musso, M. Grasso, A. Costantino, G. Lazzarino, F. Tascedda, M. Gulisano, S. M. Lunte, and F. Caraci. Microfluidics as a Novel Tool for Biological and Toxicological Assays in Drug Discovery Processes: Focus on Microchip Electrophoresis. 11(6):593. . URL https://www.mdpi.com/2072-666X/11/6/593.

[20] J. Cavanagh, N. J. Skelton, W. J. Fairbrother, M. Rance, and A. G. P. III. *Protein NMR Spectroscopy: Principles and Practice*. Elsevier. ISBN 978-0-08-047103-7.

[21] J. Chen, Z. Zhang, J. L. Stebbins, X. Zhang, R. Hoffman, A. Moore, and M. Pellecchia. A Fragment-Based Approach for the Discovery of Isoform-Specific p38α Inhibitors. 2(5):329–336. ISSN 1554-8929. . URL https://doi.org/10.1021/cb700025j.

[22] L. Ciobanu, D. A. Seeber, and C. H. Pennington. 3D MR microscopy with resolution 3.7μm by 3.3μm by 3.3μm. 158(1):178–182. ISSN 1090-7807. . URL http://www.sciencedirect.com/science/article/pii/S109078070200071X.

[23] T. D. W. Claridge. *High-Resolution NMR Techniques in Organic Chemistry*. Elsevier. ISBN 978-0-08-099993-7.

[24] B. Coggins, X. Li, A. McClerren, O. Hindsgaul, C. Raetz, and P. Zhou. Structure of the LpxC deacetylase with a bound substrate-analog inhibitor. 10(8):645–651. ISSN 1072-8368. .

[25] P. R. Costa, J. D. Gross, M. Hong, and R. G. Griffin. Solid-state NMR measurement of Ψ in peptides: A NCCN 2Q-heteronuclear local field experiment. 280 (1):95–103. ISSN 0009-2614. . URL https://www.sciencedirect.com/science/article/pii/S000926149701107X.

[26] F. Dalitz, M. Cudaj, M. Maiwald, and G. Guthausen. Process and reaction monitoring by low-field NMR spectroscopy. 60:52–70. ISSN 0079-6565. . URL http://www.sciencedirect.com/science/article/pii/S0079656511000860.

[27] C. Dalvit, P. Pevarello, M. Tatò, M. Veronesi, A. Vulpetti, and M. Sundström. Identification of compounds with binding affinity to proteins via magnetization transfer from bulk water. 18(1):65–68. ISSN 0925-2738. .

[28] F. Delaglio, S. Grzesiek, G. W. Vuister, G. Zhu, J. Pfeifer, and A. Bax. NMRPipe: A multidimensional spectral processing system based on UNIX pipes. 6(3):277–293. ISSN 0925-2738. .

[29] J.-P. Demers and A. Mittermaier. Binding Mechanism of an SH3 Domain Studied by NMR and ITC. 131(12):4355–4367. ISSN 0002-7863. . URL https://doi.org/10.1021/ja808255d.

[30] C. Dominguez, R. Boelens, and A. M. J. J. Bonvin. HADDOCK: A Protein-Protein Docking Approach Based on Biochemical or Biophysical Information. 125(7): 1731–1737. ISSN 0002-7863. . URL https://doi.org/10.1021/ja026939x.

[31] M. Du, Z. Ma, X. Ye, and Z. Zhou. On-chip fast mixing by a rotary peristaltic micropump with a single structural layer. 56(4):1047–1054. ISSN 1869-1900. . URL https://doi.org/10.1007/s11431-013-5140-6.

[32] K. Ehrmann, M. Gersbach, P. Pascoal, F. Vincent, C. Massin, D. Stamou, P. A. Besse, H. Vogel, and R. S. Popovic. Sample patterning on NMR surface microcoils. 178(1):96–105. ISSN 1090-7807. . URL http://www.sciencedirect.com/science/article/pii/S1090780705002983.

[33] G. R. Eldridge, H. C. Vervoort, C. M. Lee, P. A. Cremin, C. T. Williams, S. M. Hart, M. G. Goering, M. O'Neil-Johnso, and L. Zeng. High-Throughput Method for the Production and Analysis of Large Natural Product Libraries for Drug Discovery. 74(16):3963–3971. ISSN 0003-2700. . URL https://doi.org/10.1021/ac025534s.

[34] C. G. England, E. B. Ehlerding, and W. Cai. NanoLuc: A Small Luciferase Is Brightening Up the Field of Bioluminescence. 27(5):1175–1187. ISSN 1043-1802. . URL https://doi.org/10.1021/acs.bioconjchem.6b00112.

[35] P. Eribol, A. K. Uguz, and K. O. Ulgen. Screening applications in drug discovery based on microfluidic technology. 10(1):011502. . URL https://aip.scitation.org/doi/abs/10.1063/1.4940886.

[36] F. Evanics, J. L. Kitevski, I. Bezsonova, J. Forman-Kay, and R. S. Prosser. 19F NMR studies of solvent exposure and peptide binding to an SH3 domain. 1770 (2):221–230. ISSN 0304-4165. . URL https://www.sciencedirect.com/science/article/pii/S030441650600314X.

[37] p. u. family=Bentum, given=P. J. M., J. W. G. Janssen, and A. P. M. Kentgens. Towards nuclear magnetic resonance μ-spectroscopy and μ-imaging. 129 (9):793–803, . ISSN 1364-5528. . URL https://pubs.rsc.org/en/content/articlelanding/2004/an/b404497p.

[38] p. u. family=Bentum, given=P. J. M., J. W. G. Janssen, A. P. M. Kentgens, J. Bart, and J. G. E. Gardeniers. Stripline probes for nuclear magnetic resonance. 189(1): 104–113, . ISSN 1090-7807. . URL http://www.sciencedirect.com/science/article/pii/S1090780707002546.

[39] H. Fang, Y. Sun, X. Wang, M. Sharma, Z. Chen, X. Cao, M. Utz, and Z. Tian. Probing the kinetics in supramolecular chemistry and molecular assembly by microfluidic-NMR spectroscopy. 61(11):1460–1464. ISSN 1869-1870. . URL https://doi.org/10.1007/s11426-018-9293-3.

[40] P. J. Farber and A. Mittermaier. Relaxation dispersion NMR spectroscopy for the study of protein allostery. 7(2):191–200. ISSN 1867-2450. . URL https://www.ncbi.nlm.nih.gov/pmc/articles/PMC5425744/.

[41] N. A. Farrow, O. Zhang, J. D. Forman-Kay, and L. E. Kay. A heteronuclear correlation experiment for simultaneous determination of 15N longitudinal decay and chemical exchange rates of systems in slow equilibrium. 4(5):727–734. ISSN 0925-2738. .

[42] M. Fekete, F. Ahwal, and S. B. Duckett. Remarkable Levels of 15N Polarization Delivered through SABRE into Unlabeled Pyridine, Pyrazine, or Metronidazole Enable Single Scan NMR Quantification at the mM Level. 124(22):4573–4580. ISSN 1520-6106. . URL https://doi.org/10.1021/acs.jpcb.0c02583.

[43] S. Feng, J. K. Chen, H. Yu, J. A. Simon, and S. L. Schreiber. Two Binding Orientations for Peptides to the Src SH3 Domain: Development of a General Model for SH3-Ligand Interactions. 266(5188):1241–1247, . . URL https://www.science.org/doi/10.1126/science.7526465.

[44] S. Feng, C. Kasahara, R. J. Rickles, and S. L. Schreiber. Specific interactions outside the proline-rich core of two classes of Src homology 3 ligands. 92(26):12408–12415, . . URL https://www.pnas.org/doi/10.1073/pnas.92.26.12408.

[45] X. Feng, M. Edén, A. Brinkmann, H. Luthman, L. Eriksson, A. Gräslund, O. N. Antzutkin, and M. H. Levitt. Direct Determination of a Peptide Torsional Angle ψ by Double-Quantum Solid-State NMR. 119(49):12006–12007, . ISSN 0002-7863. . URL https://doi.org/10.1021/ja972252e.

[46] A. Fernández-la Villa, D. F. Pozo-Ayuso, and M. Castaño Álvarez. Microfluidics and electrochemistry: An emerging tandem for next-generation analytical microsystems. 15:175–185. ISSN 2451-9103. . URL http://www.sciencedirect.com/science/article/pii/S2451910319300663.

[47] G. Finch, A. Yilmaz, and M. Utz. An optimised detector for in-situ high-resolution NMR in microfluidic devices. 262:73–80. ISSN 1090-7807. . URL http://www.sciencedirect.com/science/article/pii/S1090780715002992.

[48] R. M. Fratila and A. H. Velders. Small-Volume Nuclear Magnetic Resonance Spectroscopy. 4(1):227–249. . URL https://doi.org/10.1146/annurev-anchem-061010-114024.

[49] A. Friberg, D. Vigil, B. Zhao, R. N. Daniels, J. P. Burke, P. M. Garcia-Barrantes, D. Camper, B. A. Chauder, T. Lee, E. T. Olejniczak, and S. W. Fesik. Discovery of Potent Myeloid Cell Leukemia 1 (Mcl-1) Inhibitors Using Fragment-Based Methods and Structure-Based Design. 56(1):15–30. ISSN 0022-2623. . URL https://doi.org/10.1021/jm301448p.

[50] A. Furukawa, T. Konuma, S. Yanaka, and K. Sugase. Quantitative analysis of protein–ligand interactions by NMR. 96:47–57. ISSN 0079-6565. . URL http://www.sciencedirect.com/science/article/pii/S007965651600008X.

[51] K. H. Gardner and L. E. Kay. Production and Incorporation of 15N, 13C, 2H (1H-δ1 Methyl) Isoleucine into Proteins for Multidimensional NMR Studies. 119(32): 7599–7600. ISSN 0002-7863. . URL https://doi.org/10.1021/ja9706514.

[52] Z. Gerdes, M. Hermann, M. Ogonowski, and E. Gorokhova. A novel method for assessing microplastic effect in suspension through mixing test and reference materials. 9(1):10695. ISSN 2045-2322. . URL https://www.nature.com/articles/s41598-019-47160-1.

[53] S. Ghosh, A. Sengupta, and K. Chandra. SOFAST-HMQC—an efficient tool for metabolomics. 409(29):6731–6738. ISSN 1618-2650. . URL https://doi.org/10.1007/s00216-017-0676-0.

[54] A. G. Goloshevsky, J. H. Walton, M. V. Shutov, p. u. family=Ropp, given=J. S., S. D. Collins, and M. J. McCarthy. Development of low field nuclear magnetic resonance microcoils. 76(2):024101. ISSN 0034-6748. . URL https://aip.scitation.org/doi/10.1063/1.1848659.

[55] S. H. Grimm, G. Höfner, and K. T. Wanner. MS Binding Assays for the Three Monoamine Transporters Using the Triple Reuptake Inhibitor (1R,3S)-Indatraline as Native Marker. 10(6):1027–1039. ISSN 1860-7179. . URL https://chemistry-europe.onlinelibrary.wiley.com/doi/full/10.1002/cmdc.201500084.

[56] W. H. Grover, A. M. Skelley, C. N. Liu, E. T. Lagally, and R. A. Mathies. Monolithic membrane valves and diaphragm pumps for practical large-scale integration into glass microfluidic devices. 89(3):315–323. ISSN 09254005. . URL https://linkinghub.elsevier.com/retrieve/pii/S0925400502004689.

[57] O. G. Gruschke, N. Baxan, L. Clad, K. Kratt, p. u. family=Elverfeldt, given=Dominik, A. Peter, J. Hennig, V. Badilita, U. Wallrabe, and J. G. Korvink. Lab on a chip phased-array MR multi-platform analysis system. 12(3):495–502. ISSN 1473-0189. . URL https://pubs.rsc.org/en/content/articlelanding/2012/lc/c2lc20585h.

[58] S. Grzesiek and A. Bax. Correlating backbone amide and side chain resonances in larger proteins by multiple relayed triple resonance NMR. 114(16):6291–6293, . ISSN 0002-7863. . URL https://doi.org/10.1021/ja00042a003.

[59] S. Grzesiek and A. Bax. An efficient experiment for sequential backbone assignment of medium-sized isotopically enriched proteins. 99(1):201–207, . ISSN 0022-2364. . URL http://www.sciencedirect.com/science/article/pii/0022236492901698.

[60] S. Grzesiek, J. Anglister, and A. Bax. Correlation of Backbone Amide and Aliphatic Side-Chain Resonances in 13C/15N-Enriched Proteins by Isotropic

Mixing of 13C Magnetization. 101(1):114–119. ISSN 1064-1866. . URL http://www.sciencedirect.com/science/article/pii/S1064186683710198.

[61] X. Guo. Surface plasmon resonance based biosensor technique: A review. 5(7): 483–501. ISSN 1864-0648. . URL https://onlinelibrary.wiley.com/doi/abs/10.1002/jbio.201200015.

[62] C. H. Hardman, R. W. Broadhurst, A. R. C. Raine, K. D. Grasser, J. O. Thomas, and E. D. Laue. Structure of the A-Domain of HMG1 and Its Interaction with DNA as Studied by Heteronuclear Three- and Four-Dimensional NMR Spectroscopy. 34(51):16596–16607. ISSN 0006-2960. . URL https://doi.org/10.1021/bi00051a007.

[63] P. Hentschel, K. Holtin, L. Steinhauser, and K. Albert. Monitoring the On-line Titration of Enantiomeric Omeprazole Employing Continuous-flow Capillary Microcoil 1H NMR Spectroscopy. 24(12):1074–1076. ISSN 1520-636X. . URL https://onlinelibrary.wiley.com/doi/abs/10.1002/chir.22099.

[64] J. Heuninck, C. Hounsou, E. Dupuis, E. Trinquet, B. Mouillac, J.-P. Pin, D. Bonnet, and T. Durroux. Time-Resolved FRET-Based Assays to Characterize G Protein-Coupled Receptor Hetero-oligomer Pharmacology. In M. Tiberi, editor, *G Protein-Coupled Receptor Signaling: Methods and Protocols*, Methods in Molecular Biology, pages 151–168. Springer. ISBN 978-1-4939-9121-1. . URL https://doi.org/10.1007/978-1-4939-9121-1_8.

[65] S. Huang, C. Li, B. Lin, and J. Qin. Microvalve and micropump controlled shuttle flow microfluidic device for rapid DNA hybridization. 10(21):2925–2931. . URL https://pubs.rsc.org/en/content/articlelanding/2010/lc/c005227b.

[66] E. C. Hulme and M. A. Trevethick. Ligand binding assays at equilibrium: Validation and interpretation. 161(6):1219–1237. ISSN 0007-1188. . URL https://www.ncbi.nlm.nih.gov/pmc/articles/PMC3000649/.

[67] K. P. Imaduwage, E. P. Go, Z. Zhu, and H. Desaire. HAMS: High-Affinity Mass Spectrometry Screening. A high-throughput screening method for identifying the tightest-binding lead compounds for target proteins with no false positive identifications. 27(11):1870–1877. ISSN 1044-0305. . URL https://www.ncbi.nlm.nih.gov/pmc/articles/PMC5501305/.

[68] J. M. Janz, T. P. Sakmar, and K. C. Min. A Novel Interaction between Atrophin-interacting Protein 4 and β-p21-activated Kinase-interactive Exchange Factor Is Mediated by an SH3 Domain*. 282(39):28893–28903. ISSN 0021-9258. . URL https://www.sciencedirect.com/science/article/pii/S0021925820586225.

[69] M. Kakuta, D. A. Jayawickrama, A. M. Wolters, A. Manz, and J. V. Sweedler. Micromixer-Based Time-Resolved NMR: Applications to Ubiquitin Protein Conformation. 75(4):956–960. ISSN 0003-2700. . URL https://doi.org/10.1021/ac026076q.

[70] Y. S. Kang, W. Kim, Y. H. Huh, J. Bae, J. S. Kim, and W. K. Song. P130Cas Attenuates Epidermal Growth Factor (EGF) Receptor Internalization by Modulating EGF-Triggered Dynamin Phosphorylation. 6(5):e20125. ISSN 1932-6203. . URL https://journals.plos.org/plosone/article?id=10.1371/journal.pone.0020125.

[71] R. Kapeller, K. V. Prasad, O. Janssen, W. Hou, B. S. Schaffhausen, C. E. Rudd, and L. C. Cantley. Identification of two SH3-binding motifs in the regulatory subunit of phosphatidylinositol 3-kinase. 269(3):1927–1933. ISSN 0021-9258. . URL https://www.sciencedirect.com/science/article/pii/S0021925817421156.

[72] L. M. Karnitz, S. L. Sutor, and R. T. Abraham. The Src-family kinase, Fyn, regulates the activation of phosphatidylinositol 3-kinase in an interleukin 2-responsive T cell line. 179(6):1799–1808. ISSN 0022-1007. . URL https://doi.org/10.1084/jem.179.6.1799.

[73] B. K. Kay, M. P. Williamson, and M. Sudol. The importance of being proline: The interaction of proline-rich motifs in signaling proteins with their cognate domains. 14(2):231–241. ISSN 1530-6860. . URL https://onlinelibrary.wiley.com/doi/abs/10.1096/fasebj.14.2.231.

[74] J. Keeler. *Understanding NMR Spectroscopy*. John Wiley & Sons. ISBN 978-1-119-96493-3.

[75] A. P. M. Kentgens, J. Bart, p. u. family=Bentum, given=P. J. M., A. Brinkmann, p. u. family=Eck, given=E. R. H., J. G. E. Gardeniers, J. W. G. Janssen, P. Knijn, S. Vasa, and M. H. W. Verkuijlen. High-resolution liquid- and solid-state nuclear magnetic resonance of nanoliter sample volumes using microcoil detectors. 128 (5):052202. ISSN 0021-9606. . URL https://aip.scitation.org/doi/10.1063/1.2833560.

[76] T. Kesti, A. Ruppelt, J.-H. Wang, M. Liss, R. Wagner, K. Taskén, and K. Saksela. Reciprocal Regulation of SH3 and SH2 Domain Binding via Tyrosine Phosphorylation of a Common Site in CD3ϵ. 179(2):878–885. ISSN 0022-1767, 1550-6606. . URL https://www.jimmunol.org/content/179/2/878.

[77] M. Khajeh, M. A. Bernstein, and G. A. Morris. A simple flowcell for reaction monitoring by NMR. 48(7):516–522. ISSN 1097-458X. . URL https://onlinelibrary.wiley.com/doi/abs/10.1002/mrc.2610.

[78] M. Kjaergaard, S. r. Brander, and F. M. Poulsen. Random coil chemical shift for intrinsically disordered proteins: Effects of temperature and pH. 49(2):139–149. ISSN 1573-5001. . URL https://doi.org/10.1007/s10858-011-9472-x.

[79] H. Kovacs, D. Moskau, and M. Spraul. Cryogenically cooled probes—a leap in NMR technology. 46(2):131–155. ISSN 0079-6565. . URL https://www.sciencedirect.com/science/article/pii/S0079656505000178.

[80] H. G. Krojanski, J. Lambert, Y. Gerikalan, D. Suter, and R. Hergenröder. Microslot NMR Probe for Metabolomics Studies. 80(22):8668–8672. ISSN 0003-2700. . URL https://doi.org/10.1021/ac801636a.

[81] N. Kurochkina and U. Guha. SH3 domains: Modules of protein–protein interactions. 5(1):29–39. ISSN 1867-2450. . URL https://www.ncbi.nlm.nih.gov/pmc/articles/PMC5418429/.

[82] K. Länge, B. E. Rapp, and M. Rapp. Surface acoustic wave biosensors: A review. 391(5):1509–1519. ISSN 1618-2650. . URL https://doi.org/10.1007/s00216-008-1911-5.

[83] M.-C. N. Le and Z. H. Fan. Exosome isolation using nanostructures and microfluidic devices. 16(2):022005. ISSN 1748-6041. . URL https://www.ncbi.nlm.nih.gov/pmc/articles/PMC8082697/.

[84] K.-M. Lei, H. Heidari, P.-I. Mak, M.-K. Law, F. Maloberti, and R. P. Martins. A Handheld High-Sensitivity Micro-NMR CMOS Platform With B-Field Stabilization for Multi-Type Biological/Chemical Assays. 52(1):284–297. ISSN 1558-173X. .

[85] P. Lepucki, A. P. Dioguardi, D. Karnaushenko, O. G. Schmidt, and H.-J. Grafe. The normalized limit of detection in NMR spectroscopy. 332:107077. ISSN 1090-7807. . URL https://www.sciencedirect.com/science/article/pii/S109078072100166X.

[86] M. H. Levitt. *Spin Dynamics: Basics of Nuclear Magnetic Resonance*. Wiley. ISBN 978-0-470-51712-3.

[87] Y. Li, T. M. Logan, A. S. Edison, and A. Webb. Design of small volume HX and triple-resonance probes for improved limits of detection in protein NMR experiments. 164(1):128–135. ISSN 1090-7807. . URL http://www.sciencedirect.com/science/article/pii/S1090780703001848.

[88] W. A. Lim, F. M. Richards, and R. O. Fox. Structural determinants of peptide-binding orientation and of sequence specificity in SH3 domains. 372(6504):375–379. ISSN 1476-4687. . URL https://www.nature.com/articles/372375a0.

[89] Y. Lin, S. Schiavo, J. Orjala, P. Vouros, and R. Kautz. Microscale LC-MS-NMR Platform Applied to the Identification of Active Cyanobacterial Metabolites. 80 (21):8045–8054. ISSN 0003-2700. . URL https://doi.org/10.1021/ac801049k.

[90] J. C. Lindon, J. K. Nicholson, and I. D. Wilson. Direct coupling of chromatographic separations to NMR spectroscopy. 29(1):1–49. ISSN 0079-6565. . URL http://www.sciencedirect.com/science/article/pii/0079656595010270.

[91] A.-L. Liu, Z.-Q. Li, Z.-Q. Wu, and X.-H. Xia. Study on the photocatalytic reaction kinetics in a TiO2 nanoparticles coated microreactor integrated microfluidics device. 182:544–548, . ISSN 0039-9140. . URL http://www.sciencedirect.com/science/article/pii/S0039914018301371.

[92] Y. Liu, L. Sun, H. Zhang, L. Shang, and Y. Zhao. Microfluidics for Drug Development: From Synthesis to Evaluation. 121(13):7468–7529, . ISSN 0009-2665. . URL https://doi.org/10.1021/acs.chemrev.0c01289.

[93] M. J. Lohse, S. Nuber, and C. Hoffmann. Fluorescence/bioluminescence resonance energy transfer techniques to study G-protein-coupled receptor activation and signaling. 64(2):299–336. ISSN 1521-0081. .

[94] J. Loria, M. Rance, and A. Palmer III. A relaxation-compensated Carr-Purcell-Meiboom-Gill sequence for characterizing chemical exchange by NMR spectroscopy [13]. 121(10):2331–2332. .

[95] T. Luo, L. Fan, R. Zhu, and D. Sun. Microfluidic Single-Cell Manipulation and Analysis: Methods and Applications. 10(2):104. ISSN 2072-666X. . URL https://www.ncbi.nlm.nih.gov/pmc/articles/PMC6412357/.

[96] Y. Maguire, I. L. Chuang, S. Zhang, and N. Gershenfeld. Ultra-small-sample molecular structure detection using microslot waveguide nuclear spin resonance. 104(22):9198–9203. ISSN 0027-8424, 1091-6490. . URL https://www.pnas.org/content/104/22/9198.

[97] M. Maiwald, H. H. Fischer, Y.-K. Kim, K. Albert, and H. Hasse. Quantitative high-resolution on-line NMR spectroscopy in reaction and process monitoring. 166(2): 135–146. ISSN 1090-7807. . URL http://www.sciencedirect.com/science/article/pii/S1090780703003082.

[98] A. Manz, N. Graber, and H. M. Widmer. Miniaturized total chemical analysis systems: A novel concept for chemical sensing. 1(1):244–248. ISSN 0925-4005. . URL http://www.sciencedirect.com/science/article/pii/092540059080209I.

[99] L. Mariño Pérez, F. S. Ielasi, L. M. Bessa, D. Maurin, J. Kragelj, M. Blackledge, N. Salvi, G. Bouvignies, A. Palencia, and M. R. b. Jensen. Visualizing protein breathing motions associated with aromatic ring flipping. 602

(7898):695–700. ISSN 1476-4687. . URL https://www.nature.com/articles/s41586-022-04417-6.

[100] P. R. L. Markwick, T. Malliavin, and M. Nilges. Structural Biology by NMR: Structure, Dynamics, and Interactions. 4(9):e1000168. ISSN 1553-7358. . URL https://journals.plos.org/ploscompbiol/article?id=10.1371/journal.pcbi.1000168.

[101] J. M. Martin-Garcia, I. Luque, J. Ruiz-Sanz, and A. Camara-Artigas. The promiscuous binding of the Fyn SH3 domain to a peptide from the NS5A protein. 68 (8):1030–1040. ISSN 0907-4449. . URL //scripts.iucr.org/cgi-bin/paper?mh5062.

[102] C. Massin, F. Vincent, A. Homsy, K. Ehrmann, G. Boero, P. A. Besse, A. Daridon, E. Verpoorte, p. u. family=Rooij, given=N. F, and R. S. Popovic. Planar microcoil-based microfluidic NMR probes. 164(2):242–255. ISSN 1090-7807. . URL http://www.sciencedirect.com/science/article/pii/S1090780703001514.

[103] B. Mayer. SH3 domains: Complexity in moderation. 114(7):1253–1263. ISSN 0021-9533. . URL https://doi.org/10.1242/jcs.114.7.1253.

[104] M. Mayer and B. Meyer. Characterization of Ligand Binding by Saturation Transfer Difference NMR Spectroscopy. 38(12):1784–1788. ISSN 1521-3773. . URL https://onlinelibrary.wiley.com/doi/abs/10.1002/%28SICI%291521-3773%2819990614%2938%3A12%3C1784%3A%3AAID-ANIE1784%3E3.0.CO%3B2-Q.

[105] J. A. McCammon, B. R. Gelin, and M. Karplus. Dynamics of folded proteins. 267 (5612):585–590. ISSN 1476-4687. . URL https://www.nature.com/articles/267585a0.

[106] L. P. McIntosh and F. W. Dahlquist. Biosynthetic Incorporation of 15N and 13C for Assignment and Interpretation of Nuclear Magnetic Resonance Spectra of Proteins. 23(1):1–38. ISSN 1469-8994, 0033-5835. . URL https://www.cambridge.org/core/journals/quarterly-reviews-of-biophysics/article/biosynthetic-incorporation-of-15n-and-13c-for-assignment-and-interpretation-of-FC91E81591CAD6D61CD3D37DA5F2C7FD.

[107] A. McPherson and J. A. Gavira. Introduction to protein crystallization. 70:2–20. ISSN 2053-230X. . URL https://www.ncbi.nlm.nih.gov/pmc/articles/PMC3943105/.

[108] Z. Miao, M. Jin, X. Liu, W. Guo, X. Jin, H. Liu, and Y. Wang. The application of HPLC and microprobe NMR spectroscopy in the identification of metabolites in complex biological matrices. 407(12):3405–3416. ISSN 1618-2642. . URL https://www.ncbi.nlm.nih.gov/pmc/articles/PMC4392169/.

[109] D. Migliozzi, B. Pelz, D. G. Dupouy, A.-L. Leblond, A. Soltermann, and M. A. M. Gijs. Microfluidics-assisted multiplexed biomarker detection for in situ mapping of immune cells in tumor sections. 5(1):1–12. ISSN 2055-7434. . URL https://www.nature.com/articles/s41378-019-0104-z.

[110] A. K. Mittermaier and L. E. Kay. Observing biological dynamics at atomic resolution using NMR. 34(12):601–611. ISSN 0968-0004. . URL https://www.sciencedirect.com/science/article/pii/S0968000409001649.

[111] G. Moncalián, N. Cárdenes, Y. L. Deribe, M. Spínola-Amilibia, I. Dikic, and J. Bravo. Atypical Polyproline Recognition by the CMS N-terminal Src Homology 3 Domain*. 281(50):38845–38853. ISSN 0021-9258. . URL https://www.sciencedirect.com/science/article/pii/S0021925820718776.

[112] G. T. Montelione, B. A. Lyons, S. D. Emerson, and M. Tashiro. An efficient triple resonance experiment using carbon-13 isotropic mixing for determining sequence-specific resonance assignments of isotopically-enriched proteins. 114(27):10974–10975. ISSN 0002-7863. . URL https://doi.org/10.1021/ja00053a051.

[113] S. Mori, C. Abeygunawardana, M. O. Johnson, and P. C. M. Vanzijl. Improved Sensitivity of HSQC Spectra of Exchanging Protons at Short Interscan Delays Using a New Fast HSQC (FHSQC) Detection Scheme That Avoids Water Saturation. 108(1):94–98. ISSN 1064-1866. . URL http://www.sciencedirect.com/science/article/pii/S1064186685711090.

[114] C. J. Morton, D. J. Pugh, E. L. Brown, J. D. Kahmann, D. A. Renzoni, and I. D. Campbell. Solution structure and peptide binding of the SH3 domain from human Fyn. 4(6):705–714. ISSN 0969-2126. . URL http://www.sciencedirect.com/science/article/pii/S0969212696000767.

[115] A. R. Mukhametgalieva, I. V. Zueva, A. R. Aglyamova, S. V. Lushchekina, and P. Masson. A new sensitive spectrofluorimetric method for measurement of activity and kinetic study of cholinesterases. 1868(1):140270. ISSN 1570-9639. . URL http://www.sciencedirect.com/science/article/pii/S1570963919301566.

[116] A. Musacchio. How SH3 domains recognize proline. In *Advances in Protein Chemistry*, volume 61 of *Protein Modules and Protein-Protein Interaction*, pages 211–268. Academic Press. . URL https://www.sciencedirect.com/science/article/pii/S006532330261006X.

[117] J. T. Nguyen, M. Porter, M. Amoui, W. T. Miller, R. N. Zuckermann, and W. A. Lim. Improving SH3 domain ligand selectivity using a non-natural scaffold. 7(7):463–473, . ISSN 1074-5521. . URL https://www.sciencedirect.com/science/article/pii/S1074552100001307.

[118] J. T. Nguyen, C. W. Turck, F. E. Cohen, R. N. Zuckermann, and W. A. Lim. Exploiting the Basis of Proline Recognition by SH3 and WW Domains: Design of N-Substituted Inhibitors. 282(5396):2088–2092, . . URL https://www.science.org/doi/10.1126/science.282.5396.2088.

[119] J. Nilsson, M. Evander, B. Hammarström, and T. Laurell. Review of cell and particle trapping in microfluidic systems. 649(2):141–157. ISSN 0003-2670. . URL http://www.sciencedirect.com/science/article/pii/S0003267009009222.

[120] M. E. Noble, A. Musacchio, M. Saraste, S. A. Courtneidge, and R. K. Wierenga. Crystal structure of the SH3 domain in human Fyn; comparison of the three-dimensional structures of SH3 domains in tyrosine kinases and spectrin. 12 (7):2617–2624. ISSN 1460-2075. . URL https://europepmc.org/articles/PMC413508.

[121] D. L. Olson, T. L. Peck, A. G. Webb, R. L. Magin, and J. V. Sweedler. High-Resolution Microcoil 1H-NMR for Mass-Limited, Nanoliter-Volume Samples. 270(5244):1967–1970. ISSN 0036-8075, 1095-9203. . URL https://science.sciencemag.org/content/270/5244/1967.

[122] T. L. Peck, R. L. Magin, and P. C. Lauterbur. Design and Analysis of Microcoils for NMR Microscopy. 108(2):114–124. ISSN 1064-1866. . URL http://www.sciencedirect.com/science/article/pii/S1064186685711120.

[123] M. F. Perutz. Stereochemistry of Cooperative Effects in Haemoglobin: Haem–Haem Interaction and the Problem of Allostery. 228(5273):726–734. ISSN 1476-4687. . URL https://www.nature.com/articles/228726a0.

[124] K. Pervushin, R. Riek, G. Wider, and K. Wüthrich. Attenuated T2 relaxation by mutual cancellation of dipole–dipole coupling and chemical shift anisotropy indicates an avenue to NMR structures of very large biological macromolecules in solution. 94(23):12366–12371. . URL https://www.pnas.org/doi/full/10.1073/pnas.94.23.12366.

[125] W. Peti, J. Norcross, G. Eldridge, and M. O'Neil-Johnson. Biomolecular NMR Using a Microcoil NMR Probe - New Technique for the Chemical Shift Assignment of Aromatic Side Chains in Proteins. 126(18):5873–5878, . ISSN 0002-7863. . URL https://doi.org/10.1021/ja039779d.

[126] W. Peti, R. Page, K. Moy, M. O'Neil-Johnson, I. A. Wilson, R. C. Stevens, and K. Wüthrich. Towards miniaturization of a structural genomics pipeline using micro-expression and microcoil NMR. 6(4):259–267, . ISSN 1345-711X, 1570-0267. . URL http://link.springer.com/10.1007/s10969-005-9000-x.

[127] J. C. Phillips, A. Wlodawer, M. M. Yevitz, and K. O. Hodgson. Applications of synchrotron radiation to protein crystallography: Preliminary results. 73(1):128–132. ISSN 0027-8424, 1091-6490. . URL https://www.pnas.org/content/73/1/128.

[128] I. Pritišanac, T. R. Alderson, and P. Güntert. Automated assignment of methyl NMR spectra from large proteins. 118–119:54–73. ISSN 0079-6565. . URL https://www.sciencedirect.com/science/article/pii/S0079656520300133.

[129] E. Rascol, S. Villette, E. Harté, and I. D. Alves. Plasmon Waveguide Resonance: Principles, Applications and Historical Perspectives on Instrument Development. 26(21):6442. ISSN 1420-3049. . URL https://www.mdpi.com/1420-3049/26/21/6442.

[130] L. Renaud, M. Armenean, L. Berry, P. Kleimann, P. Morin, M. Pitaval, J. O'Brien, M. Brunet, and H. Saint-Jalmes. Implantable planar rf microcoils for NMR microspectroscopy. 99(3):244–248. ISSN 0924-4247. . URL http://www.sciencedirect.com/science/article/pii/S0924424701009141.

[131] D. A. Renzoni, D. J. R. Pugh, G. Siligardi, P. Das, C. J. Morton, C. Rossi, M. D. Waterfield, I. D. Campbell, and J. E. Ladbury. Structural and Thermodynamic Characterization of the Interaction of the SH3 Domain from Fyn with the Proline-Rich Binding Site on the p85 Subunit of PI3-Kinase. 35(49):15646–15653. ISSN 0006-2960. . URL https://doi.org/10.1021/bi9620969.

[132] S. Rezzi, F. A. Vera, F.-P. J. Martin, S. Wang, D. Lawler, and S. Kochhar. Automated SPE-RP-HPLC fractionation of biofluids combined to off-line NMR spectroscopy for biomarker identification in metabonomics. 871(2):271–278. ISSN 1570-0232. . URL http://www.sciencedirect.com/science/article/pii/S1570023208002286.

[133] J. A. Rogers, R. J. Jackman, G. M. Whitesides, D. L. Olson, and J. V. Sweedler. Using microcontact printing to fabricate microcoils on capillaries for high resolution proton nuclear magnetic resonance on nanoliter volumes. 70(18):2464–2466. ISSN 0003-6951, 1077-3118. . URL http://aip.scitation.org/doi/10.1063/1.118857.

[134] P. Rossi, G. V. T. Swapna, Y. J. Huang, J. M. Aramini, C. Anklin, K. Conover, K. Hamilton, R. Xiao, T. B. Acton, A. Ertekin, J. K. Everett, and G. T. Montelione. A microscale protein NMR sample screening pipeline. 46(1):11–22. ISSN 1573-5001. . URL https://doi.org/10.1007/s10858-009-9386-z.

[135] M. Rothbauer, B. E. Bachmann, C. Eilenberger, S. R. Kratz, S. Spitz, G. Höll, and P. Ertl. A Decade of Organs-on-a-Chip Emulating Human Physiology at

the Microscale: A Critical Status Report on Progress in Toxicology and Pharmacology. 12(5):470. ISSN 2072-666X. . URL https://www.ncbi.nlm.nih.gov/pmc/articles/PMC8143089/.

[136] C. E. Rudd, O. Janssen, Y.-C. Cai, p. u. family=Silva, given=Antonio J., M. Raab, and K. V. S. Prasad. Two-step TCRζ/CD3-CD4 and CD28 signaling in T cells: SH2/SH3 domains, protein-tyrosine and lipid kinases. 15(5):225–234. ISSN 0167-5699. . URL https://www.sciencedirect.com/science/article/pii/0167569994902488.

[137] H. Ryan, A. Smith, and M. Utz. Structural shimming for high-resolution nuclear magnetic resonance spectroscopy in lab-on-a-chip devices. 14(10):1678–1685, . ISSN 1473-0189. . URL https://pubs.rsc.org/en/content/articlelanding/2014/lc/c3lc51431e.

[138] H. Ryan, S.-H. Song, A. Zaß, J. Korvink, and M. Utz. Contactless NMR Spectroscopy on a Chip. 84(8):3696–3702, . ISSN 0003-2700. . URL https://doi.org/10.1021/ac300204z.

[139] J. Saliba, A. Daou, S. Damiati, J. Saliba, M. El-Sabban, and R. Mhanna. Development of Microplatforms to Mimic the In Vivo Architecture of CNS and PNS Physiology and Their Diseases. 9(6):285. ISSN 2073-4425. . URL https://www.mdpi.com/2073-4425/9/6/285.

[140] E. Samiei, M. Tabrizian, and M. Hoorfar. A review of digital microfluidics as portable platforms for lab-on a-chip applications. 16(13):2376–2396. . URL https://pubs.rsc.org/en/content/articlelanding/2016/lc/c6lc00387g.

[141] M. Sattler and S. W. Fesik. Use of deuterium labeling in NMR: Overcoming a sizeable problem. 4(11):1245–1249. ISSN 0969-2126. . URL https://www.sciencedirect.com/science/article/pii/S0969212696001335.

[142] P. Schanda and B. Brutscher. Very Fast Two-Dimensional NMR Spectroscopy for Real-Time Investigation of Dynamic Events in Proteins on the Time Scale of Seconds. 127(22):8014–8015. ISSN 0002-7863. . URL https://doi.org/10.1021/ja051306e.

[143] P. Schanda, E. Kupce, and B. Brutscher. SOFAST-HMQC experiments for recording two-dimensional heteronuclear correlation spectra of proteins within a few seconds. 33(4):199–211. ISSN 0925-2738. .

[144] G. Schlotterbeck, A. Ross, R. Hochstrasser, H. Senn, T. Kühn, D. Marek, and O. Schett. High-Resolution Capillary Tube NMR. A Miniaturized 5-μL High-Sensitivity TXI Probe for Mass-Limited Samples, Off-Line LC NMR, and HT NMR. 74(17):4464–4471. ISSN 0003-2700. . URL https://doi.org/10.1021/ac025556e.

[145] F. H. Schumann, H. Riepl, T. Maurer, W. Gronwald, K.-P. Neidig, and H. R. Kalbitzer. Combined chemical shift changes and amino acid specific chemical shift mapping of protein–protein interactions. 39(4):275–289. ISSN 1573-5001. . URL https://doi.org/10.1007/s10858-007-9197-z.

[146] S. Schütz and R. Sprangers. Methyl TROSY spectroscopy: A versatile NMR approach to study challenging biological systems. 116:56–84. ISSN 0079-6565. . URL https://www.sciencedirect.com/science/article/pii/S0079656519300470.

[147] S. Schwarzinger, G. J. A. Kroon, T. R. Foss, J. Chung, P. E. Wright, and H. J. Dyson. Sequence-Dependent Correction of Random Coil NMR Chemical Shifts. 123(13): 2970–2978. ISSN 0002-7863. . URL https://doi.org/10.1021/ja003760i.

[148] D. A. Seeber, R. L. Cooper, L. Ciobanu, and C. H. Pennington. Design and testing of high sensitivity microreceiver coil apparatus for nuclear magnetic resonance and imaging. 72(4):2171–2179. ISSN 0034-6748, 1089-7623. . URL http://aip.scitation.org/doi/10.1063/1.1359190.

[149] G. Senisterra, I. Chau, and M. Vedadi. Thermal denaturation assays in chemical biology. 10(2):128–136. ISSN 1557-8127. .

[150] M. Sharma and M. Utz. Modular transmission line probes for microfluidic nuclear magnetic resonance spectroscopy and imaging. 303:75–81. ISSN 1090-7807. . URL http://www.sciencedirect.com/science/article/pii/S1090780719300655.

[151] M.-y. Shen, F. P. Davis, and A. Sali. The optimal size of a globular protein domain: A simple sphere-packing model. 405(1):224–228. ISSN 0009-2614. . URL http://www.sciencedirect.com/science/article/pii/S000926140500196X.

[152] X. Shi, S. Opi, A. Lugari, A. Restouin, T. Coursindel, I. Parrot, J. Perez, E. Madore, P. Zimmermann, J. Corbeil, M. Huang, S. T. Arold, Y. Collette, and X. Morelli. Identification and biophysical assessment of the molecular recognition mechanisms between the human haemopoietic cell kinase Src homology domain 3 and ALG-2-interacting protein X. 431(1):93–102. ISSN 0264-6021. . URL https://doi.org/10.1042/BJ20100314.

[153] N. Spengler, A. Moazenzadeh, R. C. Meier, V. Badilita, J. G. Korvink, and U. Wallrabe. Micro-fabricated Helmholtz coil featuring disposable microfluidic sample inserts for applications in nuclear magnetic resonance. 24(3):034004. ISSN 0960-1317. . URL https://doi.org/10.1088%2F0960-1317%2F24%2F3%2F034004.

[154] J. Stocker, T. Peck, A. Webb, M. Feng, and R. Magin. Nanoliter volume, high-resolution NMR microspectroscopy using a 60-/spl mu/m planar microcoil. 44 (11):1122–1127. ISSN 1558-2531. .

[155] D. Stratmann, R. Boelens, and A. M. J. J. Bonvin. Quantitative use of chemical shifts for the modeling of protein complexes. 79(9):2662–2670. ISSN 1097-0134. . URL https://onlinelibrary.wiley.com/doi/abs/10.1002/prot.23090.

[156] I. Swyer, p. d. u. family=Ecken, given=Sebastian, B. Wu, A. Jenne, R. Soong, F. Vincent, D. Schmidig, T. Frei, F. Busse, H. J. Stronks, A. J. Simpson, and A. R. Wheeler. Digital microfluidics and nuclear magnetic resonance spectroscopy for in situ diffusion measurements and reaction monitoring. 19(4):641–653, . ISSN 1473-0189. . URL https://pubs.rsc.org/en/content/articlelanding/2019/lc/c8lc01214h.

[157] I. Swyer, R. Soong, M. D. M. Dryden, M. Fey, W. E. Maas, A. Simpson, and A. R. Wheeler. Interfacing digital microfluidics with high-field nuclear magnetic resonance spectroscopy. 16(22):4424–4435, . ISSN 1473-0189. . URL https://pubs.rsc.org/en/content/articlelanding/2016/lc/c6lc01073c.

[158] R. R. A. Syms, M. M. Ahmad, I. R. Young, D. J. Gilderdale, and D. J. Collins. Microengineered needle micro-coils for magnetic resonance spectroscopy. 16(12): 2755–2764. ISSN 0960-1317. . URL https://doi.org/10.1088%2F0960-1317%2F16%2F12%2F032.

[159] Q. Teng. *Structural Biology: Practical NMR Applications*. Springer Science & Business Media. ISBN 978-0-387-24368-9.

[160] S. Terry, J. Jerman, and J. Angell. A gas chromatographic air analyzer fabricated on a silicon wafer. 26(12):1880–1886. ISSN 1557-9646. .

[161] F. E. Torres, M. I. Recht, J. E. Coyle, R. H. Bruce, and G. Williams. Higher Throughput Calorimetry: Opportunities, Approaches and Challenges. 20(5):598–605. ISSN 0959-440X. . URL https://www.ncbi.nlm.nih.gov/pmc/articles/PMC2989423/.

[162] J. Trumbull, I. Glasgow, D. Beebe, and R. Magin. Integrating microfabricated fluidic systems and NMR spectroscopy. 47(1):3–7. ISSN 1558-2531. .

[163] H.-Y. Tseng, C.-H. Wang, W.-Y. Lin, and G.-B. Lee. Membrane-activated microfluidic rotary devices for pumping and mixing. 9(4):545–554. ISSN 1572-8781. . URL https://doi.org/10.1007/s10544-007-9062-6.

[164] M. A. Unger, H.-P. Chou, T. Thorsen, A. Scherer, and S. R. Quake. Monolithic Microfabricated Valves and Pumps by Multilayer Soft Lithography. 288(5463): 113–116. ISSN 0036-8075, 1095-9203. . URL https://science.sciencemag.org/content/288/5463/113.

[165] M. Urbaniak, F. Muskett, M. Finucane, S. Caddick, and D. Woolfson. Solution structure of a novel chromoprotein derived from apo-Neocarzinostatin and a synthetic chromophore. 41(39):11731–11739. ISSN 0006-2960. .

[166] G. W. Vuister and A. Bax. Resolution enhancement and spectral editing of uniformly 13C-enriched proteins by homonuclear broadband 13C decoupling. 98 (2):428–435. ISSN 0022-2364. . URL http://www.sciencedirect.com/science/article/pii/002223649290144V.

[167] A. Webb. Increasing the Sensitivity of Magnetic Resonance Spectroscopy and Imaging. 84(1):9–16, . ISSN 0003-2700. . URL https://doi.org/10.1021/ac201500v.

[168] A. G. Webb. Radiofrequency microcoils for magnetic resonance imaging and spectroscopy. 229:55–66, . ISSN 1090-7807. . URL http://www.sciencedirect.com/science/article/pii/S1090780712003187.

[169] D. B. Weibel, M. Kruithof, S. Potenta, S. K. Sia, A. Lee, and G. M. Whitesides. Torque-Actuated Valves for Microfluidics. 77(15):4726–4733. ISSN 0003-2700. . URL https://doi.org/10.1021/ac048303p.

[170] H. Wensink, F. Benito-Lopez, D. C. Hermes, W. Verboom, H. J. G. E. Gardeniers, D. N. Reinhoudt, and p. d. u. family=Berg, given=Albert. Measuring reaction kinetics in a lab-on-a-chip by microcoil NMR. 5(3):280–284. ISSN 1473-0189. . URL https://pubs.rsc.org/en/content/articlelanding/2005/lc/b414832k.

[171] G. M. Whitesides. The origins and the future of microfluidics. 442(7101):368–373. ISSN 1476-4687. . URL https://www.nature.com/articles/nature05058.

[172] S. Wiesner and R. Sprangers. Methyl groups as NMR probes for biomolecular interactions. 35:60–67. ISSN 0959-440X. . URL http://www.sciencedirect.com/science/article/pii/S0959440X15001256.

[173] M. P. Williamson. Using chemical shift perturbation to characterise ligand binding. 73:1–16. ISSN 0079-6565. . URL http://www.sciencedirect.com/science/article/pii/S0079656513000265.

[174] R. Williamson, M. Carr, T. Frenkiel, J. Feeney, and R. Freedman. Mapping the binding site for matrix metalloproteinase on the N-terminal domain of the tissue inhibitor of metalloproteinases-2 by NMR chemical shift perturbation. 36(45): 13882–13889. ISSN 0006-2960. .

[175] D. S. Wishart, B. D. Sykes, and F. M. Richards. The chemical shift index: A fast and simple method for the assignment of protein secondary structure through NMR spectroscopy. 31(6):1647–1651, . ISSN 0006-2960, 1520-4995. . URL https://pubs.acs.org/doi/abs/10.1021/bi00121a010.

[176] D. S. Wishart, B. D. Sykes, and F. M. Richards. Relationship between nuclear magnetic resonance chemical shift and protein secondary structure. 222(2):311–333, . ISSN 0022-2836. . URL https://www.sciencedirect.com/science/article/pii/002228369190214Q.

[177] A. Wlodawer, W. Minor, Z. Dauter, and M. Jaskolski. Protein crystallography for non-crystallographers, or how to get the best (but not more) from published macromolecular structures. 275(1):1–21. ISSN 1742-4658. . URL https://febs.onlinelibrary.wiley.com/doi/abs/10.1111/j.1742-4658.2007.06178.x.

[178] A. M. Wolters, D. A. Jayawickrama, and J. V. Sweedler. Microscale NMR. 6(5): 711–716. ISSN 1367-5931. . URL http://www.sciencedirect.com/science/article/pii/S1367593102003824.

[179] K. Wüthrich. *NMR of Proteins and Nucleic Acids*. Wiley. ISBN 978-0-471-82893-8.

[180] K. Wuthrich. Protein structure determination in solution by NMR spectroscopy. 265(36):22059–22062.

[181] K. Yakimchuk. Receptor-Ligand Binding Assays. URL /method/Receptor-Ligand-Binding-Assays.html.

[182] K. Yamasaki, T. Yamasaki, M. Takahashi, and H. Suematsu. A mixing microfluidic chip for real-time NMR monitoring of macromolecular reactions. 170(3):363–368. ISSN 0021-924X. . URL https://doi.org/10.1093/jb/mvab048.

[183] K. Yamauchi, J. W. G. Janssen, and A. P. M. Kentgens. Implementing solenoid microcoils for wide-line solid-state NMR. 167(1):87–96. ISSN 1090-7807. . URL http://www.sciencedirect.com/science/article/pii/S1090780703004245.

[184] T. Yamazaki, J. D. Forman-Kay, and L. E. Kay. Two-dimensional NMR experiments for correlating carbon-13.beta. and proton.delta./.epsilon. chemical shifts of aromatic residues in 13C-labeled proteins via scalar couplings. 115(23):11054–11055. ISSN 0002-7863. . URL https://doi.org/10.1021/ja00076a099.

[185] A. Yang, T. B. Hoang, M. Dridi, C. Deeb, M. H. Mikkelsen, G. C. Schatz, and T. W. Odom. Real-time tunable lasing from plasmonic nanocavity arrays. 6(1):6939. ISSN 2041-1723. . URL https://www.nature.com/articles/ncomms7939.

[186] A. Yilmaz and M. Utz. Characterisation of oxygen permeation into a microfluidic device for cell culture by in situ NMR spectroscopy. 16(11):2079–2085. ISSN 1473-0189. . URL https://pubs.rsc.org/en/content/articlelanding/2016/lc/c6lc00396f.

[187] H. Yu, J. K. Chen, S. Feng, D. C. Dalgarno, A. W. Brauer, and S. L. Schrelber. Structural basis for the binding of proline-rich peptides to SH3 domains. 76(5): 933–945. ISSN 0092-8674. . URL https://www.sciencedirect.com/science/article/pii/0092867494903670.

[188] S. S. Zalesskiy, E. Danieli, B. Blümich, and V. P. Ananikov. Miniaturization of NMR Systems: Desktop Spectrometers, Microcoil Spectroscopy, and "NMR on

a Chip" for Chemistry, Biochemistry, and Industry. 114(11):5641–5694. ISSN 0009-2665. . URL https://doi.org/10.1021/cr400063g.

[189] Q. Zhang, R. Horst, M. Geralt, X. Ma, W.-X. Hong, M. G. Finn, R. C. Stevens, and K. W. . Microscale NMR Screening of New Detergents for Membrane Protein Structural Biology. 130(23):7357–7363. ISSN 0002-7863. . URL https://doi.org/10.1021/ja077863d.